ABSTRACT

Title of Document: MICELLES OF POLYBUTADIENE-*b*-POLY(ETHYLENE OXIDE) IN A BINARY SOLVENT SYSTEM

Christopher Daniel Ploetz, M.S., 2008

Directed By: Professor Sandra C. Greer
Department of Chemical Engineering

We studied the assembly behavior of a polybutadiene-*b*-poly(ethylene oxide) diblock copolymer in methanol, cyclohexane, and the corresponding partially miscible binary solvent system. Dynamic light scattering indicates that the copolymer forms coexisting spherical and cylindrical micelles in both of the pure solvents. In the binary solvent system, spherical micelles form in the methanol-rich phase for a wide range of temperatures. Conversely, micelles are present in the cyclohexane-rich phase only near the critical temperature. At the critical solvent composition, micelles form in the single phase region above the critical temperature. Size exclusion chromatography results for the binary solvent system show that the copolymer generally prefers the methanol-rich phase. The preference becomes more pronounced as temperature decreases.

MICELLES OF POLYBUTADIENE-*b*-POLY(ETHYLENE OXIDE) IN A BINARY SOLVENT SYSTEM

By

Christopher Daniel Ploetz

Thesis submitted to the Faculty of the Graduate School of the
University of Maryland, College Park, in partial fulfillment
of the requirements for the degree of
Master of Science
2008

Advisory Committee:
Professor Sandra C. Greer, Chair
Professor Mikhail A. Anisimov
Associate Professor Srinivasa R. Raghavan

Dedication

To my wife; thanks for putting up with the long nights of data collection.

Acknowledgements

I would like to thank Professor Sandra C. Greer for inspiring this work and providing the direction, expertise, and encouragement that brought it to completion.

The members of our group, Dr. Alexander I. Norman, Ms. Bryna C. Clover, and Mr. Evan L. Frank, offered great ideas, assistance, and camaraderie.

I am very grateful to Professor Srinivasa R. Raghavan for the generous use of his instruments, to Professor Philip DeShong and Mr. Ju-Hee Park for provision of vital materials, and to Professor Mikhail A. Anisimov and Mr. Kirtland L. Linegar for offering guidance and sharing their expertise.

I am also grateful to the donors of the Petroleum Research Fund, administered by the American Chemical Society.

Table of Contents

List of Tables

List of Figures

Chapter 1: Introduction

Aqueous solutions of polybutadiene-*b*-poly(ethylene oxide) (PB-*b*-PEO), like other amphiphilic block copolymers, have received much attention in the literature.[1-18] Investigations have determined the configuration of the microphase (*e.g.* isolated assemblies, networks, *etc*.) as a function of copolymer concentration[3, 4] as well as molecular mass and copolymer composition[6-8, 11-14, 18] (*i.e.*, relative length of the two blocks). In "dilute" aqueous solutions (~18 wt% or less[8]), PB-*b*-PEO forms aggregates spanning the complete range of configurations from spherical micelles (for relatively short PB blocks), through cylindrical (worm-like) micelles, to bilayers (for relatively long PB blocks).[6-8]

We have not found any studies of PB-*b*-PEO in solvents other than water. Likewise, the behavior of any amphiphilic block copolymer in the presence of a binary solvent (*i.e.*, two partially miscible solvents that form coexisting liquid phases) has received relatively little attention. Chemical intuition, corroborated by limited theoretical[19] and experimental[20, 21] work, indicates that dilute solutions of amphiphilic block copolymers in binary solvents should yield micelles in the polar phase and reverse micelles in the non-polar phase. The only relevant experimental work[20, 21] developed a complete three-component (tri-block copolymer/water/"oil") phase diagram that appears to indicate the presence of spherical micelles in both of the coexisting phases at low copolymer concentration. However, this work focused on the copolymer-rich corner of the phase diagram and the multitude of microstructures formed there. It is not clear how rigorously the copolymer-lean side of the phase

diagram was investigated, nor if the authors meant to imply the presence of micelles in coexisting phases.

Therefore, we have investigated the behavior of a PB-*b*-PEO diblock copolymer of narrow polydispersity (1.04) and roughly equivalent block lengths (54.7 wt% PEO) in the methanol/cyclohexane binary solvent system, which is partially miscible at room temperature and exhibits an ambient pressure upper critical solution temperature between 45 ºC[22, 23] and 48 ºC[24] at 29 wt% methanol (51.7 mol% methanol).[22] This work focuses specifically on the copolymer-lean side of the three-component phase diagram in order to determine if micelles are formed in both of the coexisting liquid phases, and to determine if micelles are present above the critical temperature. PB-*b*-PEO was selected for this study because the solubility properties of the two blocks are very different, which leads us to believe that microphase separation should occur for a wide variety of solvents even for small concentrations of copolymer.

Before investigating the binary solvent system, the micellization behavior of the copolymer in each of the pure solvents was characterized. In methanol, the copolymer appears to form coexisting spherical and cylindrical regular micelles. Changes in temperature and concentration have little effect. In cyclohexane, spherical and cylindrical reverse micelles are observed at elevated temperatures, but only cylindrical micelles exist at lower temperatures. There is no concentration effect. We also attempted to find the critical micelle concentration in cyclohexane, but it is experimentally inaccessible for the method we used.

Results in the binary solvent system indicate that micelles do form in both coexisting liquid phases for a small range of temperatures near the critical temperature. Micelles disappear from the cyclohexane-rich phase as the temperature is lowered, but remain in the methanol-rich phase. Micelles were also found above the critical temperature at the critical solvent concentration.

The disappearance of micelles in the cyclohexane-rich phase can be explained by the fact that the copolymer preferentially partitions into the methanol-rich phase and that the temperature effect for this phenomenon is strong (*i.e*. the ratio of the concentration in the methanol-rich phase to the concentration in the cyclohexane-rich phase increases as the temperature decreases).

Chapter 2: Theory

2.1 Micelle Formation in Selective Solvents

It is well documented that block copolymers assemble to form micelles as well as other micro- and nanostructures in solvents that are poor for one block and good for the other.[25] Like any phase transition, the solvation, *i.e.*, complete dissolution of both blocks of the copolymer, or microphase separation of block copolymers in solution is governed by the Gibbs free energy change of mixing (ΔG_{mix}),[26-28] which is shown in equation (2.1) and must be positive for microphase separation to occur.

$$\Delta G_{mix} = \Delta H_{mix} - T\Delta S_{mix} \quad (2.1)$$

The thermodynamic potential functions are often defined in terms of micellization (*i.e.*, phase separation) rather than mixing, where, *e.g.* $\Delta G_{mix} = - \Delta G_{mic}$. The mixing convention has been used here in order to make a comparison with liquid-liquid phase equilibrium, but the usual convention can be recovered by replacing the "mix" subscript with "mic" and changing the sign.

In aqueous solutions, when one block is moderately hydrophobic and the other is polar or hydrophilic, microphase separation (*e.g.* micellization) is entropically-driven due to ordering (*i.e.*, a reduction in the number of available configurations) of solvent molecules around the hydrophobic block,[25] which results in a negative entropy of mixing (ΔS_{mix}) and is known as the hydrophobic effect. In this case, both

the enthalpy (ΔH_{mix}) and entropy of mixing are negative. For a given copolymer concentration, microphase separation occurs above a certain temperature, known as the critical micelle temperature (CMT), at which point the entropy penalty for mixing overcomes the favorable enthalpy of mixing. As shown in Figure 2.1a, the CMT generally decreases as copolymer concentration increases.

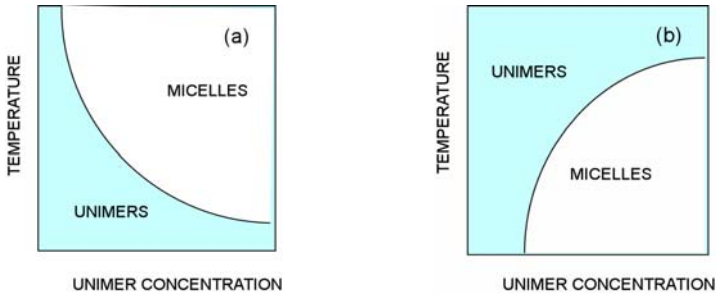

Figure 2.1: Entropically-driven micellization results in micelles above the CMT (a), whereas enthalpically-driven micellization results in micelles below the CMT (b). Figures are courtesy of S. C. Greer.

In non-polar solutions, when one block is at least moderately polar and the other is non-polar, both ΔH_{mix} and ΔS_{mix} are positive,[25] resulting in enthalpically-driven microphase separation below the CMT, which generally increases as copolymer concentration increases as shown in Figure 2.1b. At constant temperature, microphase separation occurs above the critical micelle concentration (CMC) for both cases.

We expect micellization in methanol to be entropically driven and micellization in cyclohexane to be enthalpically driven.

2.2 Liquid-Liquid Phase Equilibrium

Macrophase separation is also governed by equation (2.1), where demixing occurs for positive values of ΔG_{mix}.[29] For systems with a consolute point, liquid-liquid phase equilibrium can be entropically- or enthalpically-driven (in direct analogy to the previous discussion).

Entropically-driven phase separation often occurs when a moderately hydrophobic liquid is mixed with water. In this case, two liquid phases are formed above a lower critical solution temperature (LCST) due to the negative entropy of mixing.

Enthalpically-driven phase separation generally occurs when two liquids, at least moderately different in structure and/or polarity, are mixed. Two liquid phases are formed below an upper critical solution temperature (UCST) due to the positive enthalpy of mixing as the entropic term becomes less important.

The above discussion assumes that ΔH_{mix} and ΔS_{mix} have the same sign, which is not necessary. For systems where $\Delta H_{mix} < 0$ and $\Delta S_{mix} > 0$ across a broad range of temperatures, ΔG_{mix} is negative for any temperature in the range and the single phase is always stable. Conversely, where $\Delta H_{mix} > 0$ and $\Delta S_{mix} < 0$ for a given temperature range, ΔG_{mix} is positive for any temperature in the range and the single phase is always unstable.

As shown in Figure 2.2,[23] the methanol/cyclohexane system exhibits enthalpically-driven demixing below a moderate UCST and is a convenient system for investigating the micellization of PB-*b*-PEO in coexisting phases as well as the behavior of the block copolymer in the single phase region above the UCST.

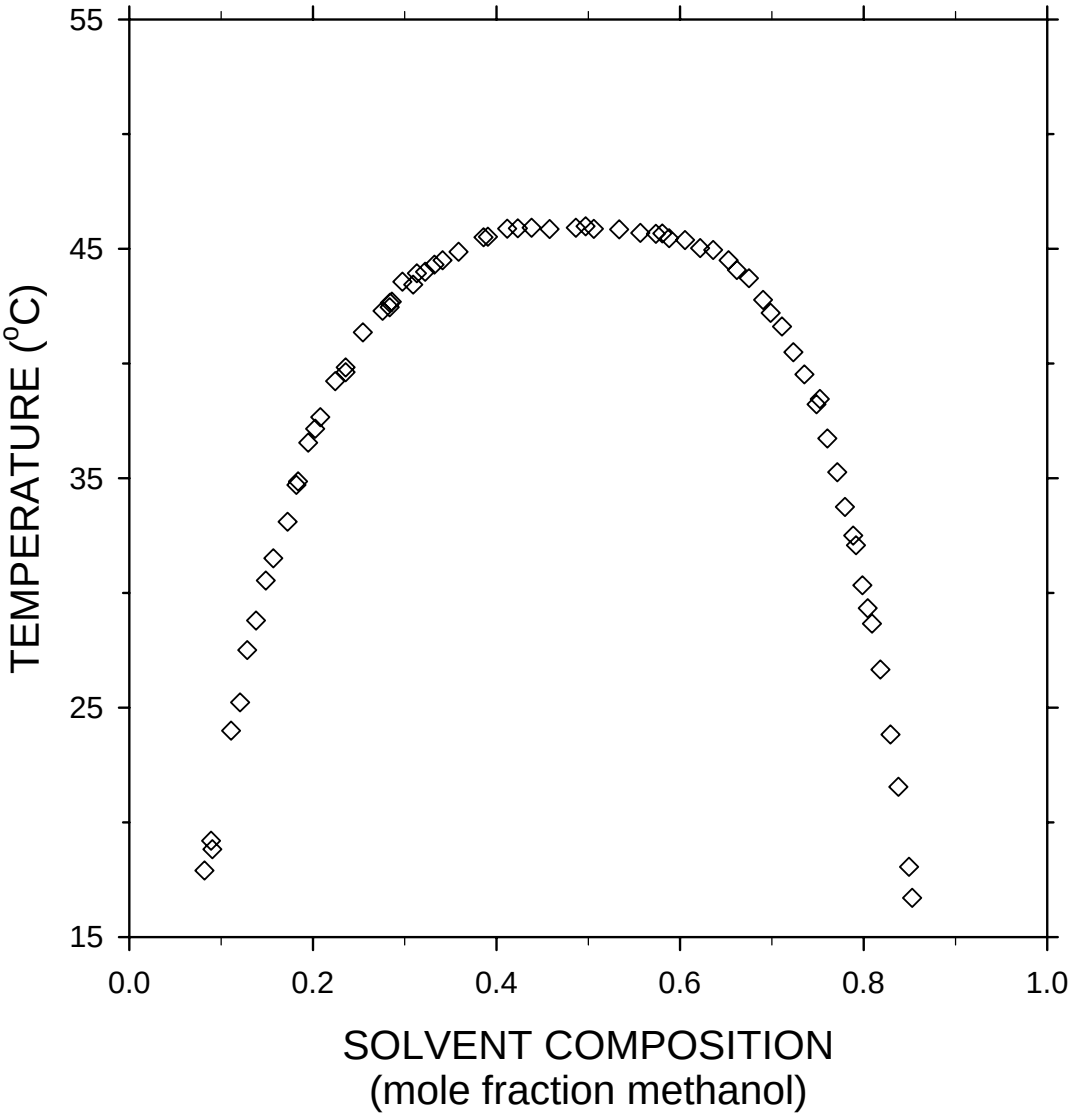

Figure 2.2: Phase diagram of the methanol/cyclohexane system by Matsuda et al. [23]

2.3 Block Copolymer Micelle Formation in Coexisting Liquid Phases

Little is known about the formation of block copolymer micelles in coexisting, partially miscible solvents. However, such a system is not conceptually different from the case of small molecule amphiphiles (*i.e.*, surfactants) in the presence of oil

and water, which form micelles or reverse micelles and then sequester the immiscible phase in the core, *i.e*., interior, of the micelles or reverse micelles. Therefore, we expect micelles to form in the polar phase, reverse micelles to form in the non-polar phase and that the micelle cores may be swollen with the immiscible phase.[19-21, 30]

If the micelles or reverse micelles are swollen by solvation of the immiscible phase, then the resulting micelles or reverse micelles may be larger than those observed in the pure solvents.[30] However, since it is assumed that the solvents are partially miscible, the bulk solvent may be less favorable for the corona block, *i.e*., the exterior block dissolved in the bulk phase, than the pure solvent. If this is the case, the interactions between the bulk phase and the micelle coronas may be smaller than those in the pure solvent, leading to less solvation of the micelle corona and a smaller coronal diameter. The result may be micelles that are ultimately smaller than those observed in the pure solvent.

Chapter 3: Experiments

3.1 Materials

Polybutadiene (1,4-addition)-*b*-poly(ethylene oxide) was obtained from Polymer Source, Inc (catalog number P4603-BdEO). The structure is shown in Figure 3.1. Analyses by the manufacturer (Figures 3.2 and 3.3) indicate that the number average molecular masses of the PB and PEO blocks are 4,800 and 5,800, resulting in approximately 89 and 132 repeating units of butadiene and ethylene oxide, respectively. The mass composition of the copolymer is 54.7 wt% PEO. The polydispersity index is ~1.04 and the PB block is rich in 1,4-microstructure (*i.e.*, each repeating unit is joined at carbons 1 and 4).

$$-\left[CH_2-CH=CH-CH_2\right]_{89}-b-\left[CH_2-CH_2-O\right]_{132}-$$

Figure 3.1: Polybutadiene (1,4-addition)-b-poly(ethylene oxide). The present copolymer consists of ~89 repeating units of butadiene and ~132 repeating units of ethylene oxide.

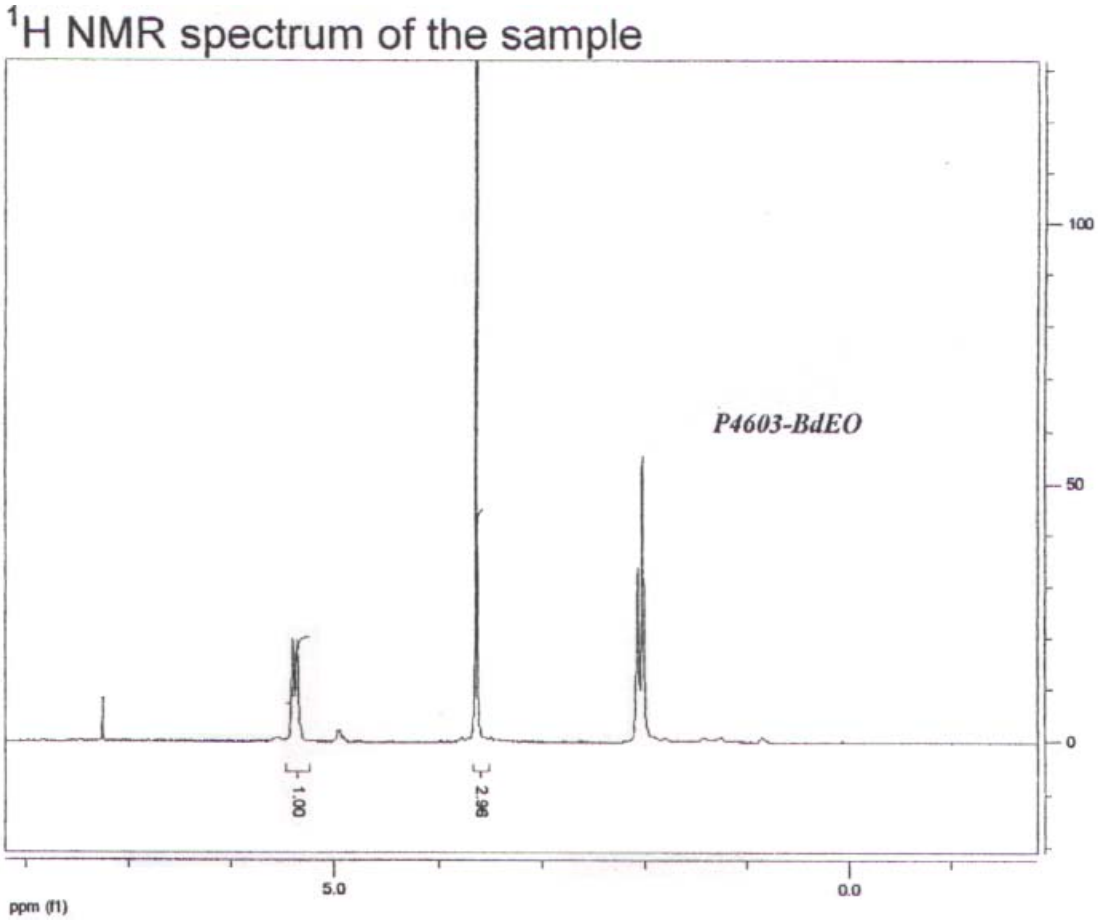

Figure 3.2: ^{1}H NMR (nuclear magnetic resonance) spectrum of the present copolymer (Polymer Source, Inc. catalog number P4603-BdEO) provided by the manufacturer. The peak area of vinylic butadiene protons at ~5.4 ppm relative to the peak area of the ethylene oxide protons at ~3.6 ppm was used to determine the relative block lengths.

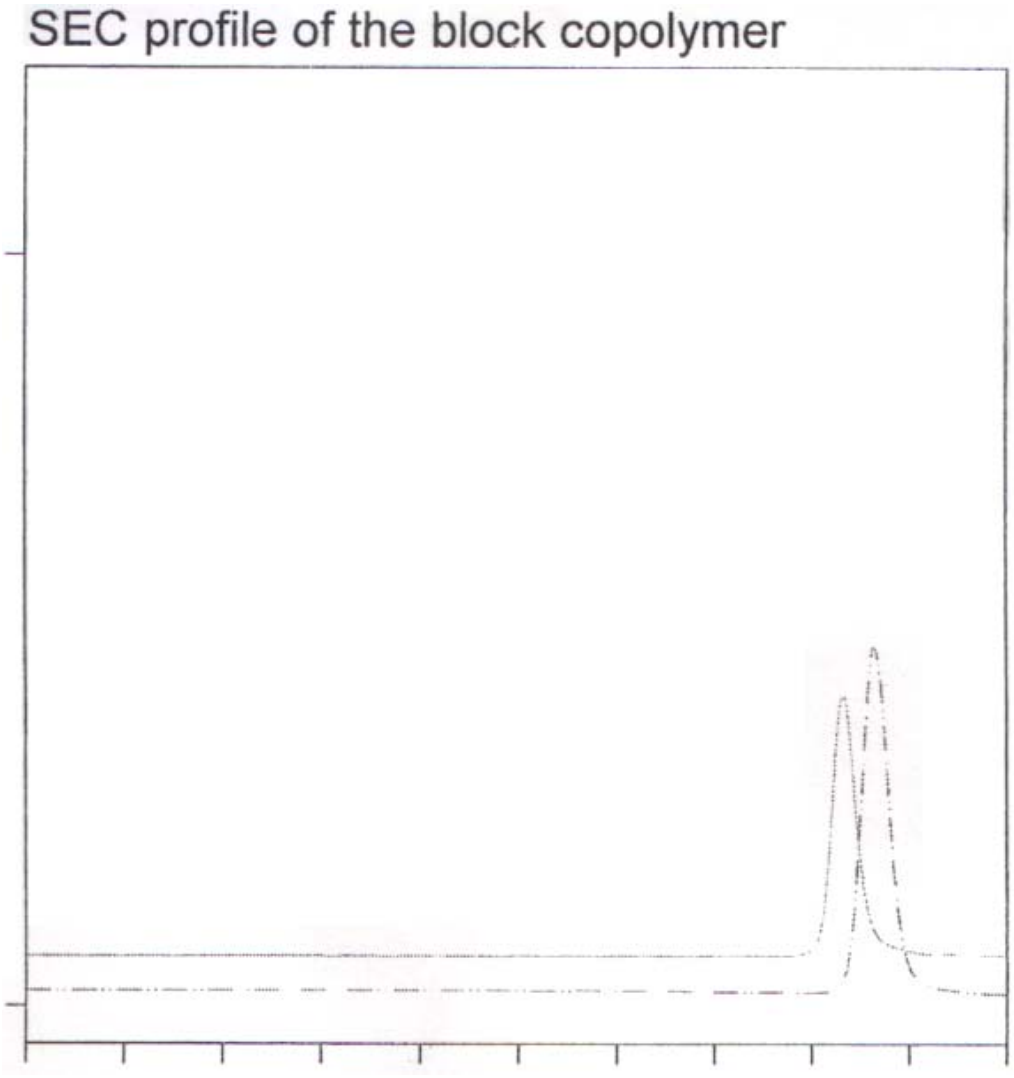

Figure 3.3: The SEC (size exclusion chromatography) results provided by the manufacturer indicate the polybutadiene molecular mass prior to addition of the poly(ethylene oxide) block (dashed line), the copolymer molecular mass (solid line), and the polydispersity index.

Methanol (100.0%) was obtained from J.T. Baker. Methanol to be used for dynamic light scattering and size exclusion chromatography samples was stored over 3 Å molecular sieve beads from Aldrich (8-12 mesh). Cyclohexane (99.9%) was obtained from Fisher. Cyclohexane to be used for dynamic light scattering and size

exclusion chromatography samples was stored over 4 Å molecular sieve beads from Sigma.

The probe molecules, (-) α-pinene (99%, 97% enantiomeric excess) and Rose Bengal, were also obtained from Aldrich.

Silica particles used to determine solvent viscosity by the dynamic light scattering method were provided by Prof. Philip DeShong and Mr. Ju-Hee Park. The particles were prepared according to a method proposed by Nozawa, *et al*.[31] and were reported to be nearly monodisperse with a diameter of approximately 110 nm, as measured by transmission electron microscopy. We measured the size distribution using dynamic light scattering and found the hydrodynamic radius to be 68 nm, with a standard deviation of 18 nm.

3.2 Sample Preparation

Samples for analysis by dynamic light scattering and size exclusion chromatography were prepared from "as-received" PB-*b*-PEO. Solvents were also used "as-received," except that they were stored over molecular sieve beads in order to minimize water contamination, which shifts the UCST of the polymer-free binary solvent system.[22] The UCST of the dehydrated, polymer-free solvent system was checked to ensure that it fell within the range of values reported in the literature (45.5 ^{o}C – 48.5 ^{o}C).[22-24] The measured UCST was <46 ^{o}C, indicating that water contamination of the dehydrated solvents was minimal.

Samples of PB-*b*-PEO in the binary solvent system were prepared by adding the required mass of stock solution (nominally 1 wt% copolymer in cyclohexane) to a

cylindrical glass vial with a Teflon-lined lid. Cyclohexane and methanol were added by mass to achieve the desired concentration of PB-*b*-PEO and the desired polymer-free solvent composition. Samples of PB-*b*-PEO in the pure solvents were prepared either from stock solutions (nominally 0.5 wt% copolymer in methanol or cyclohexane) or by adding the copolymer to a glass vial and adding the required mass of the appropriate solvent to achieve the required copolymer concentration. All masses were measured using a Mettler H80 balance (±0.1 mg). Sample compositions are shown in the relevant tables in Chapter 4 and Appendix C and have been corrected for buoyancy. The number of significant figures indicates the precision to which the concentration is known. A small mass of copolymer was lost during filtration, especially for dynamic light scattering samples, but the magnitude of the loss is believed to be negligible.

After obtaining the required sample composition, each vial was sonicated using a Fisher Scientific FS6 Sonic Cleaner to achieve complete mixing. Samples in the binary solvent were sonicated above the critical temperature in order ensure that the polymer distributed between the two liquid phases according to the thermodynamics of the system.

Due to the sensitivity of dynamic light scattering to dust in the sample, each sample prepared for dynamic light scattering was extensively filtered after sonication. The sample was filtered four times using the same 0.2 μm Teflon filter element (Pall Acrodisc Syringe Filter or Pall TF Membrane Disc Filter). Filtration was executed slowly, with the filtrate directed at the wall of the vial in order to minimize entrainment of air bubbles, which can sometimes remain suspended for long periods

in polar solvents. Care was taken to rinse the inside walls of the vial with the filtrate in an attempt to minimize dust adherence. Finally, a new 0.2 μm Teflon filter element was used as a fifth, polishing filtration step. An exception to this procedure was made for the 0.1 wt% and 0.05 wt% PB-b-PEO samples in pure cyclohexane because newly purchased filters seemed to remove more copolymer than the original filters. Therefore, these samples were not filtered prior to analysis. In all cases, the outer wall of each vial was wiped clean just prior to gathering light scattering data in order to remove dust and finger prints.

Samples for analysis by size exclusion chromatography were filtered once using a 0.2 μm Teflon filter element. After solvent evaporation and rehydration with nanopure water (NANOpure Ultrapure Water System, 0.2 μm final filter, resistivity >18 MΩ-cm), the aqueous SEC samples were filtered once using a 0.2 μm Nylon filter (Pall Nylaflo Membrane Filter).

Samples for capacitance measurement were prepared from "as-received" copolymer and solvent. The most concentrated sample was prepared first by adding polymer and solvent to yield the required concentration. Subsequent samples were prepared by making dilutions of the previous sample in order to conserve polymer. Samples were filtered once with a 0.2 μm Teflon filter element prior to measuring the capacitance.

Samples for polarimetry, dye solvation, and viscometry were prepared from "as-received" solvent, copolymer, and probe (either (-)-α-pinene or Rose Bengal) and were used unfiltered.

3.3 Capacitance Measurement

The CMC or CMT can be found by observing changes in a measurable physical property of the solution as a function of concentration or temperature.[27] If an appropriate property has been selected, a plot of the measured property versus either concentration or temperature will show a marked discontinuity in slope as the value of the CMC or CMT is traversed. Many physical properties can be used for this purpose, but most suffer from a lack of sensitivity when the CMC is very small. Since it has been reported that the CMC of PB-*b*-PEO in water is experimentally inaccessible,[12] we expect that the value of the CMC will be very low in both methanol and cyclohexane, where each pure solvent is highly selective for one of the blocks. Therefore, we attempted to find the CMC and CMT in cyclohexane by measuring the solution capacitance, as proposed by Pérez-Rodríguez,[32] in the hope that it would be more sensitive than light scattering, viscometry and surface tension methods.

Capacitance samples were prepared as described previously and poured into the capacitance cell,[33] which was placed in the reservoir of a Neslab RTE-111 constant temperature bath complete with a VWR 230 submersible stirrer. The sample was stirred in order to quickly achieve thermal equilibrium with the bath at 20 ºC. Samples were allowed at least five minutes to reach thermal equilibrium once the bath temperature had stabilized, after which the stirrer was switched off. The capacitance was recorded after it had reached a steady state value (typically within a few minutes). This process was repeated in increments of 10 ºC over the range [20 ºC, 70 ºC]. Temperature control for this apparatus was ±0.1 ºC. The uncertainty in the measured capacitance is ±0.0001 pF.

In general, it is possible for micelles to be broken up by agitation. For example, loss of opalescence was observed after sonication for some of the pure solvent samples in this study. However, since the capacitance was allowed to reach a steady state after the stirrer was switched off, it is believed that the capacitance values measured in this experiment reflect the capacitance of the solution in the presence of micelles.

3.4 Dynamic Light Scattering

Dynamic light scattering (DLS), is a technique that can be used to measure the hydrodynamic radius of small particles experiencing Brownian motion in a dilute solution.[34, 35] Monochromatic light is directed at the sample of interest and subsequently scattered by the suspended particles. The scattered light is detected by a photo-multiplier tube that is oriented at an angle to the light source. A correlator measures fluctuations in the scattered-light intensity as a function of time and calculates the autocorrelation function of the scattered-light intensity, which is used to determine the translational diffusion coefficients. The distribution of particle sizes can be inferred from the distribution of diffusion coefficients.

The autocorrelation function, $G_2(\tau)$, of the scattered-light intensity is calculated by multiplying the scattered-light intensity, $I(t)$, by the time-delayed scattered-light intensity, $I(t+\tau)$, where τ is the correlation time, and integrating the product over time.[36]

$$G_2(\tau) = < I(t)\, I(t+\tau) > \qquad (3.1)$$

When the particles of interest are monodisperse, the normalized scattered-light intensity autocorrelation function, $g_2(\tau)$, can be fitted to a decaying exponential,[37] as shown in equation (3.2), where the decay rate, Γ, or, equivalently, the inverse of the characteristic decay time, τ_c, is the half-width of the scattered light spectrum and p is the mean square scattered light intensity.

$$g_2(\tau) = 1 + p \cdot \exp(-2\Gamma\tau) \tag{3.2}$$

$$\Gamma = 1/\tau_c \tag{3.3}$$

Polydisperse particles require the following, more sophisticated, analysis.[38] The scattered-light field autocorrelation function, $g_1(\tau)$, can be calculated from the scattered-light intensity autocorrelation function, $g_2(\tau)$, as indicated in equation (3.4). Equation (3.5) is then solved to find the distribution of decay rates, $P(\Gamma)$, from which the distribution of diffusion coefficients can be calculated using equations (3.6) and (3.7).[38]

$$g_2(\tau) = 1 + \left| g_1(\tau) \right|^2 \tag{3.4}$$

$$g_1(\tau) = \int P(\Gamma) \cdot \exp(-\Gamma\tau)\, d\Gamma \tag{3.5}$$

$$\Gamma = Dq^2 \tag{3.6}$$

$$q = \frac{4\pi n}{\lambda}\sin\left(\frac{\theta}{2}\right) \tag{3.7}$$

Here, Γ is the decay rate, D is the translational diffusion coefficient, q is the modulus of the scattering vector, n is the refractive index, λ is the wavelength of incident light, and θ is the scattering angle.

Although solving equation (3.2) to find a single decay rate is straightforward, equation (3.5) is an "ill-posed" problem,[38] meaning that, if the data contain finite uncertainty, multiple solutions can fit the data equally well. Therefore, sophisticated algorithms, such as the CONTIN method[39] or the method implemented in DynaLS,[38] are required to reduce the degrees of freedom and arrive at a meaningful result.

The hydrodynamic radius, R_h, can be calculated from D using equation (3.8), the Stokes-Einstein equation.[37, 40]

$$D = \frac{k_B T}{6\pi\eta R_h} \tag{3.8}$$

Here, k_B is Boltzmann's constant, T is absolute temperature, π is the ratio of a circle's circumference to diameter, and η is the dynamic viscosity of the solvent. The hydrodynamic radius is the radius of a hypothetical hard sphere that translates at the same speed as the real particle. For real spherical particles, including spherical micelles, the hydrodynamic radius is a reasonable approximation of the actual size of the particle. However, it is important to note that real particles, especially spherical

micelles, are not hard and may have a solvation layer that increases the measured radius.[41] Therefore, the hydrodynamic radius must be interpreted as an approximate size.

A PhotoCor DLS instrument was used to gather light scattering data. The instrument consisted of a JDS Uniphase Model 1135P 632.8 nm (red) laser, a photo-multiplier tube, a 288-channel multi-tau correlator, and a precision goniometer with a resolution of ±0.01º. All data were obtained at a scattering angle of 90º. The instrument was operated in self-beating mode and a sample time of $2.5 \cdot 10^{-8}$ s was selected.

Temperature control was provided by circulating water through the annulus of the double-walled sample holder using a Neslab RTE-111 circulating constant temperature bath. The uncertainty in the sample temperature is relatively large due to natural circulation of air through the laser aperture and a temperature offset between the bath and the instrument ($T_{bath} > T_{instrument}$). Over a range of temperatures, the temperature of the sample, as measured by insertion of a thermocouple into a test solution placed in the sample holder, was consistently within 1 ºC (*i.e.*, ±0.5 ºC) of the value indicated by the DLS instrument's thermometer.

DLS samples were prepared as described previously. Copolymer samples in the binary solvent system to be analyzed at elevated temperature were heated above the UCST while inside the instrument's sample holder. The sample was shaken to ensure homogeneity after it had passed into the single-phase region and was then held above the critical temperature for three hours. It was then rapidly cooled to the

temperature of interest and held overnight to allow complete phase separation prior to gathering light scattering data.

Copolymer samples in pure solvents and silica particle samples in both binary and pure solvents that were to be analyzed at elevated temperature were placed in the reservoir of the temperature bath in order to provide rapid heating. After the temperature of the DLS instrument had stabilized at the desired value, a sample was removed from the bath and placed into the instrument's sample holder. Silica particle samples in the binary solvent were shaken prior to being placed in the sample holder in order to ensure that equilibrium phase-separation was achieved, since equilibration time for the mixing of partially miscible phases by diffusion can be very long. Due to the temperature offset between the bath and the instrument, the sample was allowed to equilibrate in the sample holder for at least fifteen minutes or until the scattered light intensity reached a steady state. Measurements indicated that the sample temperature relaxed to the instrument temperature in less than the allotted time.

After the desired temperature had been achieved, light scattering data were collected for a sufficient period of time to yield a clean autocorrelation function and minimize the presence of a "foot." Generally, a collection period of less than five minutes yielded acceptable results, though samples with low copolymer concentration sometimes required longer collection periods.

The autocorrelation functions obtained by DLS were analyzed using DynaLS version 2.8.3 (Alango Ltd).[38] The channels used in the data analysis were selected to exclude anomalous fluctuations at low channel numbers (<55) and scatter or "feet" at high channel numbers. As shown in equations (3.7) and (3.8), the viscosity and

refractive index of the solvent are required to calculate the hydrodynamic radius from the decay rate. These properties are available in the literature for both pure solvents[42-44] and the refractive indices are available for the binary solvent system.[22] Appendix A presents the results of viscosity measurements of the coexisting phases of the binary solvent system.

3.5 Determination of Micelle Configuration using Molecular Probes

For PB-*b*-PEO, chemical intuition indicates that regular micelles (*i.e.*, PB core, PEO corona) should form in methanol, while reverse micelles (*i.e.*, PEO core, PB corona) should form in cyclohexane. In order to test this hypothesis, two molecular probe experiments were conducted.

Rose Bengal, a powdery, magenta-colored, hydrophilic dye that is insoluble in non-polar solvents,[45] was used to determine the micelle conformation in cyclohexane. When Rose Bengal is added to a pure non-polar solvent, it does not dissolve and the solvent remains clear and colorless (though Rose Bengal particles do adhere to the air-solvent meniscus and walls of the vial). When an amphiphilic copolymer is added to the mixture of Rose Bengal and solvent, the solution remains clear and becomes deeply colored, presumably due to sequestration of the dye in the hydrophilic cores of reverse micelles. Therefore, as shown by Basu, *et al.*,[45] Rose Bengal can be used to indicate the presence of reverse micelles in non-polar solution.

Rose Bengal was added to pure cyclohexane and to a 0.2 wt% solution of PB-*b*-PEO in cyclohexane at ambient temperature. Both samples were sonicated and allowed to equilibrate for several days prior to visual inspection to determine if the

addition of PB-b-PEO allowed the Rose Bengal to dissolve in the unfavorable cyclohexane solvent.

Unfortunately, a complementary hydrophobic dye could not be found to test for the existence of regular micelles in methanol. Reichardt's Dye is a solvatochromic, water-insoluble dye that has been used to test for the presence of regular micelles in aqueous solution by the method described above,[45] but we found that it is soluble in methanol and, therefore, unsuitable for use as a molecular probe in methanol.

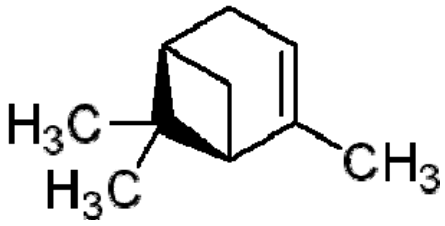

Figure 3.4: (-)-α-pinene is partially miscible in methanol.[46] Figure courtesy of Aldrich.

Rather than using a visible probe, a non-polar chiral probe was used to test for the presence of regular micelles in methanol. (-)-(α)-pinene, a cyclic, C_{10} olefin shown in Figure 3.4, is sparingly soluble in methanol.[46] When added to methanol, the system phase separates into methanol-rich and pinene-rich phases. We hypothesize that addition of PB-*b*-PEO to the binary solvent system will allow additional pinene to be sequestered in the hydrophobic cores of regular micelles, thus increasing the solubility of pinene in the methanol-rich phase. The increased pinene-solubility will result in an increase in the optical rotation of the methanol-rich phase beyond the

baseline rotation. If this hypothesis is correct, then pinene can be used to indicate the presence of regular micelles in a polar solution.

Pure methanol was mixed with pinene and allowed to phase separate. A sample of the methanol-rich phase was removed and its optical rotation was measured using a Jasco P-1010 polarimeter (589 nm, ±0.2% of measured rotation). Since the two solvents are partially miscible, the methanol-rich phase exhibits significant baseline optical rotation. The methanol-rich phase was returned to the original flask and re-mixed with the pinene-rich phase. A small amount of PB-*b*-PEO was added to the solution, which was then allowed to phase separate prior to re-measurement of the optical rotation of the methanol-rich phase. These steps were repeated several times in order to determine if the magnitude of optical rotation increased with the addition of PB-*b*-PEO.

3.6 Measurement of Copolymer Distribution by Size Exclusion Chromatography

Size exclusion chromatography (SEC) is typically used to estimate polymer molecular mass based on the time required for the polymer to flow through a column packed with a porous, permeable gel that has neutral affinity for the polymer sample.[47] Short polymers form coils with relatively small radii while longer polymers yield larger coil radii. Therefore, short polymers are able to diffuse into a greater number of pores as they flow through the column, resulting in elution of the polymer in reverse size order from largest (short elution times) to smallest (long elution times).[47]

SEC analysis results in a plot of signal vs. elution time, where signal strength is related to instantaneous polymer concentration and elution time correlates with molecular mass. The total area under the curve, obtained by numerical integration, is related to the polymer concentration in the original sample.[47] Therefore, the relative concentrations of PB-*b*-PEO in the upper and lower phases of the methanol / cyclohexane system can be obtained using this method.

In order to obtain samples of the copolymer in each of the coexisting liquid phases, binary solvent samples at 0.2 wt% PB-b-PEO were first heated above the critical temperature in the reservoir of a Neslab RTE-111 constant temperature bath. The samples were shaken and allowed to sit above the critical temperature for at least fifteen minutes prior to rapid cooling to the temperature of interest. The samples were allowed to equilibrate for several hours until two clear phases formed.

After equilibration, a 1-mL sample of each phase was removed by inserting a needle through the Teflon-lined rubber lid. The sample was placed in a Precision 31545-10 vacuum oven in order to evaporate the solvent at ambient temperature. The desolvated copolymer was hydrated using nanopure water and filtered once with a 0.2 μm Nylon filter (Pall Nylaflo Membrane Filter).

The samples were analyzed with a Waters SEC instrument operated at 35 ^{o}C using nanopure water as the eluent. The instrument consists of a 717 autosampler, a 1525 binary HPLC pump, three Ultrahydrogel columns (120, 250, 2000) and a 2412 refractive index detector. The relative concentration in each phase was estimated by comparing the areas under the signal strength (differential refractive index) vs. elution time curve for each sample.

Chapter 4: Results

In this chapter, all error bars correspond to a 99% confidence interval.

4.1 Pure Solvents

4.1.1 Molecular Probe Results

Rose Bengal, a polar, hydrophilic dye, was used to determine the conformation of micelles in cyclohexane. Figure 4.1 shows Rose Bengal added to polymer-free cyclohexane (left) and a solution of 0.2 wt% PB-*b*-PEO in cyclohexane (right). Although the polymer-free sample displays slight coloration, it is due to adherence of dye to the vial wall rather than dissolution of the dye.

Figure 4.1: The vial on the left contains undissolved Rose Bengal and copolymer-free cyclohexane. The vial on the right contains Rose Bengal sequestered in the interior of reverse micelles in cyclohexane.

It is clear from Figure 4.1 that Rose Bengal is soluble only in the presence of the block copolymer. We interpret this to mean that molecules of Rose Bengal have been sequestered in the polar, PEO core of reverse micelles, indicating that PB-*b*-PEO forms reverse micelles in pure cyclohexane.

(-)-α-pinene, a chiral, non-polar hydrocarbon that is partially miscible in methanol[46] was used to determine the conformation of micelles in methanol since a suitable dye could not be found. Figure 4.2 shows the optical rotation of the methanol-rich phase of coexisting methanol and pinene as the PB-*b*-PEO concentration increases. The optical rotation of similar copolymer concentrations in pure methanol was checked to ensure that the copolymer itself was not responsible for the increased optical rotation. These samples exhibited negligible optical rotation and did not show any trend with copolymer concentration.

It can be seen that addition of PB-*b*-PEO results in a linear increase (*i.e.*, larger negative magnitude) in the observed optical rotation (not the specific optical rotation), indicating that addition of the block copolymer allows additional pinene to be dissolved in the methanol-rich phase beyond the polymer-free solubility limit. We interpret this to mean that pinene is being sequestered in the PB core of regular micelles, indicating that PB-*b*-PEO forms regular micelles in pure methanol.

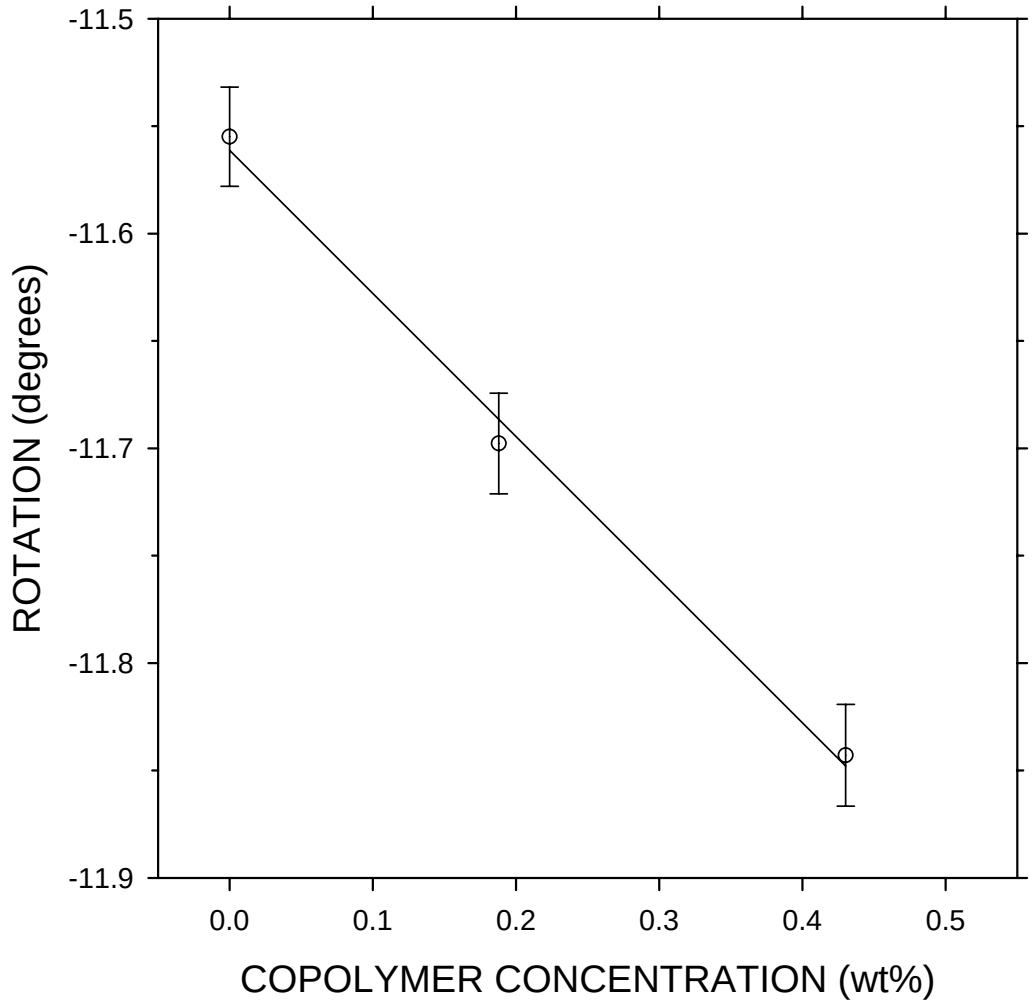

Figure 4.2: The optical rotation of the methanol-rich phase of the partially miscible methanol + (-)-α-pinene system increases linearly with copolymer concentration due to sequestration of (-)-α-pinene in the interior of regular micelles. Note that observed rotation, rather than specific rotation, is plotted on the ordinate. The (x,y) values of the three data points are as follows: (0 wt%,-11.555^{o}), (0.19 wt%,-11.698^{o}), (0.43 wt%,-11.843^{o}).

4.1.2 Dynamic Light Scattering Results

PB-*b*-PEO showed markedly different behaviors in the two pure solvents. DLS data were collected from samples in each solvent over the temperature range (25 ^{o}C – 50 ^{o}C) at the following nominal copolymer concentrations: 0.2 wt%, 0.1 wt%, and 0.05 wt%. Although it might be more instructive to analyze equivalent copolymer mole fraction concentrations (as opposed to mass fraction concentrations) in each solvent, the largest concentration was selected to match the copolymer concentration in the binary solvent system. Also it was convenient to analyze two- and four-fold dilutions in order to approximate the behavior of the copolymer in the phase of the binary system in which the copolymer is less concentrated (as shown in Section 4.2.1, the copolymer does not distribute equally between the two phases of the binary solvent system).

The uncertainty analysis used to determine the error bars for DLS in both the pure solvents and the binary solvent system is presented in Appendix B. The evaluated autocorrelations functions are presented in Appendix C.

4.1.2.1 Methanol

In pure methanol, three distinct hydrodynamic radii are observed at all temperatures, as shown in Figure 4.3 and Table 4.1. The smallest set of radii (< 1 nm) is believed to correspond to unimers. Interpretation of the two larger sets of hydrodynamic radii may be aided by the results of a cryogenic-transmission electron microscopy (cryo-TEM) study[7] of the assembly behavior of several PB-*b*-PEO copolymers in water at room temperature. The study showed that changing the

relative block lengths resulted in a transition from bilayers (B) through cylinders (C) to spheres (S) as the relative length of the PEO block increased. The resulting phase diagram[7] is shown in Figure 4.4.

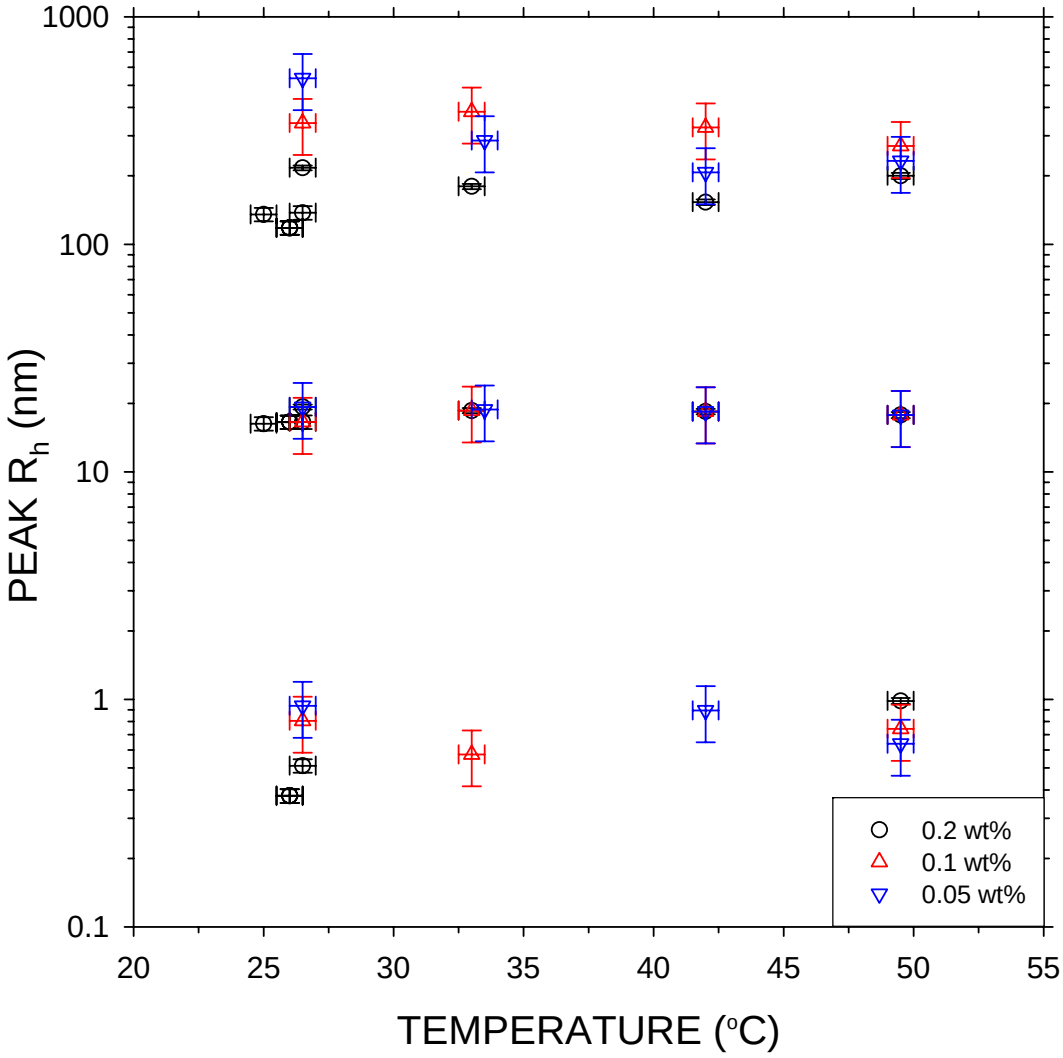

Figure 4.3: Assemblies of PB-b-PEO in methanol show little variation in hydrodynamic radius with temperature and concentration.

				Unimer			Micelle 1			Micelle 2		
Sample	Run Name	Copolymer Concentration	T	peak	mean	uncertainty	peak	mean	uncertainty	peak	mean	uncertainty
-	-	wt%	C	nm	nm	nm	nm	nm	nm	nm	nm	nm
M1	M125 (2)	0.2	25	-	-	-	16.3	16.9	1.1	135.4	134.5	9.2
M1	M126	0.2	26	0.38	0.35	0.03	16.6	17.0	1.1	118.2	121.1	8.1
M1	M126 b4 son	0.2	26	0.38	0.37	0.03	16.6	16.9	1.1	118.2	111.7	8.1
M1	M126.5	0.2	26.5	-	-	-	19.3	19.7	0.5	216.8	219.0	5.3
M1	M1_262	0.2	26.5	0.51	0.47	0.03	16.6	18.1	1.1	137.7	135.4	9.4
M1	m1_334	0.2	33	-	-	-	18.6	17.1	0.5	179.7	181.4	4.7
M1	M1_42	0.2	42	-	-	-	18.4	17.1	0.5	153.2	155.5	4.3
M1	m1_49	0.2	49.5	0.99	1.00	0.03	17.8	18.3	0.5	200.0	260.1	6.0
M4	M4_26	0.10	26.5	0.81	0.74	0.22	16.6	17.4	4.6	341.4	357.0	94.2
M4	m4_333	0.10	33	0.57	0.58	0.16	18.6	19.7	5.1	382.8	479.3	105.6
M4	m4_422	0.10	42	-	-	-	18.4	18.7	5.1	326.3	354.9	90.1
M4	m4_49	0.10	49.5	0.74	0.71	0.21	17.8	17.7	4.9	270.6	347.1	74.8
M5	m5_261	0.050	26.5	0.94	0.87	0.26	19.3	18.3	5.3	537.4	543.4	148.2
M5	m5_333	0.050	33.5	-	-	-	18.8	20.1	5.2	286.2	338.4	79.0
M5	m5_423	0.050	42	0.90	0.84	0.25	18.4	20.1	5.1	207.3	250.6	57.2
M5	m5_491	0.050	49.5	0.64	0.61	0.18	17.8	18.3	4.9	232.6	260.2	64.3

Table 4.1: Hydrodynamic radii of PB-b-PEO assemblies in pure methanol from DLS.

If Figure 4.4 is qualitatively interpreted as a general phase diagram describing the assembly behavior of PB-*b*-PEO in the presence of a solvent that is selective for the coronal block, the ordinate can be labeled "N_{core}" (number of repeating units in the core block) and the absissca can be labeled "w_{corona}" (mass fraction of the corona block relative to the entire copolymer). According to this approximation, the present copolymer would be expected to form coexisting spherical and cylindrical regular micelles in methanol (red triangle). Likewise, cylindrical reverse micelles would be expected to form in cyclohexane (blue triangle).

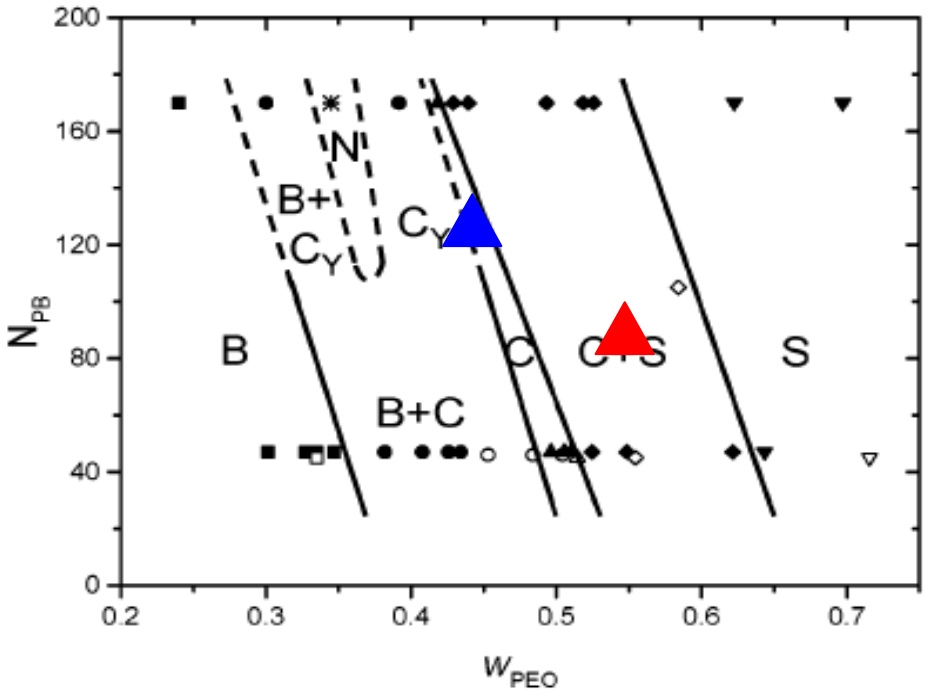

Figure 4.4: Phase diagram of PB-b-PEO in water at 25 °C as a function of copolymer composition.[7] If the phase diagram is generalized to any solvent that is selective for one block, the current copolymer block composition is represented by the red triangle (methanol solvent) and the blue triangle (cyclohexane solvent). N_{PB} is the number of repeating PB blocks and w_{PEO} is the mass fraction of the PEO block. B, C, and S, stand for bilayers, cylinders, and spheres and refer to the type of assembly formed in the corresponding region of the phase diagram.

This approach implicitely assumes that the phase diagram can be extrapolated to other solvents based on packing arguments[48] without accounting for the potentially large difference in corona-solvent interactions that may occur in a different solvent system. Also, it is important to note that the copolymer used in the cryo-TEM study was rich in 1,2-microstructure (*i.e.*, as shown in Figure 4.5, the PB block was branched not linear),[7] whereas the current copolymer is rich in 1,4-microstructure, as shown in Figure 3.1. In spite of these caveats, the cryo-TEM study helps explain our results.

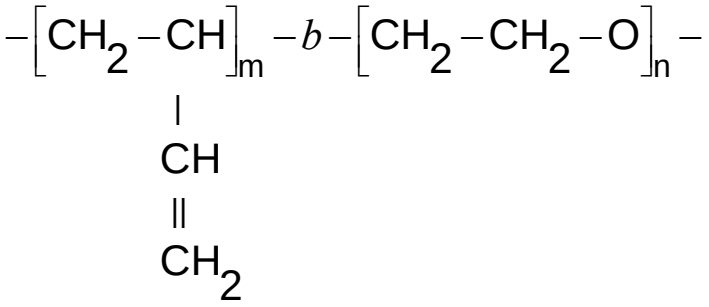

Figure 4.5: Polybutadiene (1,2-addition)-b-poly(ethylene oxide).

Based on Figure 4.4, it is reasonable to conclude that the intermediate and large radii shown in Figure 4.3 represent spherical and cylindrical micelles, respectively.

For the relatively small range of temperatures and concentrations studied, there is no effect of either temperature or concentration on the hydrodynamic radii of the spherical micelles. There is some variation in the hydrodynamic radii of the cylindrical micelles with concentration, though there is no discernable trend; for the majority of the temperatures, the intermediate concentration exhibits the largest radii.

Scatter in the hydrodynamic radii of the cylindrical micelles decreases with temperature, but there is no obvious temperature effect. Since it is typical for cylindrical micelles to exhibit a large distribution of contour lengths[49] and since the hydrodynamic radius of cylindrical micelles is expected to be much more dependent on the contour length than the cylindrical radius, the scatter in the cylindrical micelles' hydrodynamic radii is reasonable.

The mean scattered intensity for each concentration showed no trend with temperature, though (as expected) it decreased with concentration.

In addition to the radii plotted in Figure 4.3, the majority of the samples also present one or more hydrodyamic radius in the micron to millimeter range. Generally, the fractional area of the peak(s) (when plotted on an intensity versus hydrodynamic radius graph) was small (<10%). These are believed to be dust peaks rather than legitimate micelle peaks.

4.1.2.2 Cyclohexane

At low temperatures in cyclohexane, only one hydrodynamic radius was detected by DLS, as shown in Figure 4.6 and Table 4.2. At higher temperatures, two radii were discernable and, at 42 ^{o}C, unimers were detected in one of the samples.

The order-of-magnitude difference in the hydrodynamic radii at elevated temperature indicates that two distinct structures are in coexistence, whereas only one structure is present at low temperature. Therefore, upon heating, a transition takes place in the nature of the assemblies. If the low temperature (25 ^{o}C – 35 ^{o}C) and elevated temperature (40 ^{o}C – 50 ^{o}C) data are evaluated separately, there is perhaps a

slight decrease in the hydrodynamic radius with temperature, but the effect is very small.

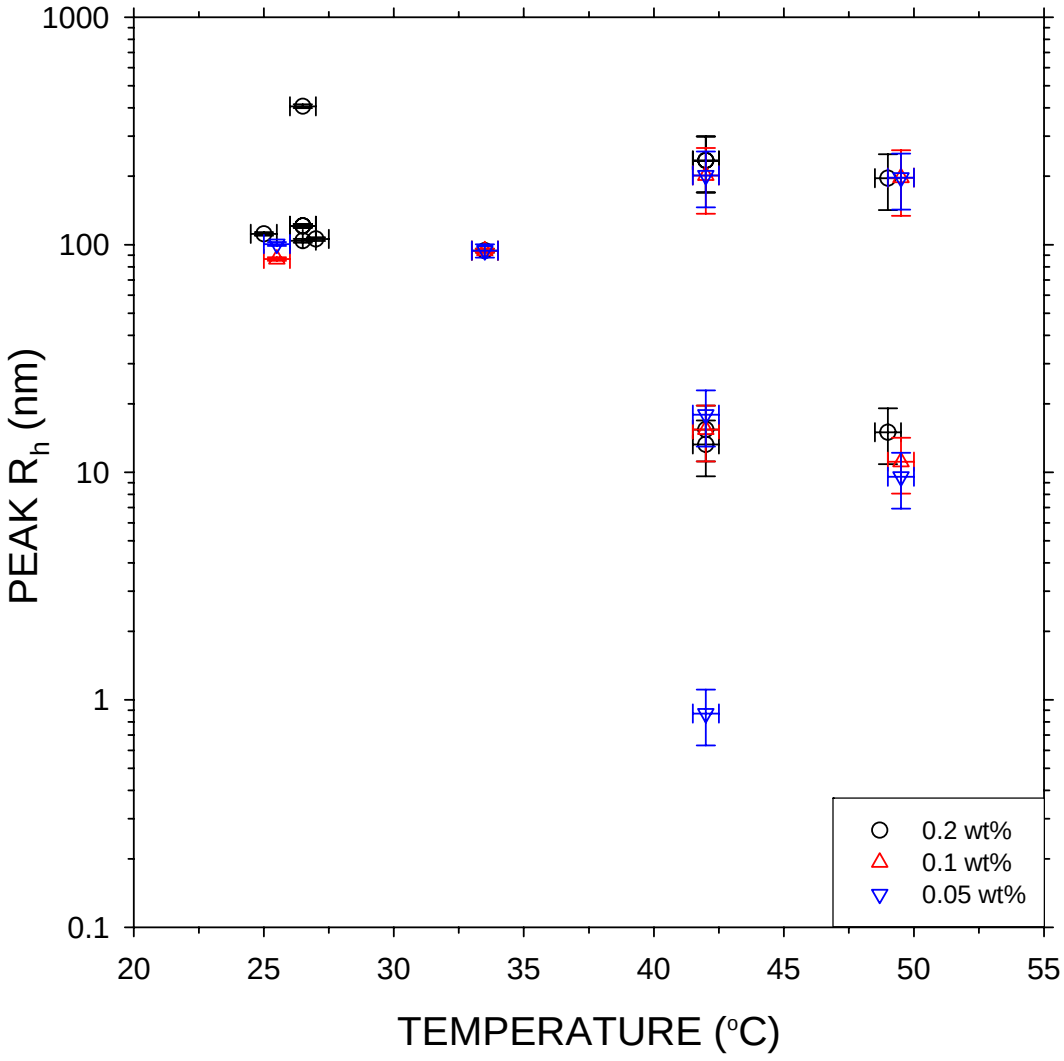

Figure 4.6: Assemblies of PB-b-PEO in cyclohexane show a transition between cylindrical micelles at low temperature and coexisting cylindrical and spherical micelles at elevated temperature.

As stated previously, extrapolation of Figure 4.4 indicates that the present copolymer would form cylindrical reverse micelles in cyclohexane. However, its location on the phase diagram is very close to the transition between cylindrical

micelles and coexisting cylindrical and spherical micelles, so it is not unreasonable to conclude that the system undergoes a transition from cylindrical micelles at low temperature to coexisting cylindrical and spherical micelles at elevated temperature.

Like the results in methanol, there is negligible variation and no discernable trend in hydrodynamic radii with concentration.

It is unclear why unimers could be detected in most of the methanol samples but only one cyclohexane sample. This could indicate that the ratio of unimers to assemblies in higher in methanol than cyclohexane.

As shown in Figure 4.7 and Table 4.3, the mean scattered intensity decreases at elevated temperature, paralleling the transition from cylindrical micelles to coexisting cylindrical and spherical micelles. If the low temperature and elevated temperature intensities are evaluated separately, there appears to be a slight decrease with temperature, which parallels the hydrodynamic radii results. We interpret the decrease in scattered intensity to be a direct consequence of the shift toward spherical micelles.

Similar to the results in methanol, several samples present a hydrodyamic radius in the micron to millimeter range. These are believed to correspond to dust contamination rather than micelles. This conclusion is supported by the fact that the dust peaks are present only in the elevated temperature samples where the scattered intensity is low and dust becomes more problematic.

				Unimer			Micelle 1			Micelle 2		
Sample	Run Name	Copolymer Concentration	T	peak	mean	uncertainty	peak	mean	uncertainty	peak	mean	uncertainty
-	-	wt%	C	nm	nm	nm	nm	nm	nm	nm	nm	nm
cC1	cC125 4	0.2	25	-	-	-	-	-	-	111.6	116.9	2.1
cC1	cC1_26.5	0.2	26.5	-	-	-	-	-	-	121.1	120.8	2.3
cC1	cC126	0.2	26.5	-	-	-	-	-	-	121.1	130.7	2.3
cC1	cC126 b4 son	0.2	26.5	-	-	-	-	-	-	104.1	116.0	2.0
cC1	cc1_27	0.2	27	-	-	-	-	-	-	105.9	104.3	2.0
cC1	cC1_33	0.2	33.5	-	-	-	-	-	-	94.2	95.2	1.9
cC1	cc1_42	0.2	42	-	-	-	15.4	17.2	4.2	234.5	264.9	64.6
cC1	cc1_421	0.2	42	-	-	-	13.3	18.1	3.7	234.5	246.9	64.6
cC1	cc1_491	0.20	49	-	-	-	15.0	17.2	4.1	196.1	235.4	54.1
cC12	cc12_254	0.10	25.5	-	-	-	-	-	-	86.6	89.2	1.6
cC12	cc12_33	0.10	33.5	-	-	-	-	-	-	94.2	92.2	1.9
cC12	cc12_423	0.10	42	-	-	-	15.4	18.7	4.2	234.5	275.2	64.6
cC12	cc12_49	0.100	49.5	-	-	-	11.1	11.4	3.1	229.1	468.7	63.2
cC11	cc11_254	0.050	25.5	-	-	-	-	-	-	100.7	99.5	1.9
cC11	cc11_331	0.050	33.5	-	-	-	-	-	-	94.2	88.9	6.3
cC11	cc11_421	0.050	42	0.87	0.75	0.24	17.9	19.2	4.9	201.6	216.9	55.6
cC11	cc11_49	0.050	49.5	-	-	-	9.6	10.1	2.6	197.0	229.0	54.3

Table 4.2: Hydrodynamic radii of PB-b-PEO assemblies in pure cyclohexane from DLS.

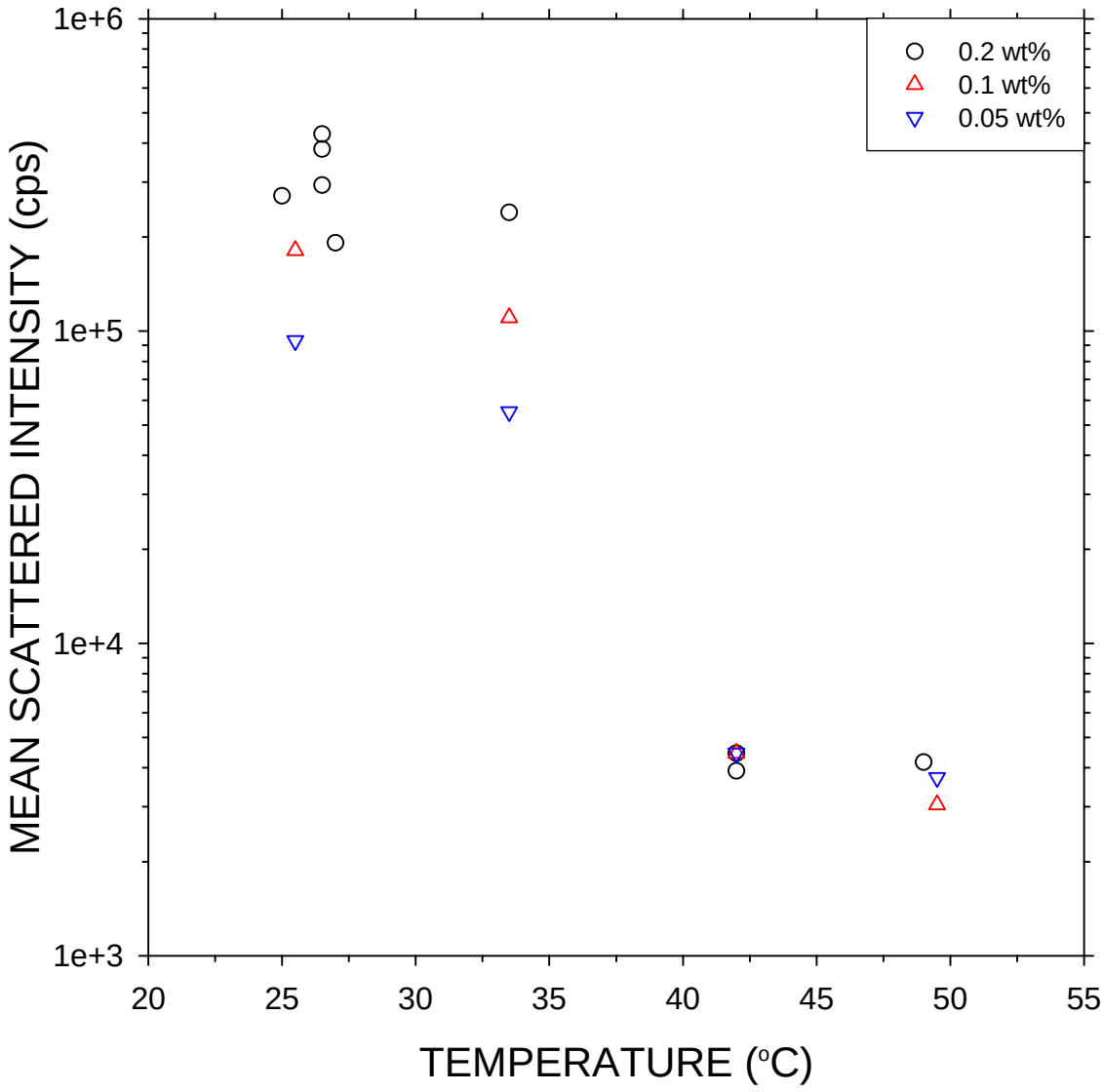

Figure 4.7: Scattered intensity decreases at elevated temperature, which is consistent with the hydrodynamic radii results. The units of the ordinate are counts per second (cps).

Sample	Run Name	Copolymer Concentration	T	Intensity
-	-	wt%	C	cps
cC1	cC125 4	0.20	25	270,847
cC1	cC1_26.5	0.20	26.5	293,272
cC1	cC126	0.20	26.5	382,750
cC1	cC126 b4 son	0.20	26.5	427,265
cC1	cc1_27	0.20	27	191,692
cC1	cC1_33	0.20	33.5	239,760
cC1	cc1_42	0.20	42	3,905
cC1	cc1_421	0.20	42	4,450
cC1	cc1_491	0.20	49	4,165
cC12	cc12_254	0.10	25.5	181,114
cC12	cc12_33	0.10	33.5	110,438
cC12	cc12_423	0.10	42	4,450
cC12	cc12_49	0.10	49.5	3,047
cC11	cc11_254	0.050	25.5	93,067
cC11	cc11_331	0.050	33.5	55,136
cC11	cc11_421	0.050	42	4,450
cC11	cc11_49	0.050	49.5	3,719

Table 4.3: Mean scattered intensity of PB-b-PEO samples in pure cyclohexane measured by DLS.

4.1.3 Capacitance Measurement

The capacitance of PB-*b*-PEO in cyclohexane was measured as a function of temperature for two copolymer concentrations in an attempt to find a concentration low enough to allow the CMT to be traversed. Since micelles were detected by DLS at 0.05 wt%, this was selected as the high concentration. The low concentration was arbitrarily selected to be three orders of magnitude lower, *viz*. $5 \cdot 10^{-5}$ wt%. Figure 4.8 and Table 4.4 present the results and compare them to the capacitance of the polymer-free solvent.

There is no meaningful difference between the three sets of data. Therefore, it is apparent that the capacitance method for finding the CMT suffers from the same lack of sensitivity experienced by other methods (viscosity, surface tension, light scattering, *etc*.) when the CMC is very small. We must conclude that the CMC of the present copolymer in cyclohexane is not experimentally accessible. We decided not to search for the CMT in methanol.

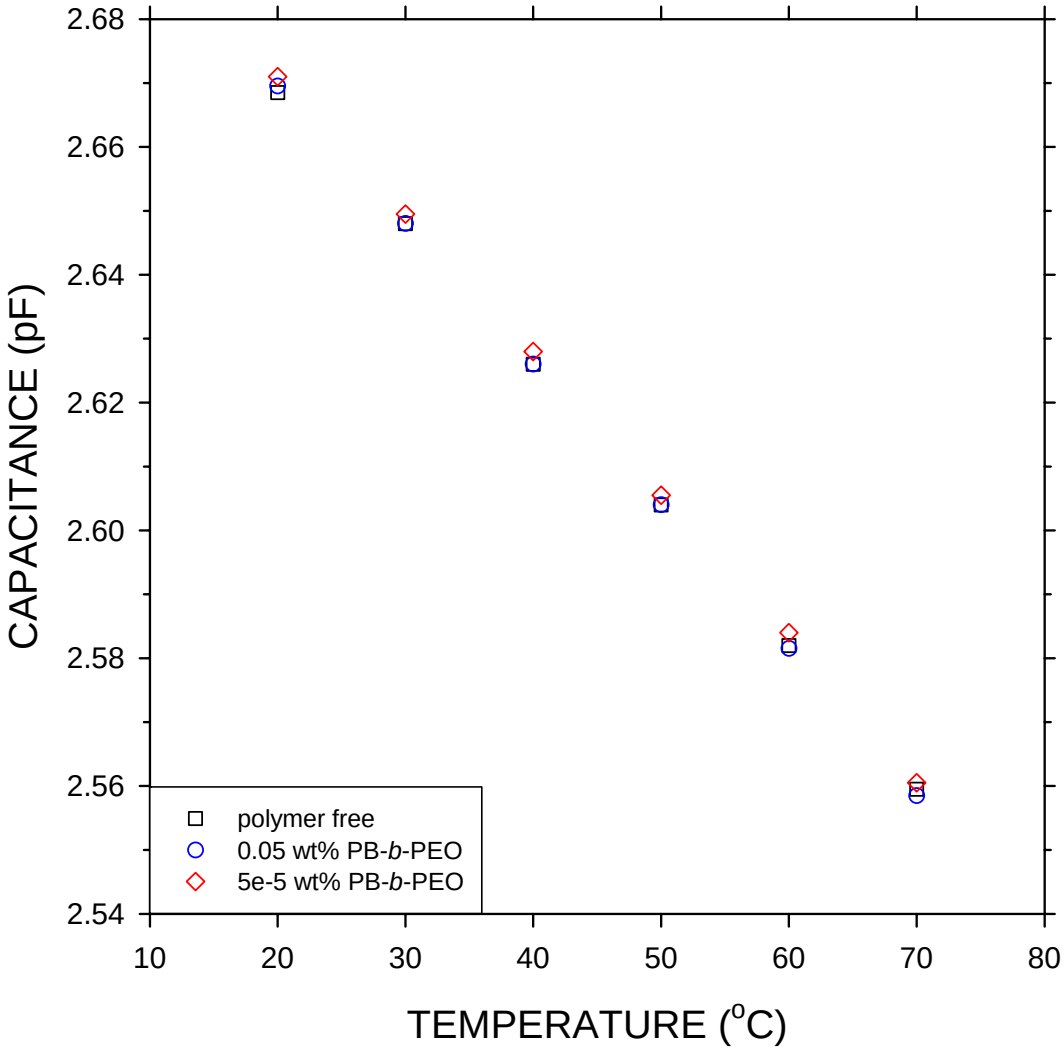

Figure 4.8: Capacitance measurements for PB-b-PEO in cyclohexane did not detect the CMT. Error bars are smaller than the data points.

Capacitance (pF)			
T C	polymer free	0.05 wt%	5e-5 wt%
20	2.6685	2.6695	2.6710
30	2.6480	2.6480	2.6495
40	2.6260	2.6260	2.6280
50	2.6040	2.6040	2.6055
60	2.5820	2.5815	2.5840
70	2.5595	2.5585	2.5605

Table 4.4: Capacitance of solutions of PB-b-PEO in cyclohexane as a function of temperature and copolymer concentration.

4.2 Binary Solvent

4.2.1 Size Exclusion Chromatography Results

The distribution of the copolymer between the upper and lower phases of the binary solvent was analyzed by using SEC to estimate the relative concentration of the copolymer in the two phases. Figure 4.9 and Table 4.5 show the mass per volume concentration ratio between the lower, methanol-rich and upper, cyclohexane-rich phases for a nominal bulk copolymer concentration of 0.2 wt% at the critical solvent composition.

For the narrow temperature range investigated, it can be seen that copolymer concentration in the lower phase increases with decreasing temperature. Since the methanol composition in the upper phase also decreases with decreasing temperature, it is apparent that the concentration of PB-*b*-PEO in each of the coexisting phases is directly related to the methanol composition of the phase (*i.e.*, PB-*b*-PEO prefers a methanol-rich solvent environment to a cyclohexane-rich solvent environment).

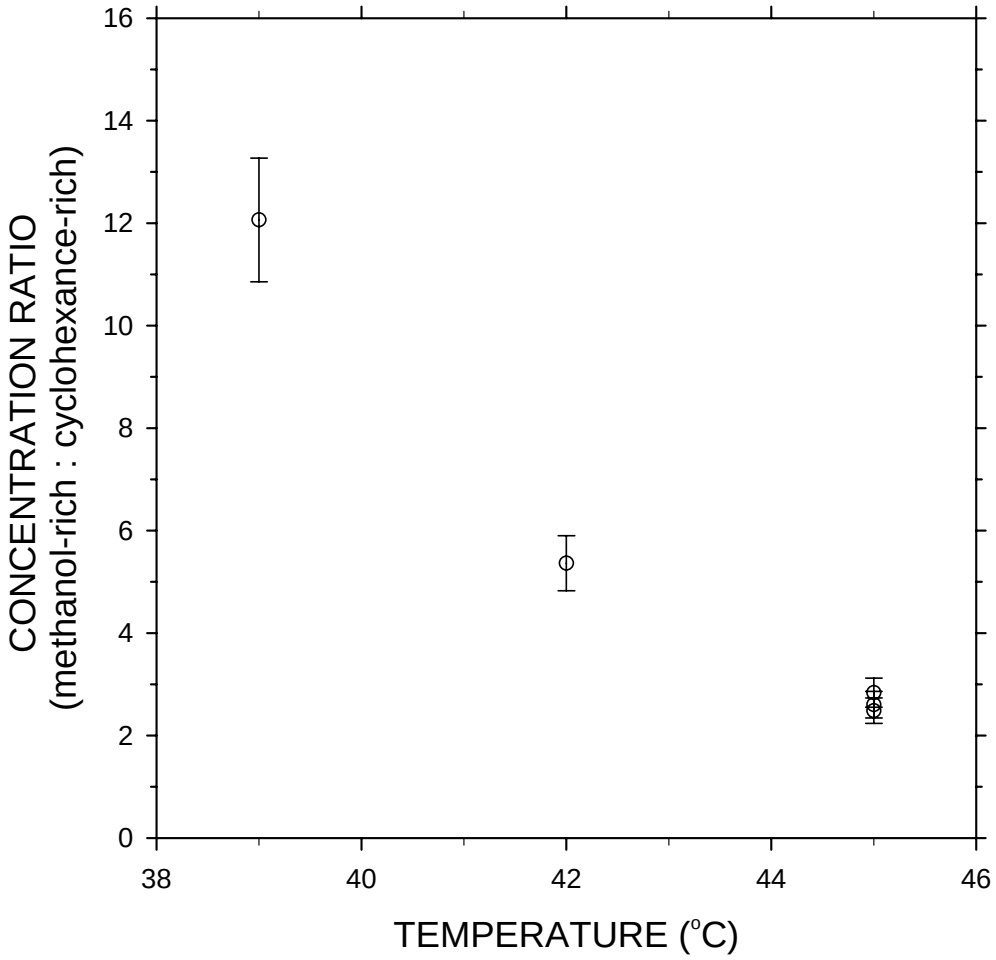

Figure 4.9: The mass per volume concentration ratio increases with decreasing temperature, indicating that the copolymer prefers a methanol-rich solvent environment. The bulk copolymer concentration is nominally 0.2 wt%.

Figure 4.10 and Table 4.5 show the concentration ratio at 39 °C for a nominal bulk copolymer concentration of 0.2 wt% as a function of bulk solvent composition in the two-phase region at 39 °C. Since the compositions of the upper and lower phases are functions of temperature only, changing the bulk solvent composition changes the relative volume of the two phases, as shown in Figure 4.11. As the bulk methanol composition increases, the relative volume of the two phases increasingly favors the lower phase, methanol-rich phase. Therefore, the upper, cyclohexane-rich phase has

greater volume when the bulk solvent is cyclohexane-rich and the lower, methanol-rich phase has greater volume when the bulk solvent is methanol-rich. At the critical composition (~51.5 mol% methanol)[22] and near the UCST, the volumes of the coexisting phases were observed to be approximately equal.

If one assumes that the copolymer mass distribution ratio (*i.e.*, mass in the methanol-rich phase : mass in the cyclohexane-rich phase) is approximately constant, the results can be understood by noting that the concentration ratio decreases as the volume of the methanol-rich phase increases, *i.e.*, for a given mass of copolymer in the methanol-rich phase, the concentration decreases as the volume increases. While this is perhaps a gross approximation, it does explain the high copolymer concentrations observed in methanol-rich phase on the cyclohexane-rich side of the phase diagram.

The trend with bulk solvent composition shown in Figure 4.10 does not appear to be linear. However, the volume of the methanol-rich phase at 33 mol% methanol is very small, which makes it difficult to obtain a good sample of the methanol-rich phase (*i.e.*, the sample may be contaminated by the cyclohexane-rich phase, which has a lower copolymer concentration). It is believed that the concentration ratio at 33 mol% methanol is higher than indicated by Figure 4.10, which would result in more linear behavior in the concentration ratio as a function of bulk solvent composition.

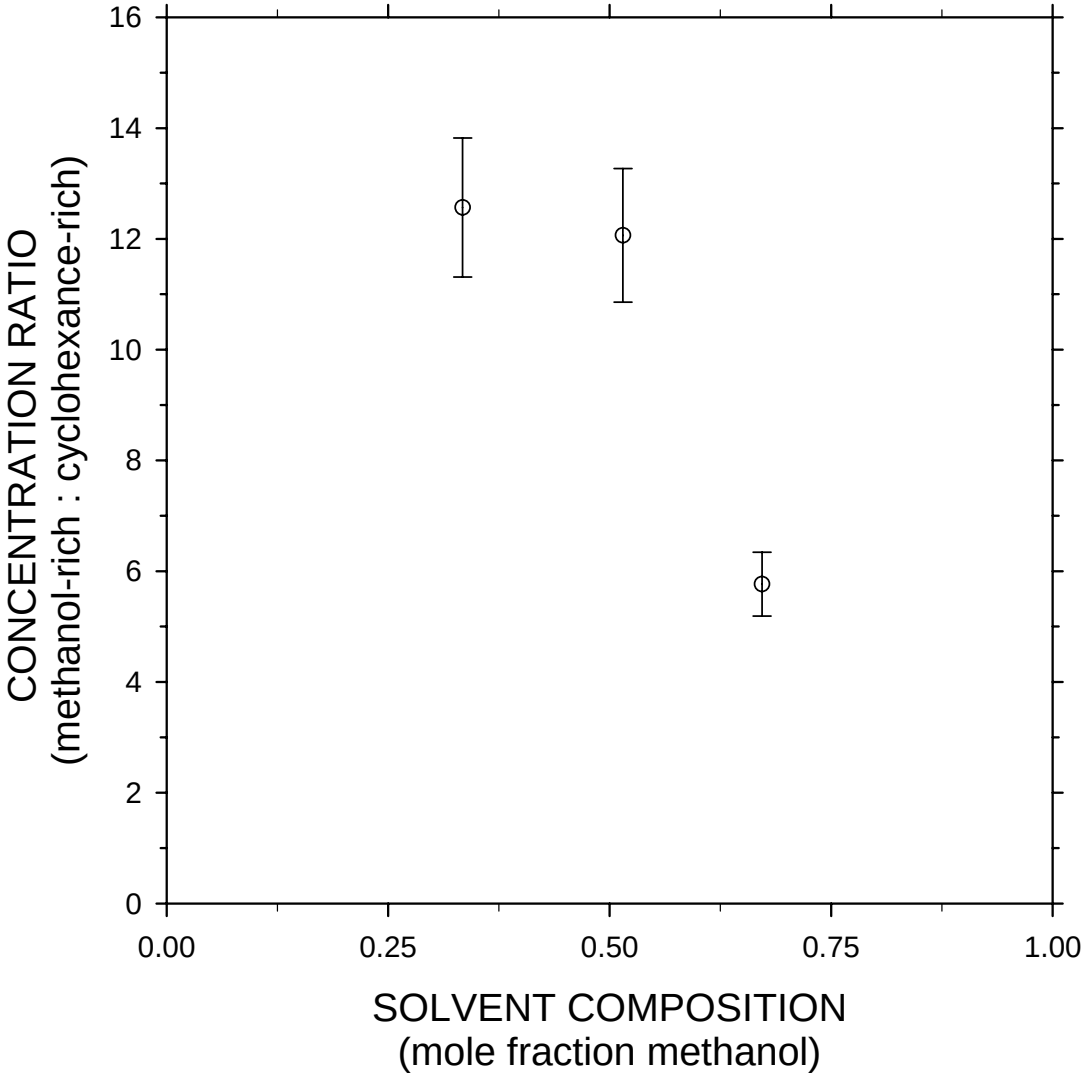

Figure 4.10: At 39 ^{o}C, the mass per volume concentration ratio decreases with increasing bulk methanol composition. This can be understood by presuming that the majority of the copolymer partitions into the methanol-rich phase regardless of the bulk solvent composition. Therefore, the copolymer concentration in the methanol-rich phase decreases as volume of the methanol-rich phase increases. The bulk copolymer concentration is nominally 0.2 wt%.

Concentration Ratio			
T C	33.4 mol% methanol	51.5 mol% methanol	67.2 mol% methanol
39	12.57:1	12.06:1	5.76:1
42	-	5.36:1	-
45	-	2.84:1	-
45	-	2.60:1	-
45	-	2.49:1	-

Table 4.5: Mass per volume copolymer concentration ratios (methanol-rich phase : cyclohexane-rich phase)measured by SEC as a function of temperature and bulk solvent composition.

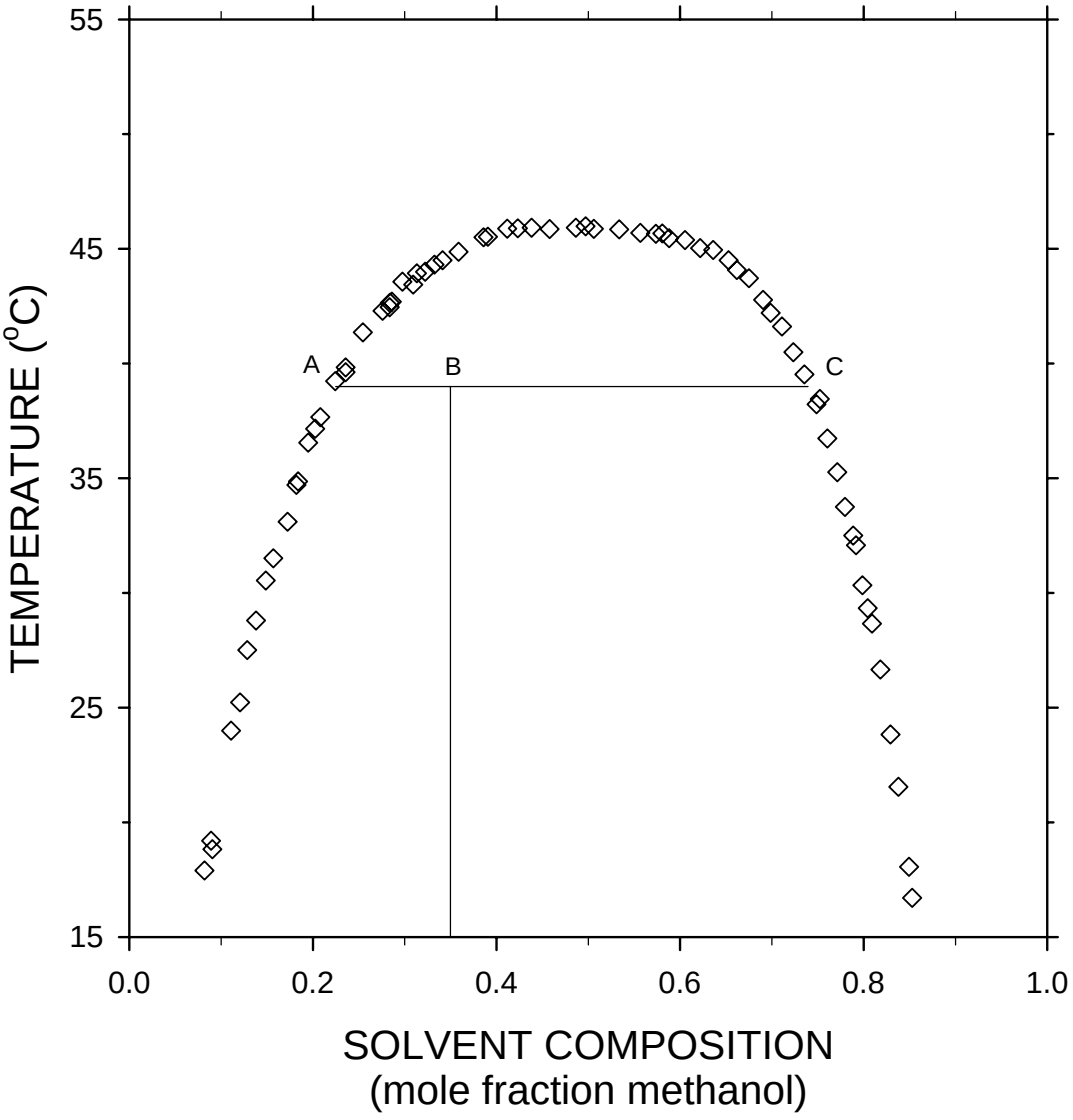

Figure 4.11: The relative amount of each coexisting phase is governed by the lever-rule[50] (i.e., the material balance). For example, a bulk composition of 35 mol% methanol yields a methanol-rich molar phase fraction of $\overline{AB} / \overline{ABC}$ ***. Likewise, the cyclohexane-rich phase fraction is*** $\overline{BC} / \overline{ABC}$ ***. A similar relation exists for the volumetric phase fraction when the abscissa is volume fraction rather than mole fraction.***

4.2.2 Dynamic Light Scattering Results

Most of the DLS data were taken from a single sample at a nominal concentration of 0.2 wt% PB-*b*-PEO in the binary solvent at its critical composition (51.7 mol% methanol in cyclohexane on a polymer-free basis).[22] The primary reason for focusing on the critical solvent composition is that it yields approximately equal volumes of each phase at temperatures moderately below the UCST, which allowed both the upper and lower phases of the same sample to be analyzed. Solvent compositions significantly different from the critical composition had to be cooled well below the UCST before the minority phase volume was large enough to be analyzed by DLS.

A second reason for focusing on the critical solvent composition is that the copolymer concentrations in the daughter phases are functions of the bulk solvent composition, as discussed in Section 4.2.1. If the results for samples containing "off-critical" solvent composition are not evaluated carefully, erroneous conclusions could be made, since multiple variables (*e.g.* phase composition, relative phase fraction, copolymer concentration, temperature, *etc*.) are changing simultaneously.

Determination of the viscosities of the coexisting liquid phases is described in Appendix A.

After addition of the copolymer (which acts as an emulsifier) to the binary solvent system, the similar densities of methanol and cyclohexane resulted in very long relaxation times for phase separation. At room temperature, phase separation required weeks or months, depending on the copolymer concentration. Near the

UCST, relaxation times were on the order of several hours, such that samples had to be left overnight in the DLS sample holder at the temperature of interest.

4.2.2.1 Critical Solvent Composition

DLS results for the critical solvent composition are plotted as a function of temperature in Figure 4.12 and interpreted pictorially as an overlay to the binary solvent phase diagram[51] in Figures 4.13 and 4.14. The data are also presented in Table 4.6. In the lower, methanol-rich phase, the hydrodynamic radii appear to increase as temperature decreases, while the opposite is observed in the upper, cyclohexane-rich phase.

In the lower, methanol-rich phase, unimers could be detected for samples at or below 40 ^{o}C only. This complicates the interpretation of the results somewhat since, for the higher temperatures, the decay rate, Γ, may be an average of the micelle Γ and the unimer Γ. Therefore, the presence of undetected unimers may artificially depress the calculated hydrodynamic radii, so it is unclear if the decrease in hydrodynamic radius between 39.5 ^{o}C and 42 ^{o}C is real or artificial. However, it is likely that the micelle radii do decrease with increasing temperature since the solvent becomes less favorable for the PEO corona due to increasing cyclohexane concentration.

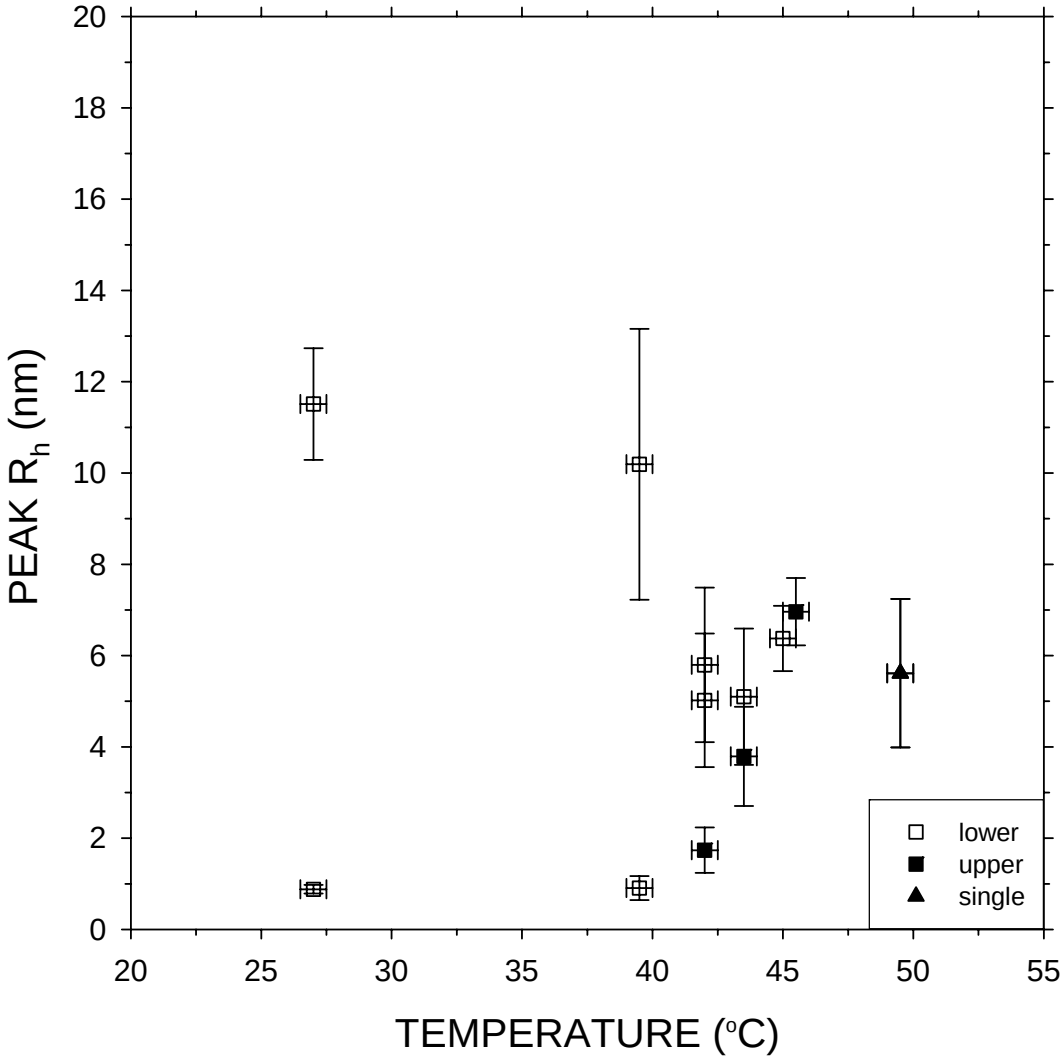

Figure 4.12: The hydrodynamic radii in the lower, methanol-rich phase appear to decrease with temperature while the opposite is true in the upper, cyclohexane-rich phase. Contrary to our hypothesis, micelles are present above the UCST.

Interpretation of the upper, cyclohexane-rich phase and single phase results is even less straightforward. We hypothesized that the upper phase would contain reverse micelles at all temperatures and that, above the UCST, the solvent would contain no micelles. In fact, the data show that micelles exist in the upper phase only a few degrees below the UCST and then disappear below 42 °C. Also, it appears that

micelles do exist above the UCST. Two interpretations of the data are presented in Figures 4.13 and 4.14, where blue indicates the PB-block and red indicates the PEO-block. The relative micelle sizes are approximately to scale.

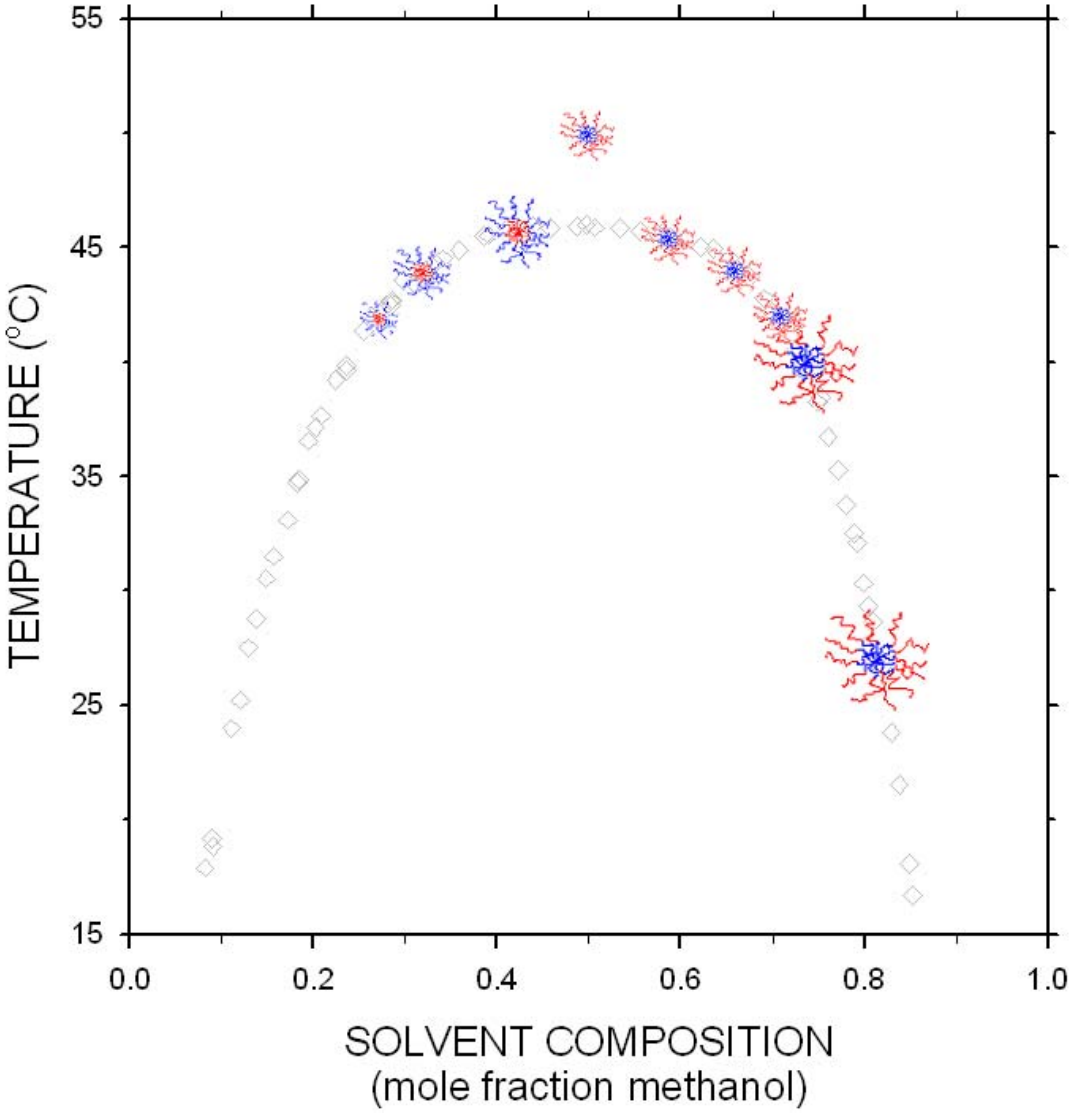

Figure 4.13: This interpretation assumes (as indicated by chemical intuition) that regular micelles (red PEO-corona) form in the methanol-rich phase and reverse micelles (blue PB-corona) form in the cyclohexane-rich phase. Although shown as a regular micelle, the conformation of the micelle above the UCST is unknown. Micelle sizes are approximately scaled to the measured hydrodynamic radii.

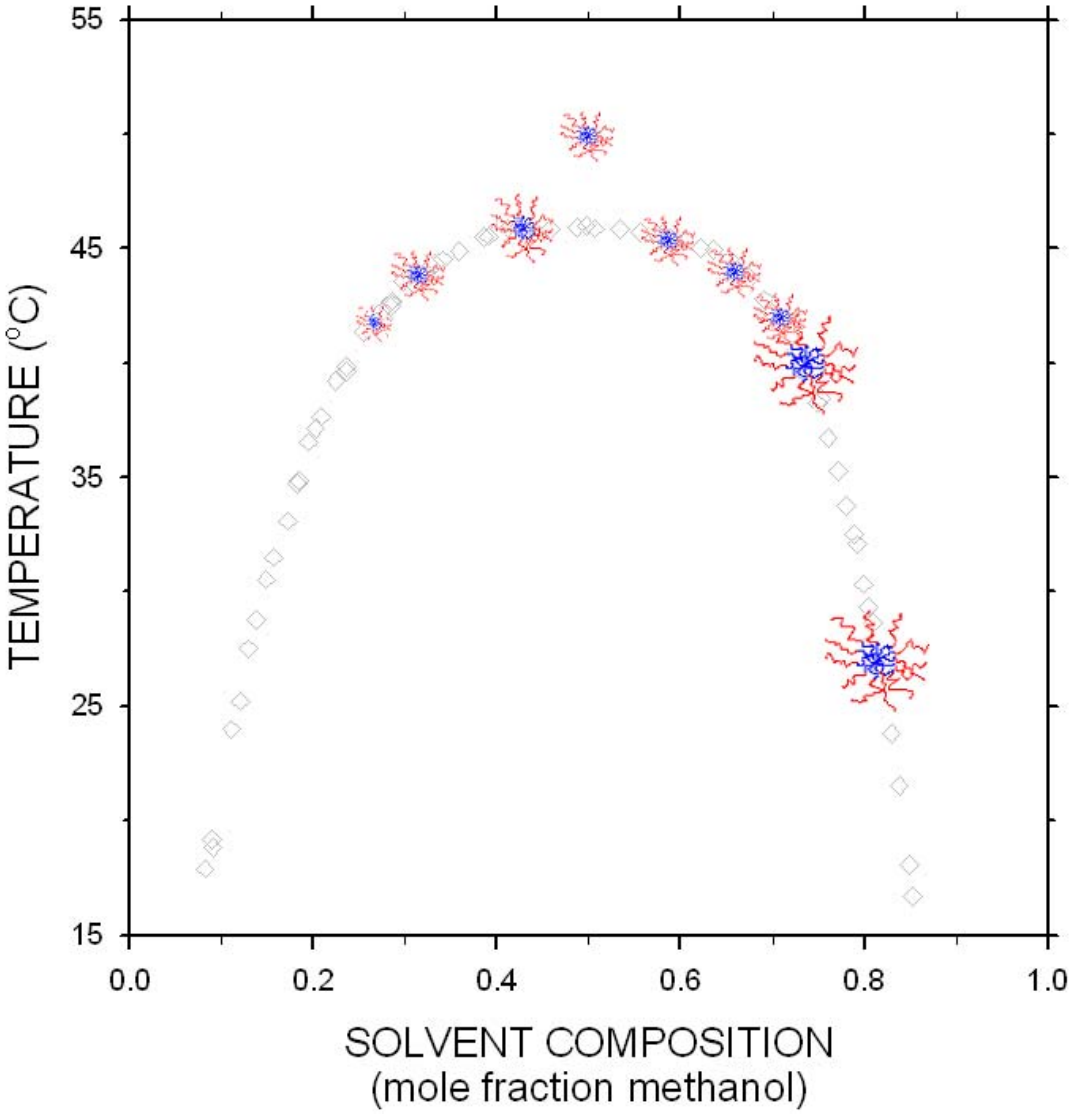

Figure 4.14: This interpretation assumes that regular micelles (red PEO-corona) form in both the methanol-rich phase, the cyclohexane-rich phase, and the single-phase solution at the critical composition. Micelle sizes are approximately scaled to the measured hydrodynamic radii.

Chemical intuition supports the interpretation shown in Figure 4.13, which assumes that reverse micelles form in the cyclohexane-rich phase. However, if this is correct, it is difficult to understand why the micelles disappear as the temperature

decreases, which increases the cyclohexane composition in the cyclohexane-rich phase and should favor the formation of reverse micelles.

An alternative interpretation is shown in Figure 4.14. Here it is assumed that regular micelles are formed in both phases. The basis of this interpretation is the assumption that even small compositions of methanol in the cyclohexane-rich phase may render the solvent unfavorable for the PB block. At elevated temperatures near the UCST, the methanol composition of the cyclohexane-rich phase may be high enough to cause the formation of regular micelles.

The presence of micelles above the UCST can also be explained by this interpretation if the methanol concentration at the critical composition is high enough to make the single-phase solvent unfavorable for the PB block.

It is important to consider that the copolymer concentration ratio increasingly favors the methanol-rich phase as temperature decreases (Figure 4.9). Therefore, at low temperature, regardless of which interpretation is correct, it is likely that either the copolymer concentration in the cyclohexane-rich phase is below the CMC or that the micelle concentration is too low to be detected by DLS.

Without more data, it is impossible to determine which interpretation is correct. Also, even if the first interpretation is correct, the conformation of the micelles above the UCST remains unclear since the single-phase solvent was not expected to be selective for either block.

4.2.2.2 Off-Critical Solvent Composition

In order to investigate the effect of bulk solvent composition on micelle formation in the binary system, two off-critical samples (33.4 mol% methanol in cyclohexane and 67.3 mol% methanol in cyclohexane on a polymer-free basis, both at ~0.2 wt% PB-*b*-PEO) were analyzed at both room temperature and 42 ^{o}C. The cyclohexane-rich sample yielded small volumes for the methanol-rich phase and the methanol-rich sample yielded small volumes for the cyclohexane-rich phase. Therefore, the copolymer concentration in each daughter phase differs from the critical composition sample. It was hoped that this would allow micelles to form more readily in the upper, cyclohexane-rich phase.

Figure 4.15 and Table 4.6 compare the DLS results for the lower, methanol-rich phase of the cyclohexane-rich, critical, and methanol-rich samples. No micelles were found in the upper phase for any of the samples at room temperature. The upper phase of the critical sample (51.7 mol% methanol) at elevated temperature has been discussed previously. The upper phase of the cyclohexane-rich sample exhibited no micelles at 42 ^{o}C and there was insufficient upper phase volume to analyze the methanol-rich sample by DLS at 42 ^{o}C.

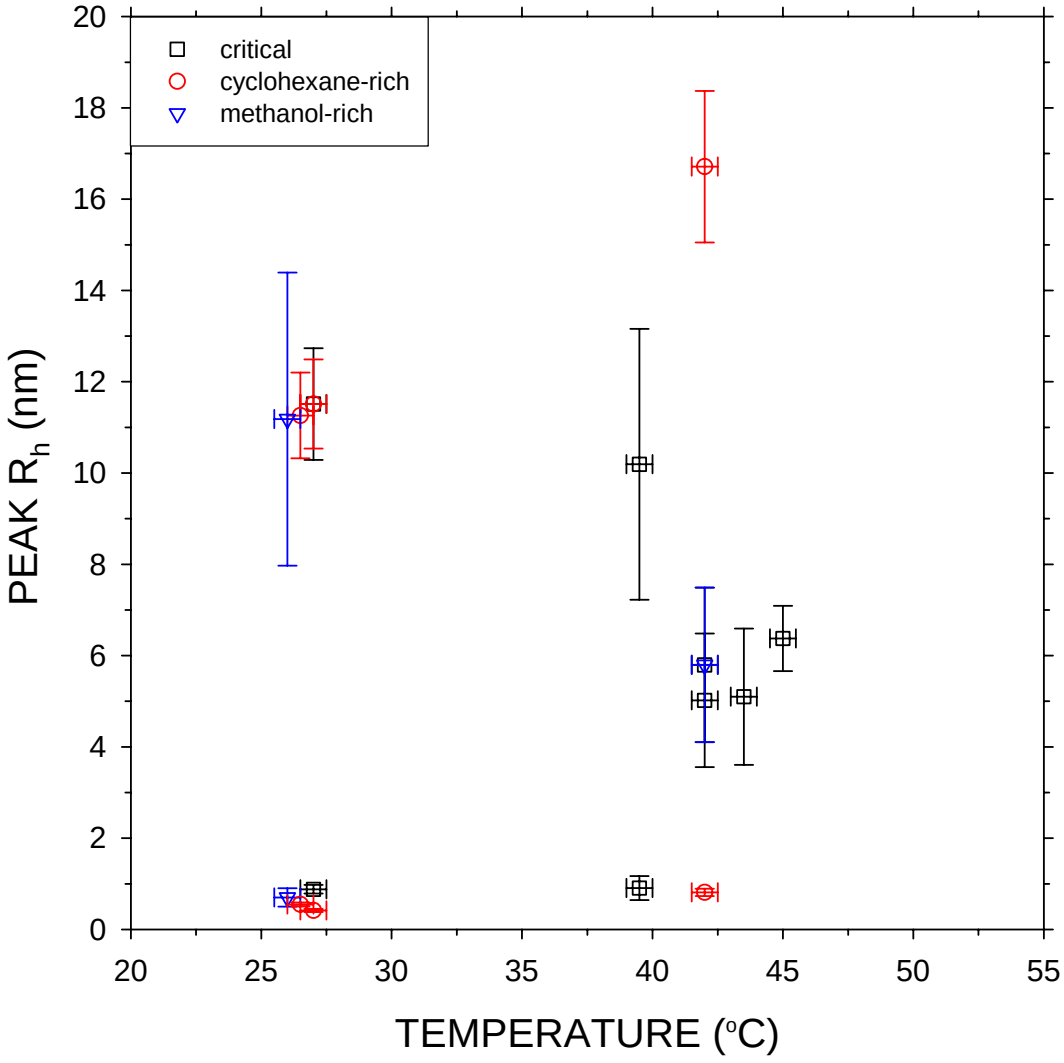

Figure 4.15: Hydrodynamic radii detected in the lower, methanol-rich phase as a function of temperature for several solvent compositions. The methanol-rich and critical solvent composition samples display similar behavior, but the cyclohexane-rich sample contains significantly larger micelles at elevated temperature. As discussed in the text, this may be due to the high copolymer concentration in the minority, methanol-rich phase of the cyclohexane-rich sample.

At room temperature, the lower phases of all samples exhibited micelles of similar hydrodynamic radii. However, at 42 °C (near the phase transition temperature

for both off-critical samples) the lower, methanol-rich phase of the cylohexane-rich sample yielded larger micelles than the other samples.

A possible explanation for the large micelle size in this sample is that the effect of changing bulk solvent composition is to change the relative volumes of the two phases and the copolymer concentration in each phase. Specifically, increasing the bulk cyclohexane composition acts to decrease the volume of the lower, methanol-rich phase. Since the methanol-rich phase is preferred by the copolymer , it may be considerably more concentrated than the bulk concentration. Increased copolymer concentration in this system may favor the formation of larger micelles.

It is interesting that cylindrical micelles were observed in both pure solvents, but only spherical micelles were observed in the binary solvent system, regardless of temperature and bulk solvent composition.

						Unimer			Micelle		
Sample	Run Name	Copolymer Concentration	Solvent Composition	Phase	T	peak	mean	uncertainty	peak	mean	uncertainty
-	-	wt%	mol% methanol	-	C	nm	nm	nm	nm	nm	nm
MC3	MC326L	0.19	33.4	lower	26.5	0.55	0.46	0.05	11.3	10.5	0.9
MC3	MC3L27	0.19	33.4	lower	27	0.41	0.39	0.04	11.5	10.8	1.0
MC3	mc3l422	0.19	33.4	lower	42	0.81	0.70	0.08	16.7	18.5	1.7
MC4	MC4L27	0.19	51.7	lower	27	0.88	0.77	0.09	11.5	11.3	1.2
MC4	mc4l403	0.19	51.7	lower	39.5	0.91	0.88	0.26	10.2	10.3	3.0
MC4	mc4l428	0.19	51.7	lower	42	-	-	-	5.8	5.7	1.7
MC4	mcl423	0.19	51.7	lower	42	-	-	-	5.0	4.3	1.5
MC4	MC4L43.5 (3)	0.19	51.7	lower	43.5	-	-	-	5.1	5.2	1.5
MC4	MC4L45 (3)	0.19	51.7	lower	45	-	-	-	6.4	6.4	0.7
MC4	MC4S49.5 15 min	0.19	51.7	single	49.5	-	-	-	5.6	5.4	1.6
MC4	MC4S49.5 30 min	0.19	51.7	single	49.5	-	-	-	5.6	5.5	1.6
MC4	mc4u_426	0.19	51.7	upper	42	-	-	-	1.7	2.4	0.5
MC4	MC4U43.5	0.19	51.7	upper	43.5	-	-	-	3.8	4.8	1.1
MC4	MC4U45.5 (1)	0.19	51.7	upper	45.5	-	-	-	7.0	7.4	0.7
MC5	MC5L26_2	0.20	67.3	lower	26	0.70	?	0.20	11.2	11.9	3.2
MC5	mc5l422	0.20	67.3	lower	42	-	-	-	5.8	8.0	1.7

Table 4.6: Hydrodynamic radii of PB-b-PEO assemblies in the binary solvent system from DLS.

Chapter 5: Discussion

5.1 Conclusions

Molecular probe experiments in the two pure solvents have shown that PB-*b*-PEO forms regular micelles in methanol and reverse micelles in cyclohexane. By analogy to cryo-TEM results for a similar PB-*b*-PEO copolymer in water,[7] it seems likely that the large and small hydrodynamic radii measured by DLS in the pure solvents are cylindrical and spherical micelles, respectively.

DLS results in the binary solvent system indicate that, near the UCST, spherical micelles exist in both the upper, cyclohexane-rich and in the lower, methanol-rich phases. Micelles also exist in the single-phase region above the UCST at the critical solvent composition. As the temperature decreases below the UCST, micelles disappear from the cyclohexane-rich phase but remain in the methanol-rich phase. SEC results indicate that the copolymer distributes preferentially into the methanol-rich phase as the temperature decreases, which explains the absence of micelles in the cyclohexane-rich phase (*i.e.*, the copolymer concentration in the cyclohexane-rich phase is below the CMC or, at least, below the DLS detection limit).

5.2 Recommendations for Future Work

One of the most interesting questions raised by the results of this work relates to the conformation (*i.e.*, regular or reverse) of the micelles in the upper, cyclohexane-rich phase near the UCST. More information could be gained from a

contrast-matched small angle neutron scattering study of the system, which would require one block of the copolymer to be deuterated while the other remains hydrogenated. This would allow determination of the conformation of the micelles. If the copolymer was also studied in the pure solvents, the micelle shapes (*i.e.*, spherical and cylindrical) could also be confirmed.

Ideally this work would have used a copolymer that had equal affinity for the upper and lower phases instead of preferentially distributing into the lower, methanol-rich phase. If the copolymer distributed more evenly, we expect that both phases would exhibit micelles over a wider temperature range. One strategy for achieving even distribution would be to increase the number of PB segments in order to equal or exceed the number of PEO segments. However, it is not immediately clear that this will achieve the desired result.

Although it may be very difficult to find such a system, a theoretically better approach might be to select the UCST-forming binary solvent system such that the pure solvents are each the monomer of one of the copolymer blocks. In this case, we expect that a block copolymer with an equal number of repeating units of each block would distribute nearly equally between the phases and give a better indication of general behavior of amphiphiles near the UCST of a partially-miscible binary solvent system.

Due to long relaxation times for the present binary solvent system after addition of the copolymer, future work on amphiphilic copolymers in binary solvents would be easier if the components of the binary solvent exhibited a greater difference in density. One potential system is fully deuterated methanol and hydrogenated

cyclohexane. The density of deuterated methanol is significantly larger than that of hydrogenated methanol, but the results should be qualitatively similar to those presented here. However, some quantitative differences are expected due to increased hydrogen-bond strength in deuterated methanol.[52]

Appendices

Appendix A: Measurement of Viscosities in Coexisting Liquid Phases

We were unable to find published data for the viscosities of the coexisting liquid phases in the binary solvent. Since this is a crucial parameter required for the analysis of DLS data, *a priori* estimation methods were not deemed to be accurate enough for our purposes. Therefore, it was necessary to measure the dynamic viscosities as functions of temperature (where the dynamic viscosity for a Newtonian fluid is defined as the constant of proportionality relating the shear stress to the velocity gradient).[53] While many viscometry techniques are available, we elected to use capillary tube viscometry and, in the lower, methanol-rich phase, DLS measurement of silica particles of known size, since both techniques were available and the employment of a second technique would allow independent verification of the results.

The following procedure was used to measure the viscosities using capillary tube viscometry. A beaker containing a magnetic stirrer bar and coexisting methanol and cyclohexane at the critical composition (51.7 mol% methanol) was placed over a submersible stirrer in the reservoir of the Neslab RTE-111 constant temperature bath, along with a Cannon-Fenske Size 100 capillary tube viscometer and a 25-mL graduated cylinder. The binary solvent was stirred while the system was brought to the desired temperature.

After allowing sufficient time for phase-separation, the appropriate volume of the upper, cyclohexane-rich phase was removed with a pipette and placed into the

viscometer, where it was allowed to return to the system temperature. The flow time through the viscometer was measured three to five times until a consistent set of three measurements was obtained. Multiplication by the viscometer constant (previously determined using distilled water) yielded the kinematic viscosity of the sample (where kinematic viscosity is the ratio of the dynamic viscosity to the density).[53]

A second sample of the upper phase was removed from the beaker and placed into the graduated cylinder. Excess sample was removed in order to achieve a 10-mL volume. The exterior of the previously-tared graduated cylinder was carefully dried and weighed in order to determine the density of the sample. Multiplication of the kinematic viscosity by the measured density yielded the dynamic viscosity of the sample.

The above procedure was repeated for the lower, methanol-rich phase prior to moving on to the next temperature.

The viscosity of the lower, methanol-rich phase was verified using DLS to measure the hydrodynamic radius of particles of known size, as proposed by Anisimov, *et al*. [54] and implemented by Will and Leipertz.[55] For this work, silica particles of a narrow size distribution were suspended in both methanol and the binary solvent at the critical composition. It was known from previous work by Park and DeShong[56] that the particles were not soluble in cyclohexane nor in the upper, cyclohexane-rich phase. Therefore, only the lower phase viscosity can be measured by this procedure.

The viscosity of pure methanol is well-known.[44] Therefore, the hydrodynamic radius of the particles was first measured by DLS in methanol at each temperature of

interest. The diffusion coefficient of the particles in the lower phase was also measured by DLS. The lower-phase solvent viscosity was then calculated from the hydrodynamic radius measured in pure methanol using the Stokes-Einstein equation.[37, 40] Since the silica particle size distribution is slightly asymmetric, as shown in Figure A.1, the solvent viscosity that matched the mean radius is slightly different from the viscosity that matched the peak radius, so both sets of results are presented.

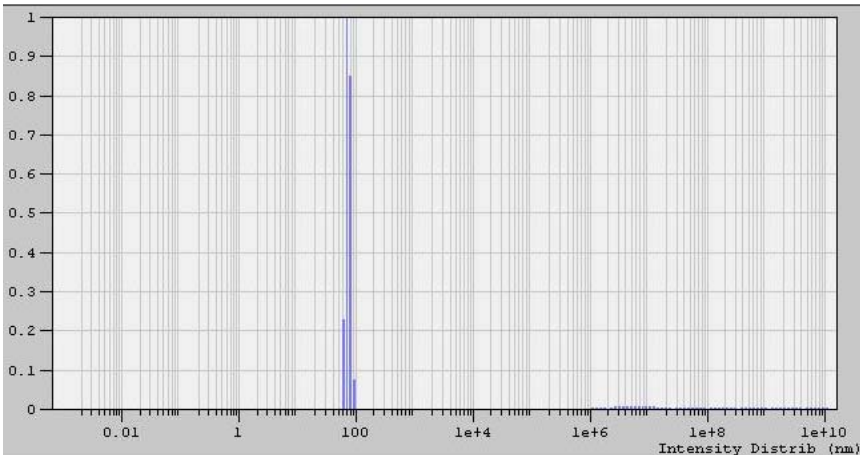

Figure A.1: DLS analysis of the silica particles indicates that the size distribution is slightly asymmetric.

The results for both viscometry methods are shown in Figure A.2 and Table A.1. The viscosities of pure methanol[44] and cyclohexane[43] are also plotted.

It is impossible to calculate the uncertainty in the viscosity measured by the capillary tube viscometry method because the largest experimental error, *viz*. nucleation of the second phase in the viscometer, is not quantifiable. Therefore, we estimate that the measured viscosities are accurate to within ±0.05 cP. Given the

relatively small variation of the viscosities with temperature, we believe that this is a conservative estimate.

Capillary tube viscometry yielded smoother results than DLS. For this reason and because the DLS method was capable of measuring only the methanol-rich phase viscosity, the capillary tube viscometry results were used for analysis of all DLS data for the binary solvent system. However, the viscosity data obtained from the DLS method generally agree with the capillary tube viscometry data to within the assumed uncertainty, which validates the uncertainty estimate and indicates that both methods are suitable.

	Lower			Upper	Single
T	CTV	DLS (P)	DLS (M)	CTV	CTV
C	cP	cP	cP	cP	cP
23	0.62	-	-	0.86	-
26	-	0.56	0.60	-	-
26	-	0.56	0.58	-	-
30	0.58	-	-	0.73	-
33.5	-	0.51	0.59	-	-
40	0.52	0.56	0.58	0.63	-
42	0.51	0.55	0.50	0.62	-
44	0.50	-	-	0.60	-
46	-	-	-	-	0.60
48	-	-	-	-	0.57
50	-	-	-	-	0.55

Table A.1: Experimental viscosities of the coexisting phases by capillary tube viscometry (CTV) and dynamic light scattering (DLS). The uncertainty (99% confidence interval) in the CTV results is estimated to be ±0.05 cP. The DLS data were evaluated using both the peak (P) hydrodynamic radius and the mean (M) hydrodynamic radius. The uncertainty in the DLS results has not been evaluated.

The DLS-derived data show significant scatter and internal disagreement between the two methods of analysis (peak vs. mean). The source of the scatter is

unclear, but disagreement between the two methods of analysis is believed to stem from the asymmetry of the silica particle size distribution.

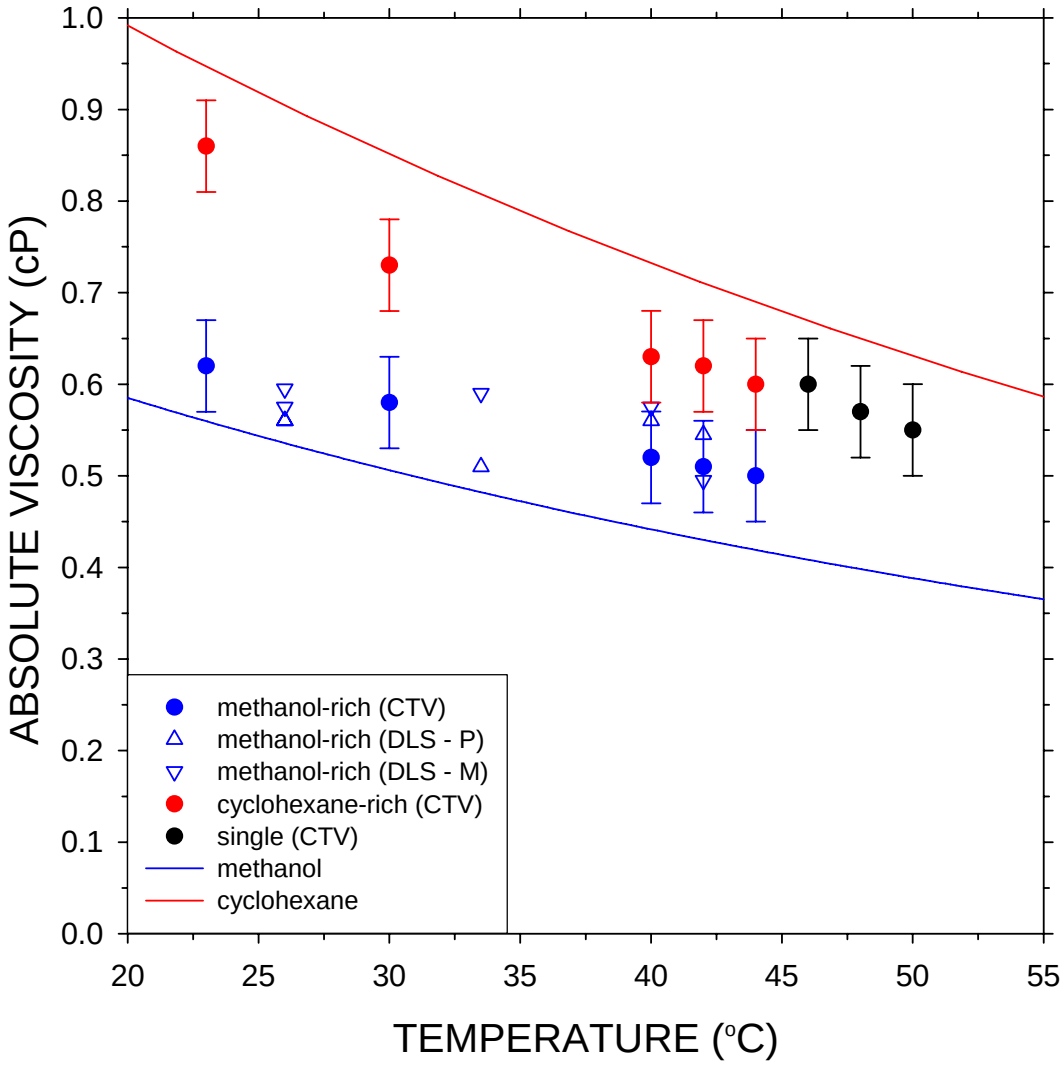

Figure A.2: Viscosities of the coexisting phases were measured by capillary tube viscometry (CTV) and, in the methanol-rich phase only, dynamic light scattering (DLS). The methanol-rich phase viscosity was estimated using both the peak (P) hydrodynamic radius and the mean (M) hydrodynamic radius. Pure component viscosities[43, 44] are provided for reference.

Appendix B: Uncertainty Propagation in Dynamic Light Scattering Analysis

The uncertainty, u_{R_h} (equivalent to a 99% confidence interval), in the hydrodynamic radius, R_h, calculated from a set of DLS data can be found from equation (B.1),[57] where u_i represents the uncertainty in each experimental value.

$$u_{R_h} = \sqrt{\sum_{i=1}^{n}\left(\frac{\partial R_h}{\partial i}u_i\right)^2} \tag{B.1}$$

Rearrangement of equations (3.6) – (3.8) to solve for R_h results in equation (B.2), where all of the variables have been previously defined in Section 3.4.

$$R_h = \frac{8}{3}\frac{k_B T}{\eta}\frac{\pi n^2}{\lambda^2}\frac{1}{\Gamma}\sin^2\left(\frac{\theta}{2}\right) \tag{B.2}$$

Equation (B.1) can then be expressed as shown below if covariance is neglected:

$$u_{R_h} = R\sqrt{\left(\frac{u_T}{T}\right)^2 + \left(\frac{u_\eta}{\eta}\right)^2 + \left(\frac{2u_n}{n}\right)^2 + \left(\frac{2u_\lambda}{\lambda}\right)^2 + \left(\frac{u_\Gamma}{\Gamma}\right)^2 + \left(\frac{u_\theta}{\tan\left(\frac{\theta}{2}\right)}\right)^2} \tag{B.3}$$

The estimated uncertainty (99% confidence interval) for each experimental variable is shown in Table B.1.

Variable	Unit	Uncertainty
T	K	0.5
η	cP	0.05 / 0.01
n	-	0.0001
λ	nm	3.164
Γ	-	27.5% / 6.5% / 1.25%
θ	degrees	0.01

Table B.1: The uncertainty in each variable corresponds to a 99% confidence interval. The uncertainties in η correspond to the binary solvent system and the pure solvents, respectively. The uncertainty in Γ depends on the mean scattered intensity. The uncertainties shown correspond to the following scattered intensity intervals: (0, 30,000], (30,000, 90,000], and (90,000, ∞).

The uncertainties in T and θ have been discussed previously. Uncertainty in η has been discussed for the binary solvent system, but not the pure solvents, where it is assumed to be ±0.01 cP. Uncertainty in n for the binary solvent system was estimated by Jacobs to be ±0.0001,[22] which is equivalent to the precision generally obtained using an analog Abbe refractometer,[58] so the same uncertainty will be applied to the pure solvent refractive index. Uncertainty in λ is unknown, but was assumed to be 0.5%.

The uncertainty in Γ was found to depend on the mean scattered intensity of the sample. The standard error in Γ was estimated using Sigma Plot version 5.0 (SSPS, Inc.) to make a linear fit to a plot of the natural logarithm of the autocorrelation function versus decay time, where the slope of the fitted line is equal

to $-\Gamma$. The regression results indicate the standard error in the slope, which is equal to the standard error in Γ. The uncertainty in Γ was then assumed to be three times the standard error in order to obtain >99% confidence that Γ falls within the uncertainty interval.

This procedure was carried out for data that had mean scattered intensities of ~9,000 cps, ~30,000 cps, and ~90,000 cps. The uncertainty in Γ was found to be ±27.5%, ±6.5%, and ±1.25% of the fitted Γ, respectively. Therefore, the calculated uncertainty in R_h is applied in a step-wise fashion as a function of the mean scattered intensity of the sample. The highest uncertainty is applied to samples with scattered intensity < 30,000 cps and the lowest uncertainty is applied to samples with scattered intensity > 90,000 cps. The mid-range uncertainty is applied between these limits. A better uncertainty estimate could be obtained if this method were applied with greater resolution, but the present method results in a conservative measure of the propagation of Γ uncertainty in the calculated R_h.

Note that the procedure outlined above for estimating the uncertainty in Γ is valid only for nearly monodisperse samples which present a single exponential decay such that it is valid to represent the data using a single parameter. For polydisperse samples, a more rigorous method is required. However, the results of this method have been applied to all DLS data whether the sample was monodisperse or polydisperse.

It is interesting to compare the relative magnitudes of the various uncertainties on the calculated uncertainty in R_h. For the pure solvent samples, the uncertainty in η is low, so the primary source of uncertainty is Γ. For the binary samples, both Γ and

η contain significant uncertainty. Since the uncertainty in the binary viscosities ranges from ~5% to ~10%, depending on the viscosity, the uncertainty in Γ is controlling for mean scattered intensities below 30,000 cps. Between 30,000 cps and 90,000 cps, the magnitude of the two uncertainties is approximately equal. Above 90,000 cps, the uncertainty in η is controlling. All of the other uncertainties are relatively small compared with the uncertainty in Γ and η.

Appendix C: Evaluated Dynamic Light Scattering Autocorrelation Functions

The DLS results discussed in Chapter 4 are based on the evaluated autocorrelation functions presented here. The methanol results are presented first followed by the cyclohexane and binary solvent results. The results are summarized in Tables C.1-C.3, which also include the physical properties used to analyze the data, *viz*. solvent viscosity and refractive index.

									Unimer		Micelle 1		Micelle 2	
Sample	Run Name	Copolymer Concentration	T	n	η	Intensity	Min Channel	Max Channel	peak	mean	peak	mean	peak	mean
-	-	wt%	C	-	cP	cps	-	-	nm	nm	nm	nm	nm	nm
M1	M125 (2)	0.2	25	1.3297	0.547	66,598	55	120	-	-	16.29	16.85	135.4	134.5
M1	M126	0.2	26	1.3293	0.54	73,198	55	115	0.377	0.351	16.55	17.04	118.2	121.1
M1	M126 b4 son	0.2	26	1.3293	0.54	79,138	55	115	0.377	0.365	16.55	16.85	118.2	111.7
M1	M126.5	0.2	26.5	1.3291	0.54	180,063	55	125	-	-	19.28	19.66	216.8	219
M1	M1_262	0.2	26.5	1.3291	0.54	44,255	55	115	0.511	0.474	16.57	18.13	137.7	135.4
M1	m1_334	0.2	33	1.3265	0.49	108,769	55	120	-	-	18.59	17.07	179.7	181.4
M1	M1_42	0.2	42	1.3229	0.435	97,544	55	120	-	-	18.43	17.08	153.2	155.5
M1	m1_49	0.2	49.5	1.3199	0.395	134,714	55	115	0.985	1.004	17.78	18.3	200	260.1
M4	M4_26	0.10	26.5	1.3291	0.54	21,752	55	200	0.805	0.739	16.57	17.43	341.4	357
M4	m4_333	0.10	33	1.3265	0.49	19,834	55	120	0.573	0.576	18.59	19.66	382.8	479.3
M4	m4_422	0.10	42	1.3229	0.435	21,867	55	120	-	-	18.43	18.67	326.3	354.9
M4	m4_49	0.10	49.5	1.3199	0.395	26,888	55	115	0.742	0.709	17.78	17.7	270.6	347.1
M5	m5_261	0.050	26.5	1.3291	0.54	19,358	55	205	0.936	0.869	19.28	18.25	537.4	543.4
M5	m5_333	0.050	33.5	1.3263	0.485	17,621	55	120	-	-	18.8	20.06	286.2	338.4
M5	m5_423	0.050	42	1.3229	0.435	15,113	55	120	0.895	0.841	18.43	20.09	207.3	250.6
M5	m5_491	0.050	49.5	1.3199	0.395	21,523	55	115	0.638	0.613	17.78	18.25	232.6	260.2

Table C.1: DLS results for pure methanol.

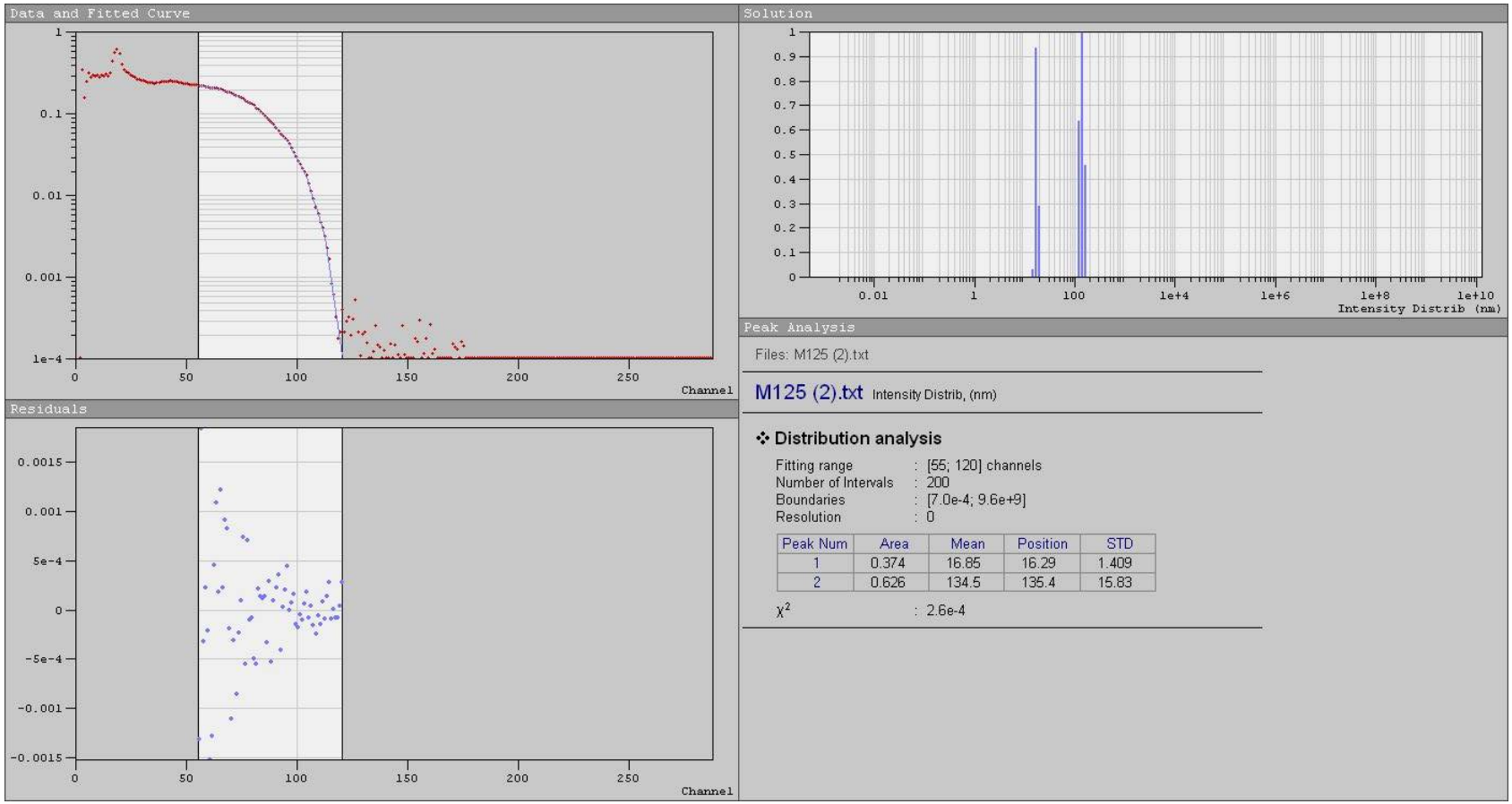
Data and Fitted Curve
1
0.1
0.01
0.001
1e-4
0
50
100
150
200
250
Channel
Residuals
0.0015
0.001
5e-4
0
-5e-4
-0.001
-0.0015
0
50
100
150
200
250
Channel
Solution
1
0.9
0.8
0.7
0.6
0.5
0.4
0.3
0.2
0.1
0
0.01
1
100
1e+4
1e+6
1e+8
1e+10
Intensity Distrib (nm)
Peak Analysis
Files: M125 (2).txt
M125 (2).txt Intensity Distrib, (nm)
Distribution analysis
Fitting range : [55; 120] channels
Number of Intervals : 200
Boundaries : [7.0e-4; 9.6e+9]
Resolution : 0
Peak Num | Area | Mean | Position | STD
1 | 0.374 | 16.85 | 16.29 | 1.409
2 | 0.626 | 134.5 | 135.4 | 15.83
χ² : 2.6e-4

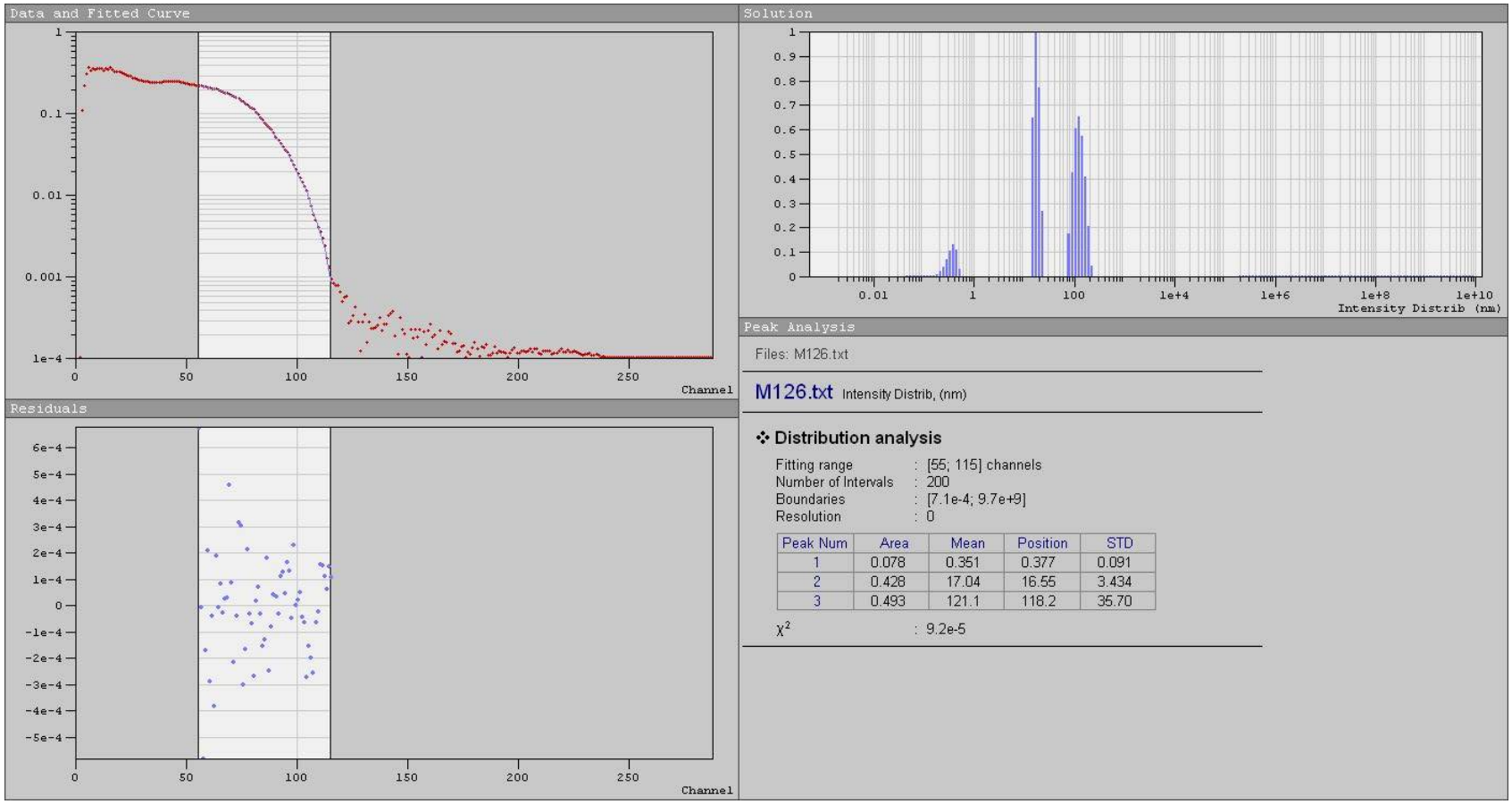
Data and Fitted Curve
1
0.1
0.01
0.001
1e-4
0
50
100
150
200
250
Channel
Residuals
6e-4
5e-4
4e-4
3e-4
2e-4
1e-4
0
-1e-4
-2e-4
-3e-4
-4e-4
-5e-4
0
50
100
150
200
250
Channel
Solution
1
0.9
0.8
0.7
0.6
0.5
0.4
0.3
0.2
0.1
0
0.01
1
100
1e+4
1e+6
1e+8
1e+10
Intensity Distrib (nm)
Peak Analysis
Files: M126.txt
M126.txt Intensity Distrib, (nm)
Distribution analysis
Fitting range : [55; 115] channels
Number of Intervals : 200
Boundaries : [7.1e-4; 9.7e+9]
Resolution : 0
Peak Num | Area | Mean | Position | STD
1 | 0.078 | 0.351 | 0.377 | 0.091
2 | 0.428 | 17.04 | 16.55 | 3.434
3 | 0.493 | 121.1 | 118.2 | 35.70
χ² : 9.2e-5

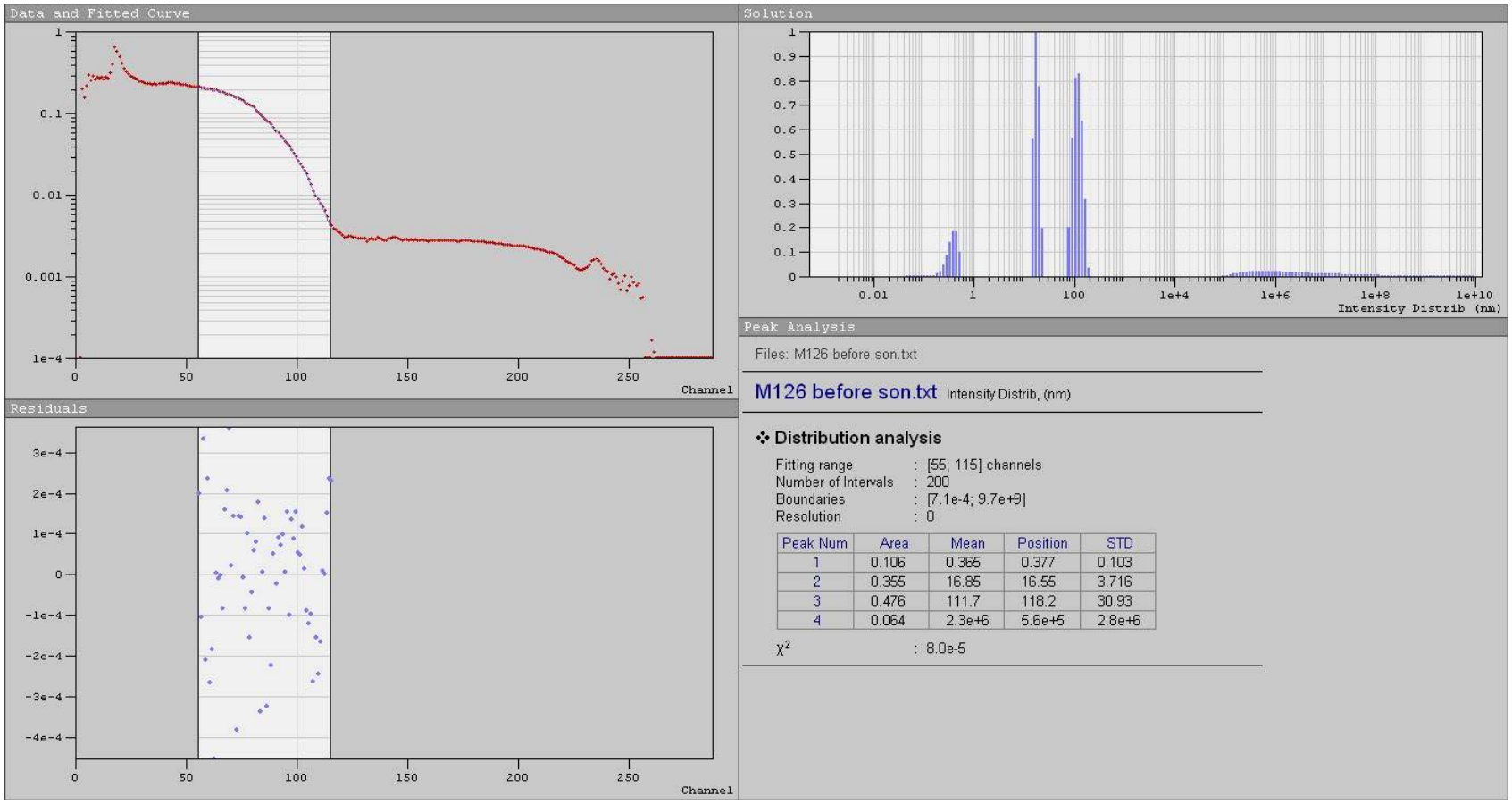
Data and Fitted Curve
1
0.1
0.01
0.001
1e-4
0
50
100
150
200
250
Channel
Residuals
3e-4
2e-4
1e-4
0
-1e-4
-2e-4
-3e-4
-4e-4
0
50
100
150
200
250
Channel
Solution
1
0.9
0.8
0.7
0.6
0.5
0.4
0.3
0.2
0.1
0
0.01
1
100
1e+4
1e+6
1e+8
1e+10
Intensity Distrib (nm)
Peak Analysis
Files: M126 before son.txt
M126 before son.txt Intensity Distrib, (nm)
Distribution analysis
Fitting range : [55; 115] channels
Number of Intervals : 200
Boundaries : [7.1e-4; 9.7e+9]
Resolution : 0
Peak Num | Area | Mean | Position | STD
1 | 0.106 | 0.365 | 0.377 | 0.103
2 | 0.355 | 16.85 | 16.55 | 3.716
3 | 0.476 | 111.7 | 118.2 | 30.93
4 | 0.064 | 2.3e+6 | 5.6e+5 | 2.8e+6
χ² : 8.0e-5

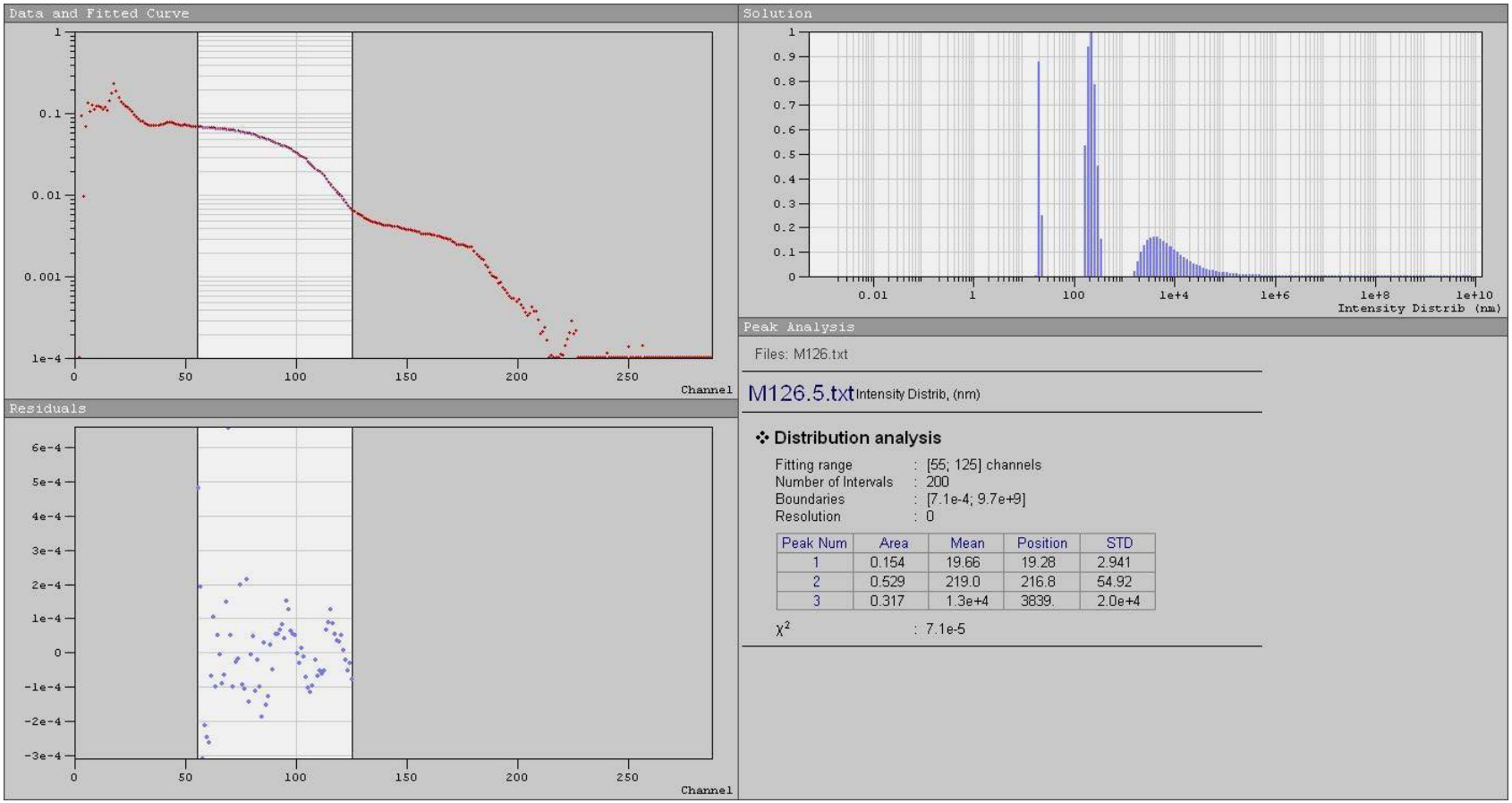
Data and Fitted Curve
1
0.1
0.01
0.001
1e-4
0
50
100
150
200
250
Channel
Residuals
6e-4
5e-4
4e-4
3e-4
2e-4
1e-4
0
-1e-4
-2e-4
-3e-4
0
50
100
150
200
250
Channel
Solution
1
0.9
0.8
0.7
0.6
0.5
0.4
0.3
0.2
0.1
0
0.01
1
100
1e+4
1e+6
1e+8
1e+10
Intensity Distrib (nm)
Peak Analysis
Files: M126.txt
M126.5.txt Intensity Distrib, (nm)
Distribution analysis
Fitting range : [55; 125] channels
Number of Intervals : 200
Boundaries : [7.1e-4; 9.7e+9]
Resolution : 0
Peak Num | Area | Mean | Position | STD
1 | 0.154 | 19.66 | 19.28 | 2.941
2 | 0.529 | 219.0 | 216.8 | 54.92
3 | 0.317 | 1.3e+4 | 3839. | 2.0e+4
χ² : 7.1e-5

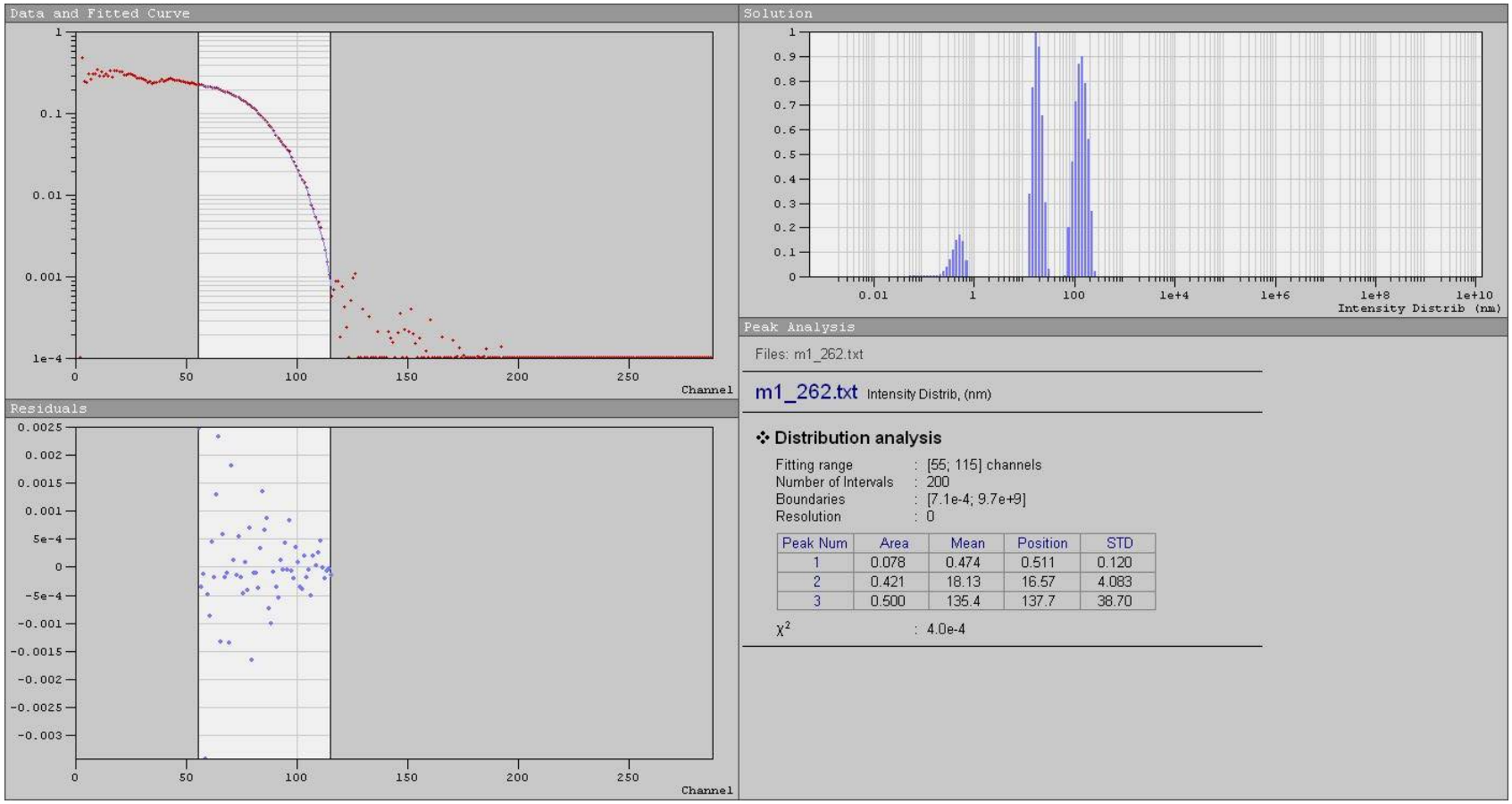
Data and Fitted Curve
Channel
Residuals
Channel
Solution
Intensity Distrib (nm)
Peak Analysis
Files: m1_262.txt
m1_262.txt Intensity Distrib, (nm)
Distribution analysis
Fitting range : [55; 115] channels
Number of Intervals : 200
Boundaries : [7.1e-4; 9.7e+9]
Resolution : 0
Peak Num | Area | Mean | Position | STD
1 | 0.078 | 0.474 | 0.511 | 0.120
2 | 0.421 | 18.13 | 16.57 | 4.083
3 | 0.500 | 135.4 | 137.7 | 38.70
χ² : 4.0e-4

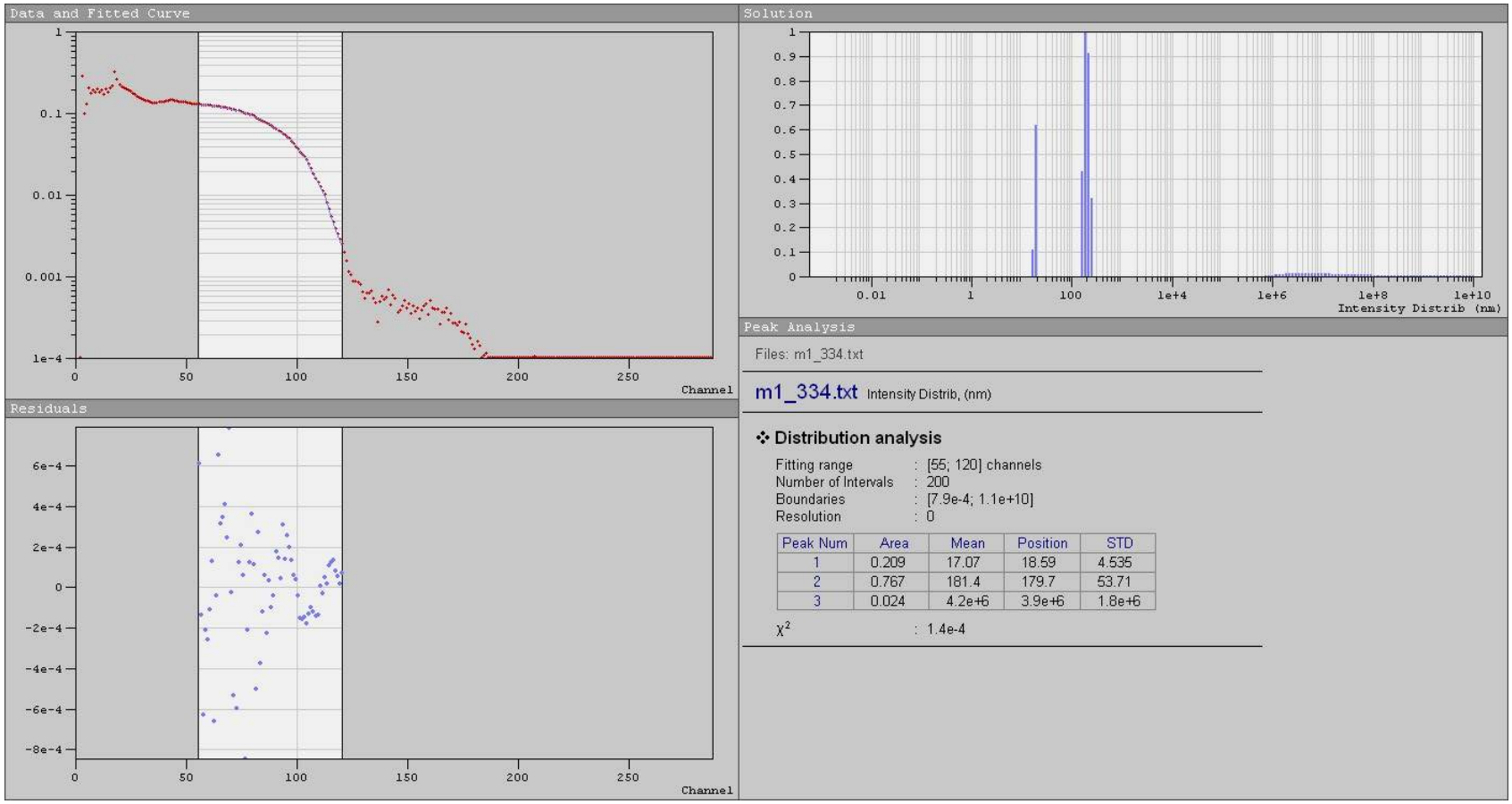
Data and Fitted Curve
Channel
Residuals
Channel
Solution
Intensity Distrib (nm)
Peak Analysis
Files: m1_334.txt
m1_334.txt Intensity Distrib, (nm)
Distribution analysis
Fitting range : [55; 120] channels
Number of Intervals : 200
Boundaries : [7.9e-4; 1.1e+10]
Resolution : 0
Peak Num | Area | Mean | Position | STD
1 | 0.209 | 17.07 | 18.59 | 4.535
2 | 0.767 | 181.4 | 179.7 | 53.71
3 | 0.024 | 4.2e+6 | 3.9e+6 | 1.8e+6
χ² : 1.4e-4

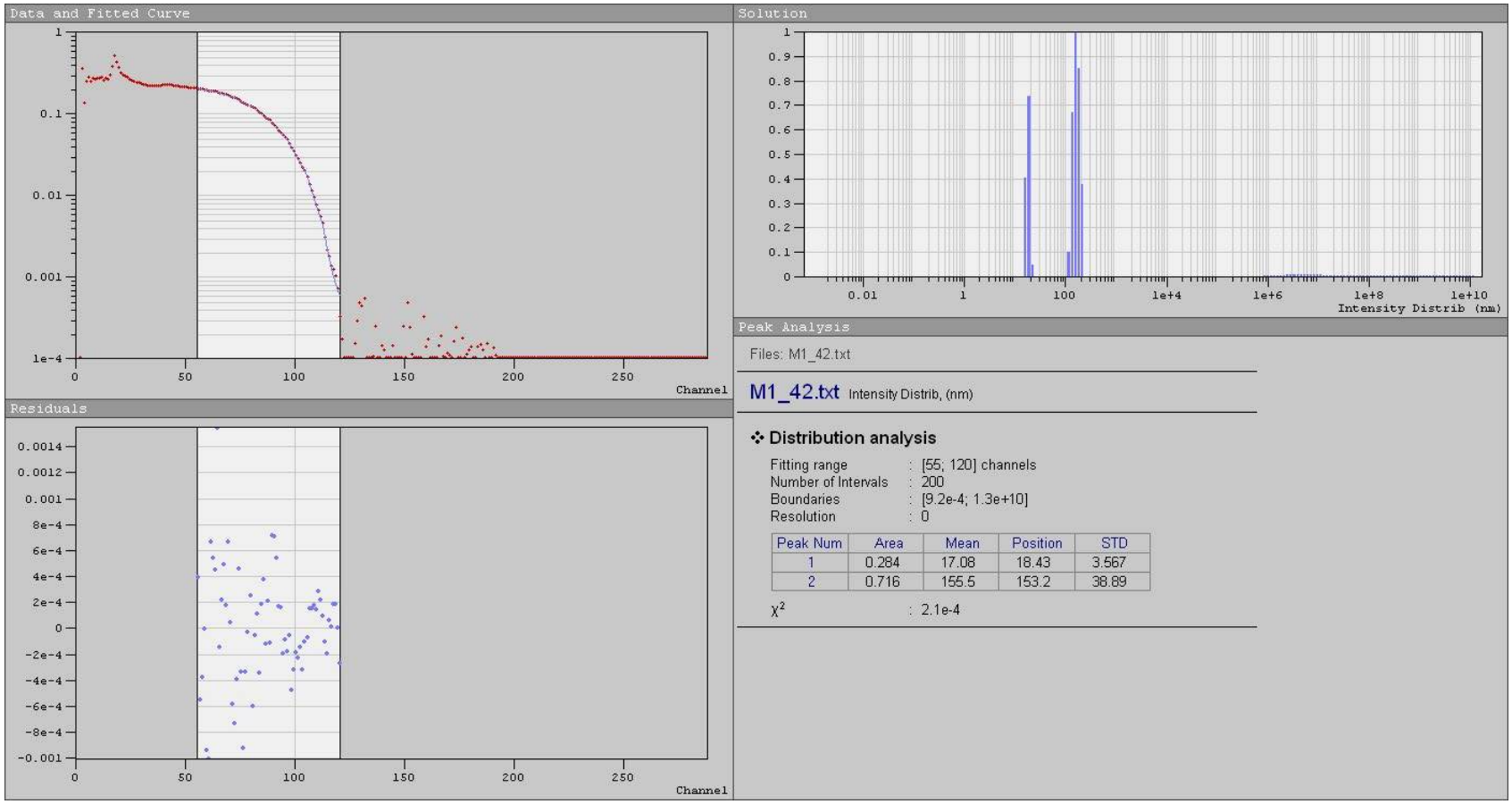
Data and Fitted Curve
Channel
Residuals
Channel
Solution
Intensity Distrib (nm)
Peak Analysis
Files: M1_42.txt
M1_42.txt Intensity Distrib, (nm)
Distribution analysis
Fitting range : [55, 120] channels
Number of Intervals : 200
Boundaries : [9.2e-4; 1.3e+10]
Resolution : 0
Peak Num | Area | Mean | Position | STD
1 | 0.284 | 17.08 | 18.43 | 3.567
2 | 0.716 | 155.5 | 153.2 | 38.89
χ² : 2.1e-4

Data and Fitted Curve

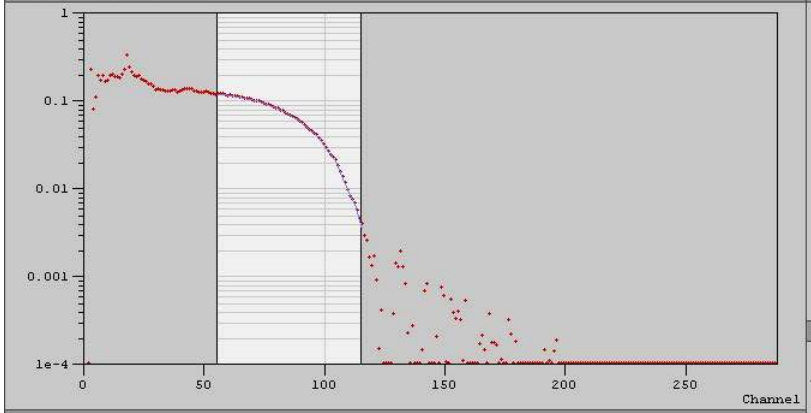

Residuals

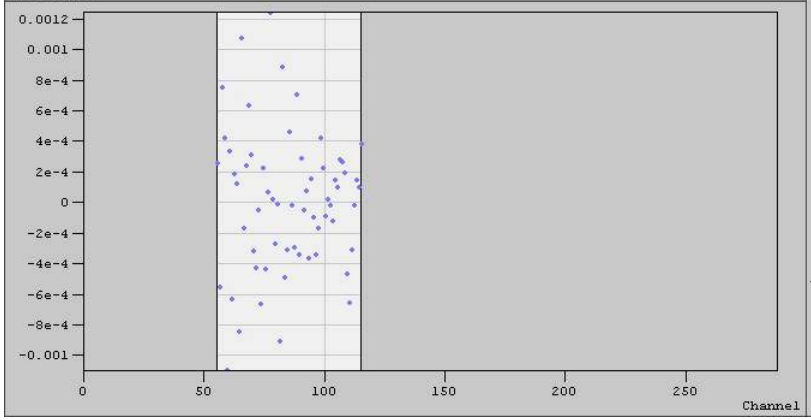

Solution

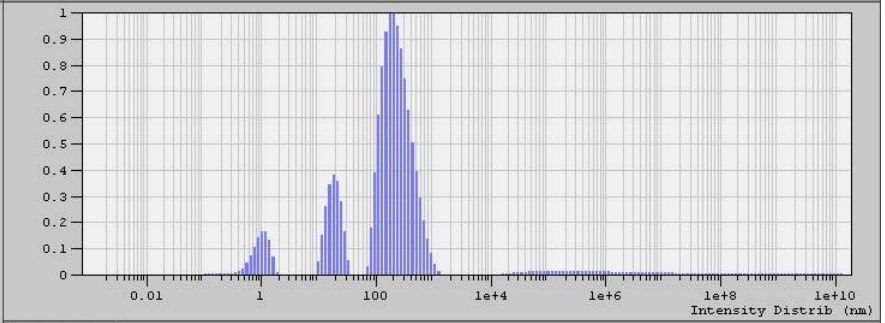

Peak Analysis

Files: m1_49.txt

m1_49.txt Intensity Distrib, (nm)

❖ Distribution analysis

Fitting range : [55; 115] channels
Number of Intervals : 200
Boundaries : [0.001; 1.4e+10]
Resolution : 0.250

Peak Num	Area	Mean	Position	STD
1	0.071	0.985	1.004	0.332
2	0.158	18.30	17.78	5.984
3	0.756	260.1	200.0	173.0
4	0.016	2.5e+5	1.6e+5	1.9e+5

χ^2 : 2.1e-4

Data and Fitted Curve

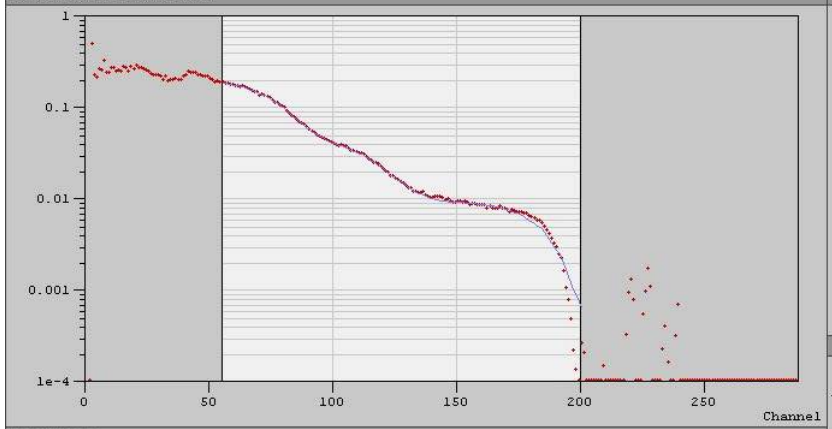

Residuals

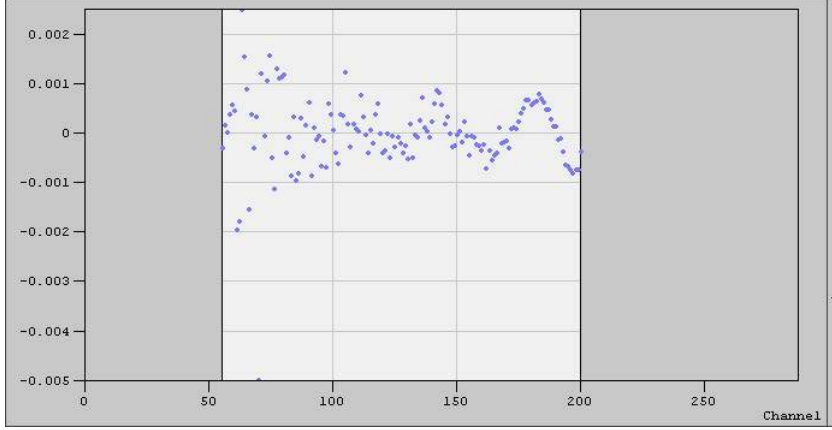

Solution

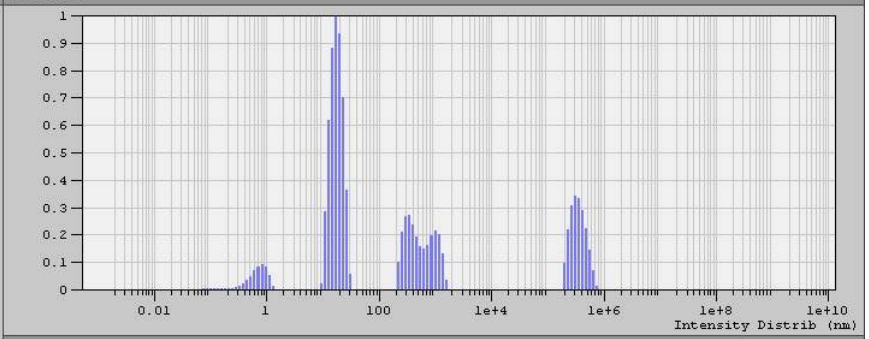

Peak Analysis

Files: M4_26.txt

M4_26.txt Intensity Distrib, (nm)

❖ Distribution analysis

Fitting range : [55; 200] channels
Number of Intervals : 200
Boundaries : [7.1e-4; 9.7e+9]
Resolution : 0

Peak Num	Area	Mean	Position	STD
1	0.050	0.739	0.805	0.226
2	0.492	17.43	16.57	4.603
3	0.145	357.0	341.4	97.14
4	0.109	959.9	984.1	248.8
5	0.204	3.6e+5	3.1e+5	1.2e+5

χ^2 : 5.3e-4

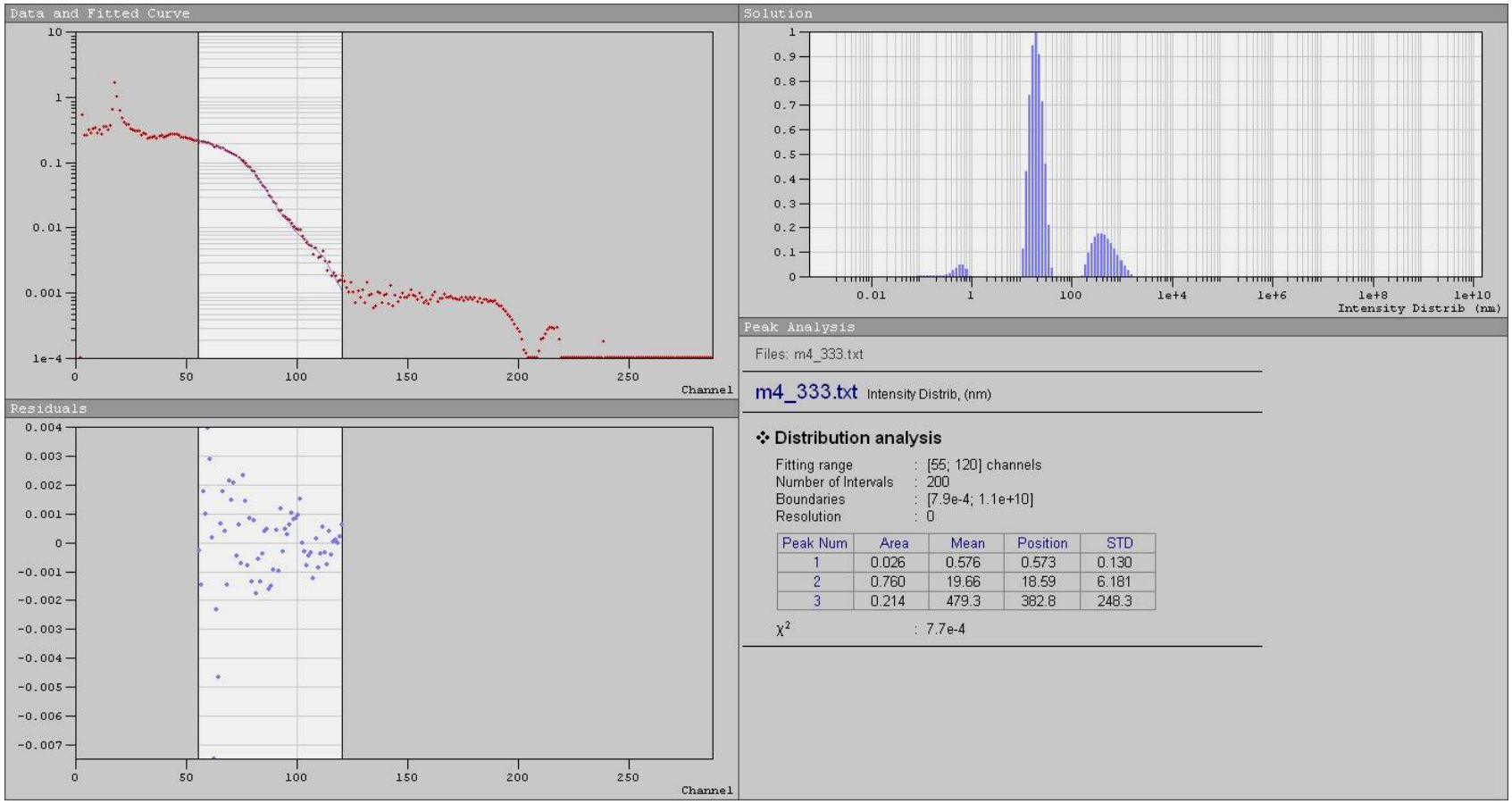
Data and Fitted Curve
Channel
Residuals
Channel
Solution
Intensity Distrib (nm)
Peak Analysis
Files: m4_333.txt
m4_333.txt Intensity Distrib, (nm)
Distribution analysis
Fitting range : [55; 120] channels
Number of Intervals : 200
Boundaries : [7.9e-4; 1.1e+10]
Resolution : 0
Peak Num | Area | Mean | Position | STD
1 | 0.026 | 0.576 | 0.573 | 0.130
2 | 0.760 | 19.66 | 18.59 | 6.181
3 | 0.214 | 479.3 | 382.8 | 248.3
χ² : 7.7e-4

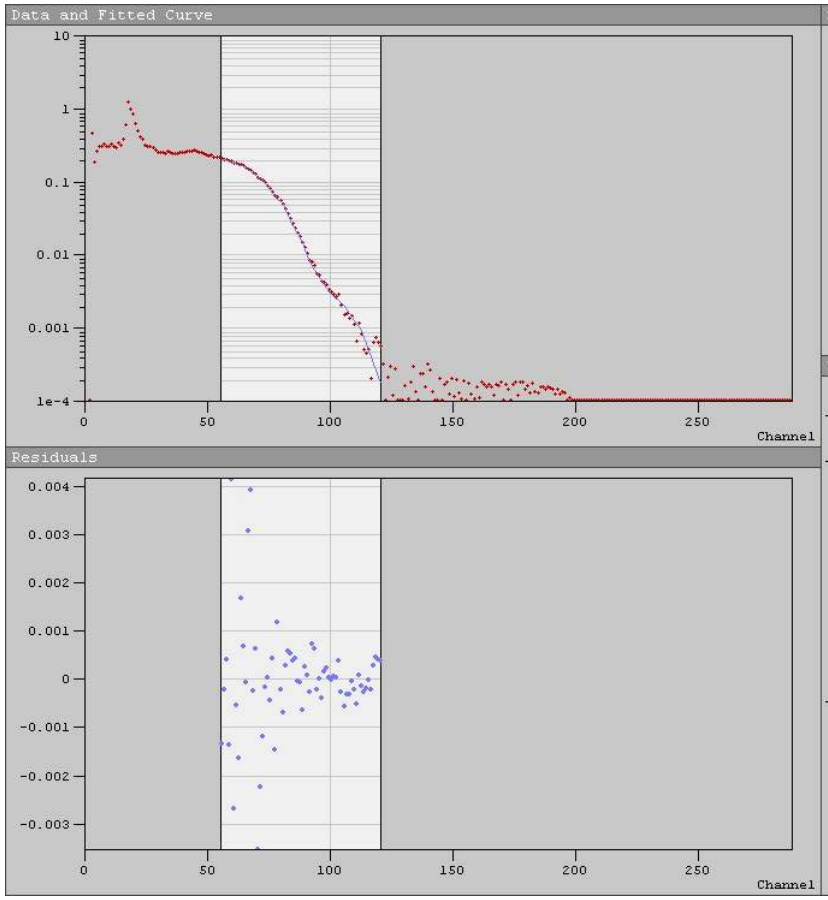

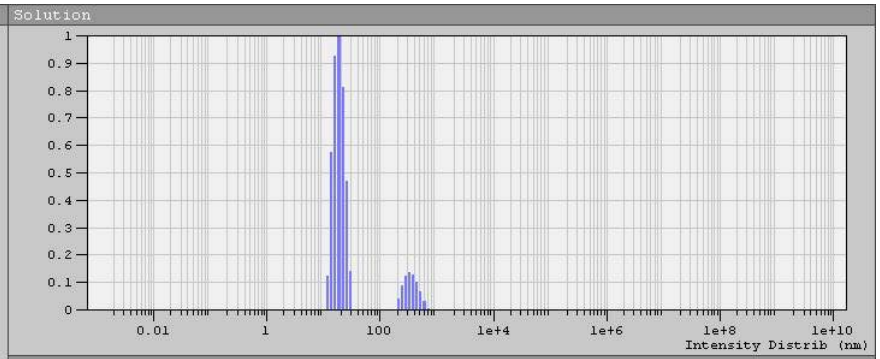

Peak Analysis

Files: m4_422.txt

m4_422.txt Intensity Distrib, (nm)

❖ Distribution analysis

Fitting range : [55, 120] channels
Number of Intervals : 200
Boundaries : [9.2e-4; 1.3e+10]
Resolution : 0

Peak Num	Area	Mean	Position	STD
1	0.852	18.67	18.43	4.172
2	0.148	354.9	326.3	100.3

χ^2 : 5.5e-4

Data and Fitted Curve

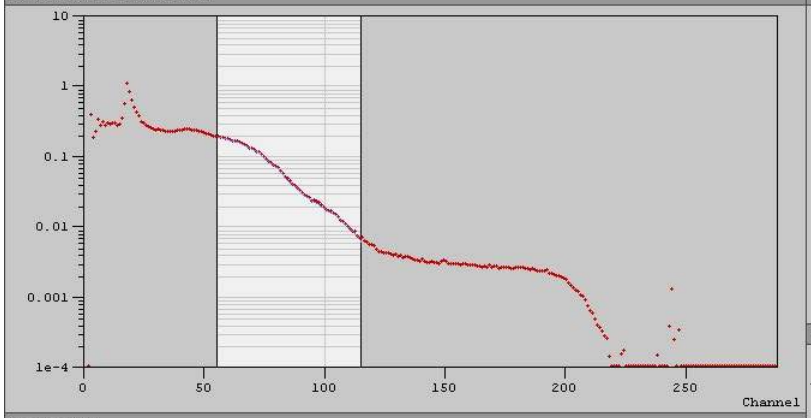

Residuals

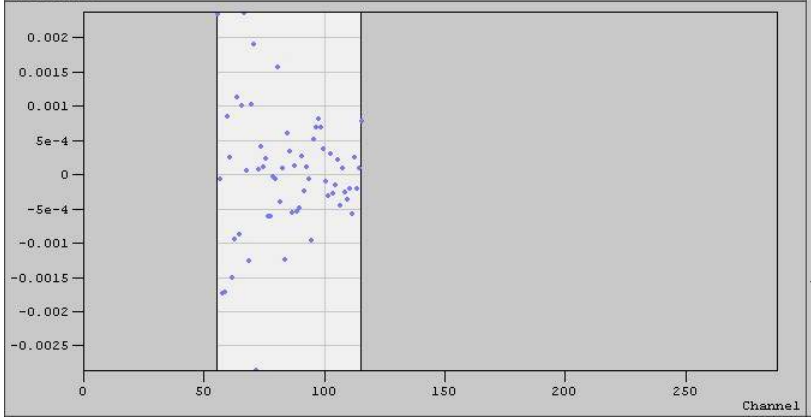

Solution

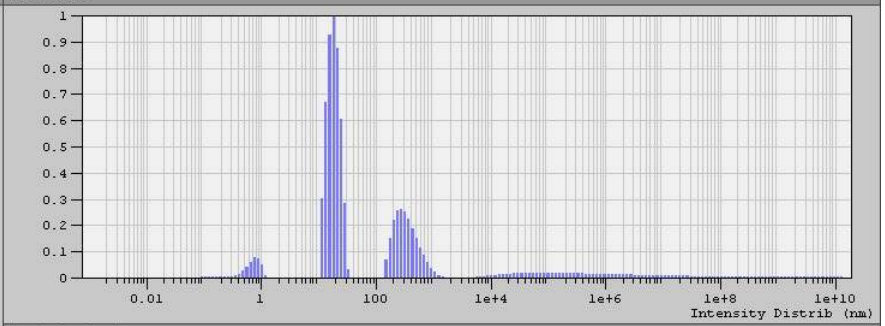

Peak Analysis

Files: m4_49.txt

m4_49.txt Intensity Distrib, (nm)

❖ Distribution analysis

Fitting range : [55; 115] channels
Number of Intervals : 200
Boundaries : [0.001; 1.4e+10]
Resolution : 0

Peak Num	Area	Mean	Position	STD
1	0.043	0.709	0.742	0.212
2	0.621	17.70	17.78	5.583
3	0.273	347.1	270.6	188.8
4	0.063	3.6e+5	7.3e+4	4.8e+5

χ^2 : 4.2e-4

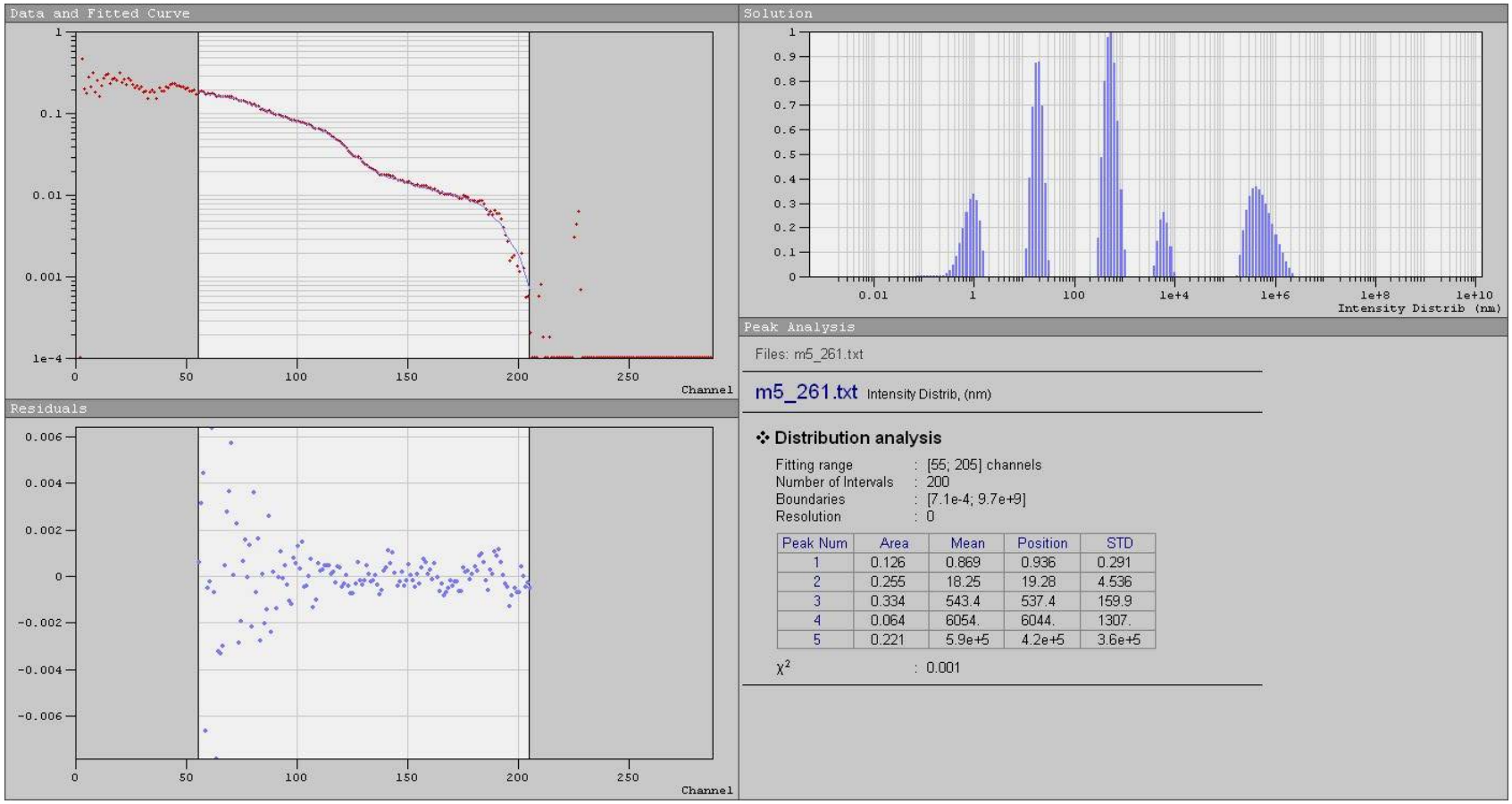
Data and Fitted Curve
Channel
Residuals
Channel
Solution
Intensity Distrib (nm)
Peak Analysis
Files: m5_261.txt
m5_261.txt Intensity Distrib, (nm)
Distribution analysis
Fitting range : [55; 205] channels
Number of Intervals : 200
Boundaries : [7.1e-4; 9.7e+9]
Resolution : 0
Peak Num | Area | Mean | Position | STD
1 | 0.126 | 0.869 | 0.936 | 0.291
2 | 0.255 | 18.25 | 19.28 | 4.536
3 | 0.334 | 543.4 | 537.4 | 159.9
4 | 0.064 | 6054. | 6044. | 1307.
5 | 0.221 | 5.9e+5 | 4.2e+5 | 3.6e+5
χ² : 0.001

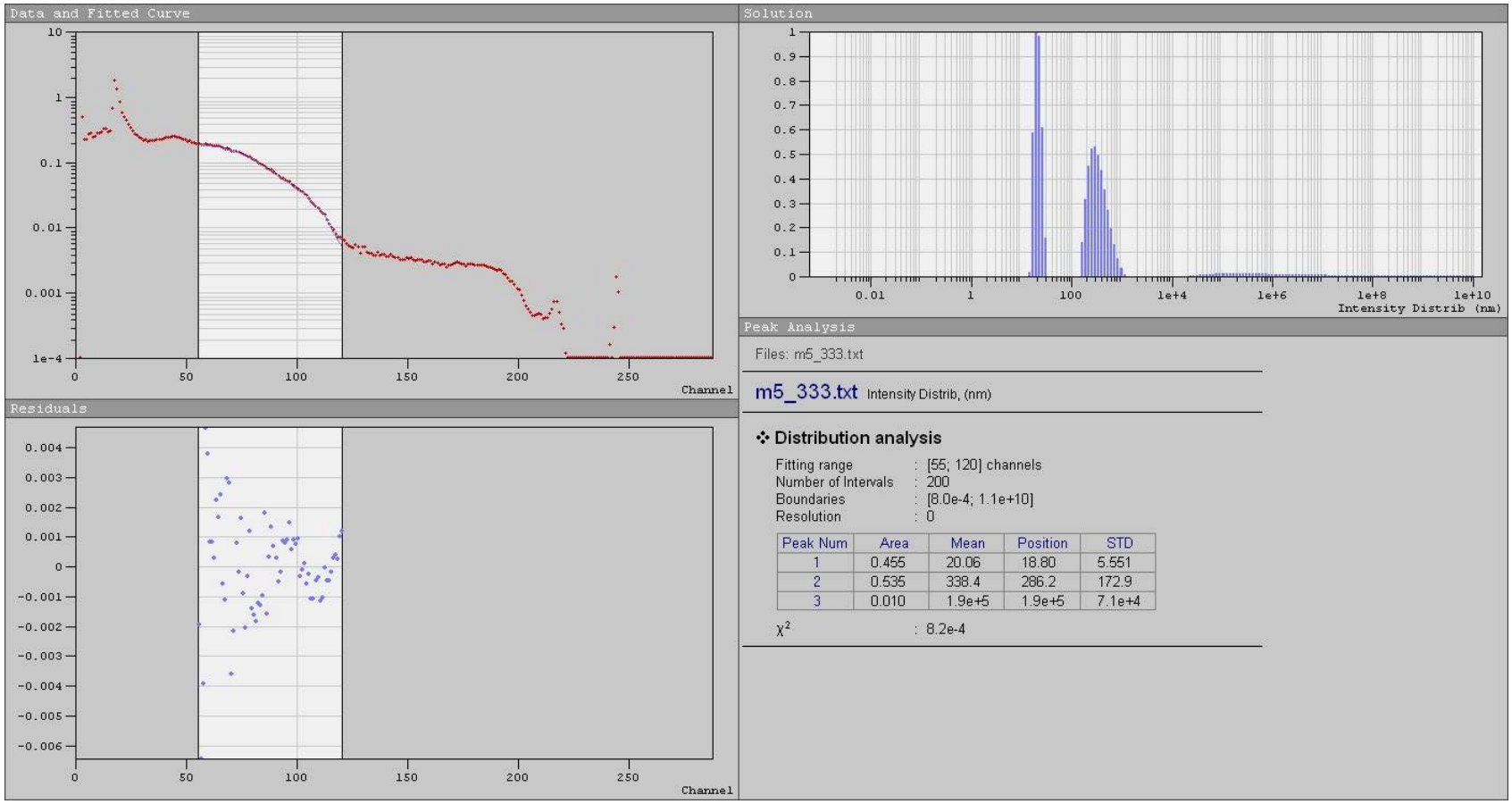
Data and Fitted Curve
Channel
Residuals
Channel
Solution
Intensity Distrib (nm)
Peak Analysis
Files: m5_333.txt
m5_333.txt Intensity Distrib, (nm)
Distribution analysis
Fitting range : [55; 120] channels
Number of Intervals : 200
Boundaries : [8.0e-4; 1.1e+10]
Resolution : 0
Peak Num | Area | Mean | Position | STD
1 | 0.455 | 20.06 | 18.80 | 5.551
2 | 0.535 | 338.4 | 286.2 | 172.9
3 | 0.010 | 1.9e+5 | 1.9e+5 | 7.1e+4
χ² : 8.2e-4

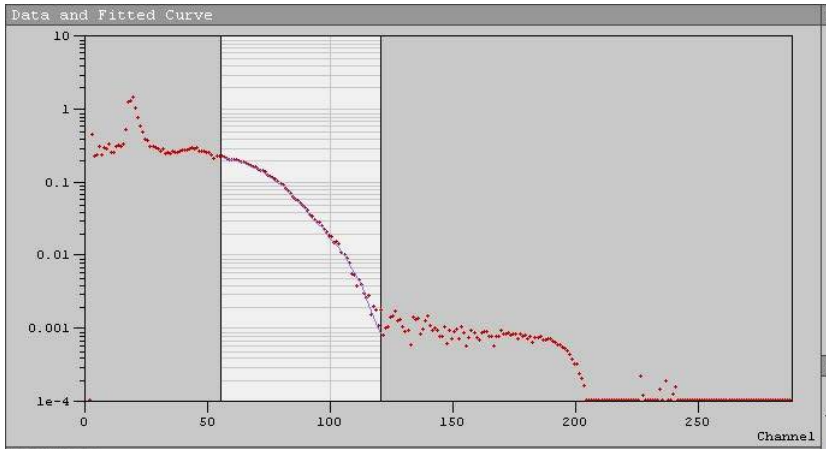

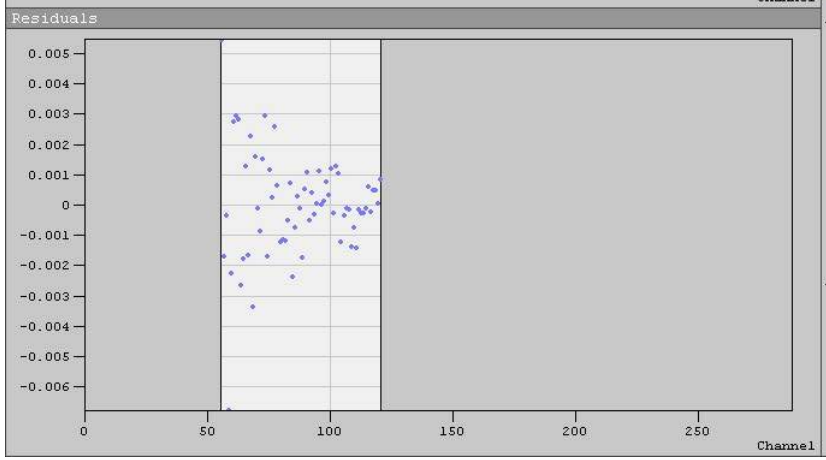

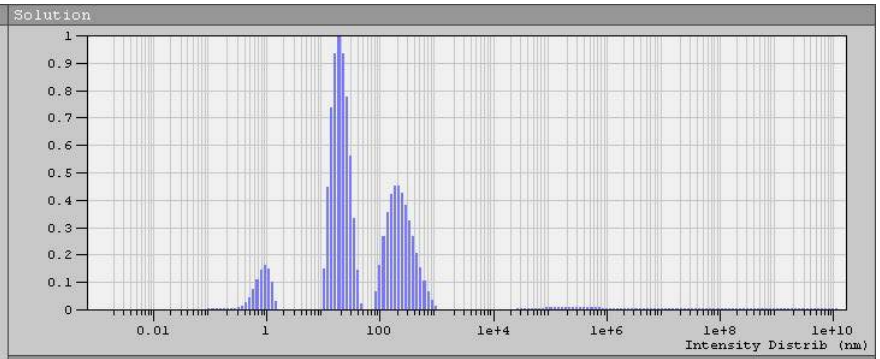

Peak Analysis

Files: m5_423.txt

m5_423.txt Intensity Distrib, (nm)

❖ Distribution analysis

Fitting range : [55, 120] channels
Number of Intervals : 200
Boundaries : [9.2e-4; 1.3e+10]
Resolution : 0

Peak Num	Area	Mean	Position	STD
1	0.076	0.841	0.895	0.273
2	0.550	20.09	18.43	7.446
3	0.374	250.6	207.3	144.3

χ^2 : 8.2e-4

Data and Fitted Curve

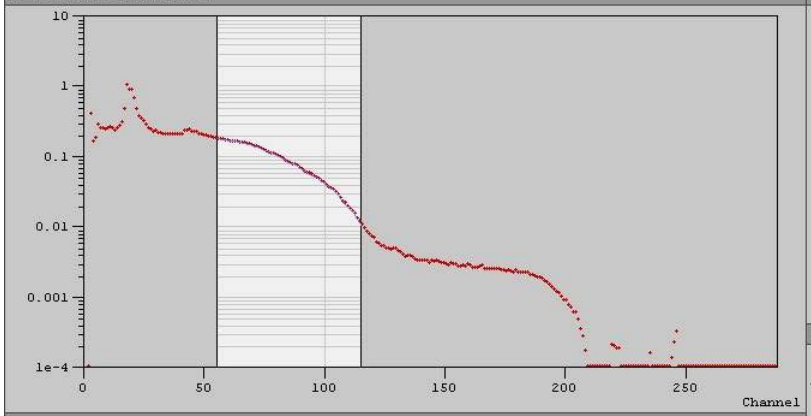

Residuals

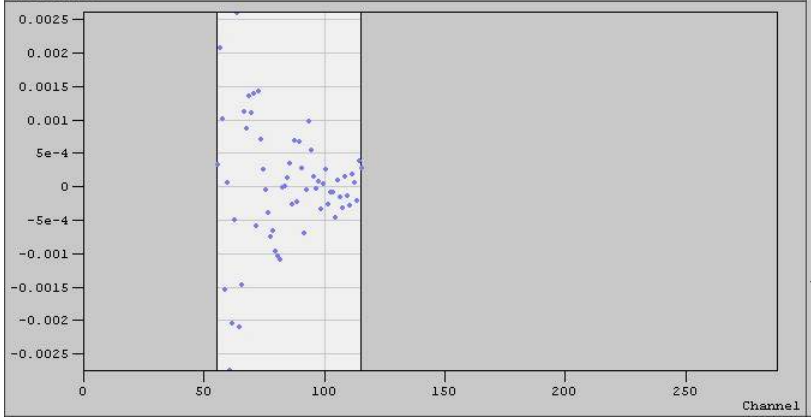

Solution

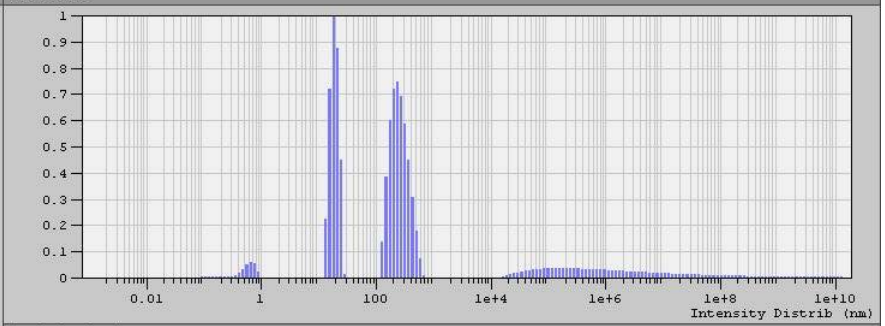

Peak Analysis

Files: m5_491.txt

m5_491.txt Intensity Distrib, (nm)

❖ Distribution analysis

Fitting range : [55; 115] channels
Number of Intervals : 200
Boundaries : [0.001; 1.4e+10]
Resolution : 0

Peak Num	Area	Mean	Position	STD
1	0.024	0.613	0.638	0.156
2	0.343	18.25	17.78	4.124
3	0.509	260.2	232.6	104.7
4	0.123	3.0e+6	1.6e+5	6.3e+6

χ^2 : 4.2e-4

									Unimer		Micelle 1		Micelle 2	
Sample	Run Name	Copolymer Concentration	T	n	η	Intensity	Min Channel	Max Channel	peak	mean	peak	mean	peak	mean
-	-	wt%	C	-	cP	cps	-	-	nm	nm	nm	nm	nm	nm
cC1	cC125 4	0.2	25	1.4218	0.98	270,847	55	125	-	-	-	-	111.6	116.9
cC1	cC1_26.5	0.2	26.5	1.4209	0.95	293,272	55	130	-	-	-	-	121.1	120.8
cC1	cC126	0.2	26.5	1.4209	0.95	382,750	55	130	-	-	-	-	121.1	130.7
cC1	cC126 b4 son	0.2	26.5	1.4209	0.95	427,265	55	130	-	-	-	-	104.1	116
cC1	cc1_27	0.2	27	1.4208	0.935	191,692	55	115	-	-	-	-	105.9	104.3
cC1	cC1_33	0.2	33.5	1.4172	0.79	239,760	55	115	-	-	-	-	94.17	95.24
cC1	cc1_42	0.2	42	1.4126	0.69	3,905	55	175	-	-	15.41	17.21	234.5	264.9
cC1	cc1_421	0.2	42	1.4126	0.69	4,450	55	165	-	-	13.25	18.08	234.5	246.9
cC1	cc1_491	0.20	49	1.4088	0.62	4,165	60	150	-	-	14.99	17.24	196.1	235.4
cC12	cc12_254	0.10	25.5	1.4218	0.98	181,114	55	120	-	-	-	-	86.56	89.18
cC12	cc12_33	0.10	33.5	1.4172	0.79	110,438	55	115	-	-	-	-	94.17	92.15
cC12	cc12_423	0.10	42	1.4126	0.69	4,450	55	165	-	-	15.41	18.71	234.5	275.2
cC12	cc12_49	0.100	49.5	1.4085	0.618	3,047	60	150	-	-	11.12	11.4	229.1	468.7
cC11	cc11_254	0.050	25.5	1.4218	0.98	93,067	55	125	-	-	-	-	100.7	99.5
cC11	cc11_331	0.050	33.5	1.4172	0.79	55,136	55	115	-	-	-	-	94.17	88.9
cC11	cc11_421	0.050	42	1.4126	0.69	4,450	55	165	0.87	0.754	17.93	19.19	201.6	216.9
cC11	cc11_49	0.05	49.5	1.4085	0.618	3,719	60	150	-	-	9.562	10.08	197	229

Table C.2: DLS results for pure cyclohexane.

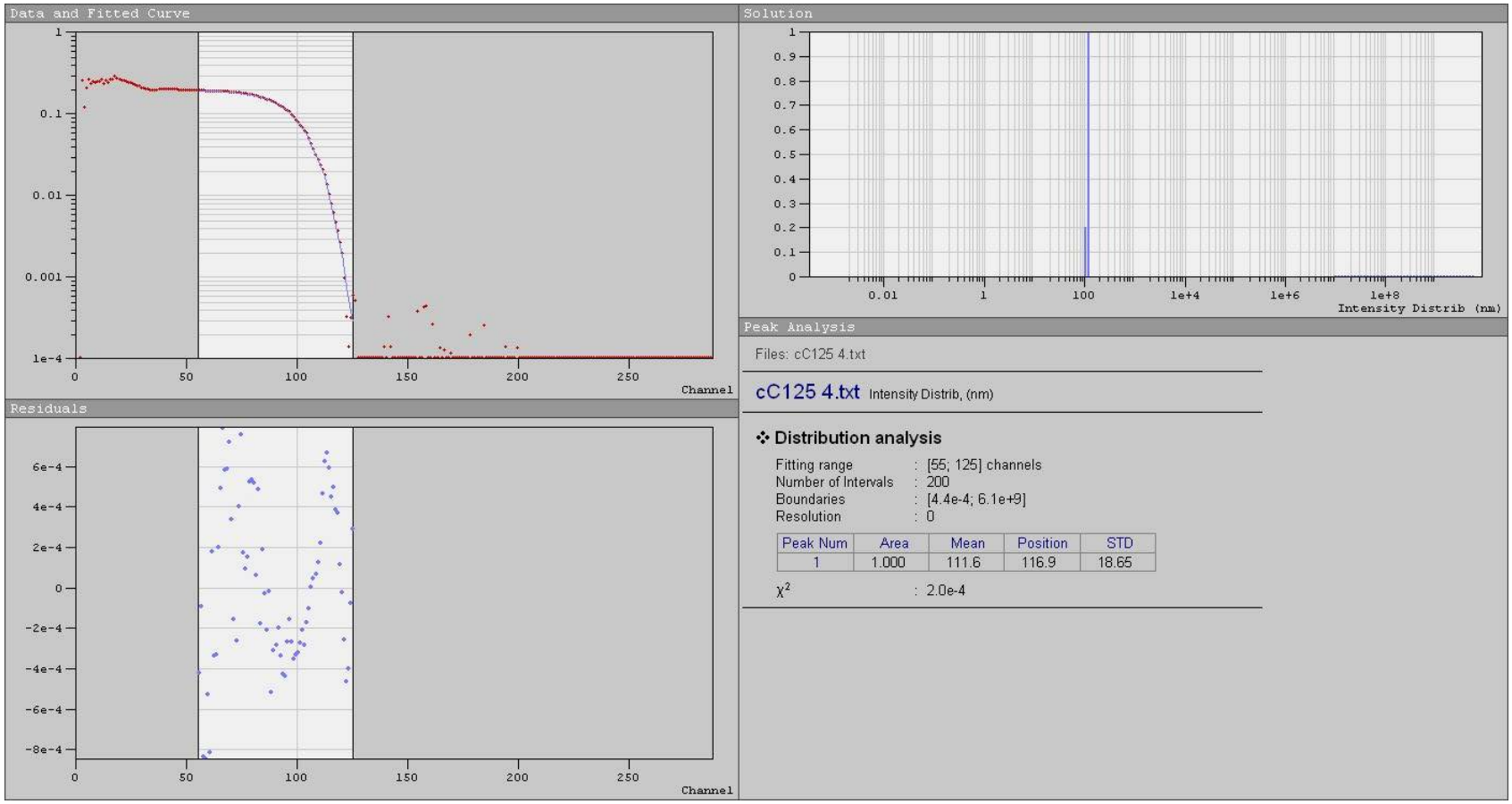
Data and Fitted Curve
1
0.1
0.01
0.001
1e-4
0
50
100
150
200
250
Channel
Residuals
6e-4
4e-4
2e-4
0
-2e-4
-4e-4
-6e-4
-8e-4
0
50
100
150
200
250
Channel
Solution
1
0.9
0.8
0.7
0.6
0.5
0.4
0.3
0.2
0.1
0
0.01
1
100
1e+4
1e+6
1e+8
Intensity Distrib (nm)
Peak Analysis
Files: cC125 4.txt
cC125 4.txt Intensity Distrib, (nm)
Distribution analysis
Fitting range : [55; 125] channels
Number of Intervals : 200
Boundaries : [4.4e-4; 6.1e+9]
Resolution : 0
Peak Num | Area | Mean | Position | STD
1 | 1.000 | 111.6 | 116.9 | 18.65
χ² : 2.0e-4

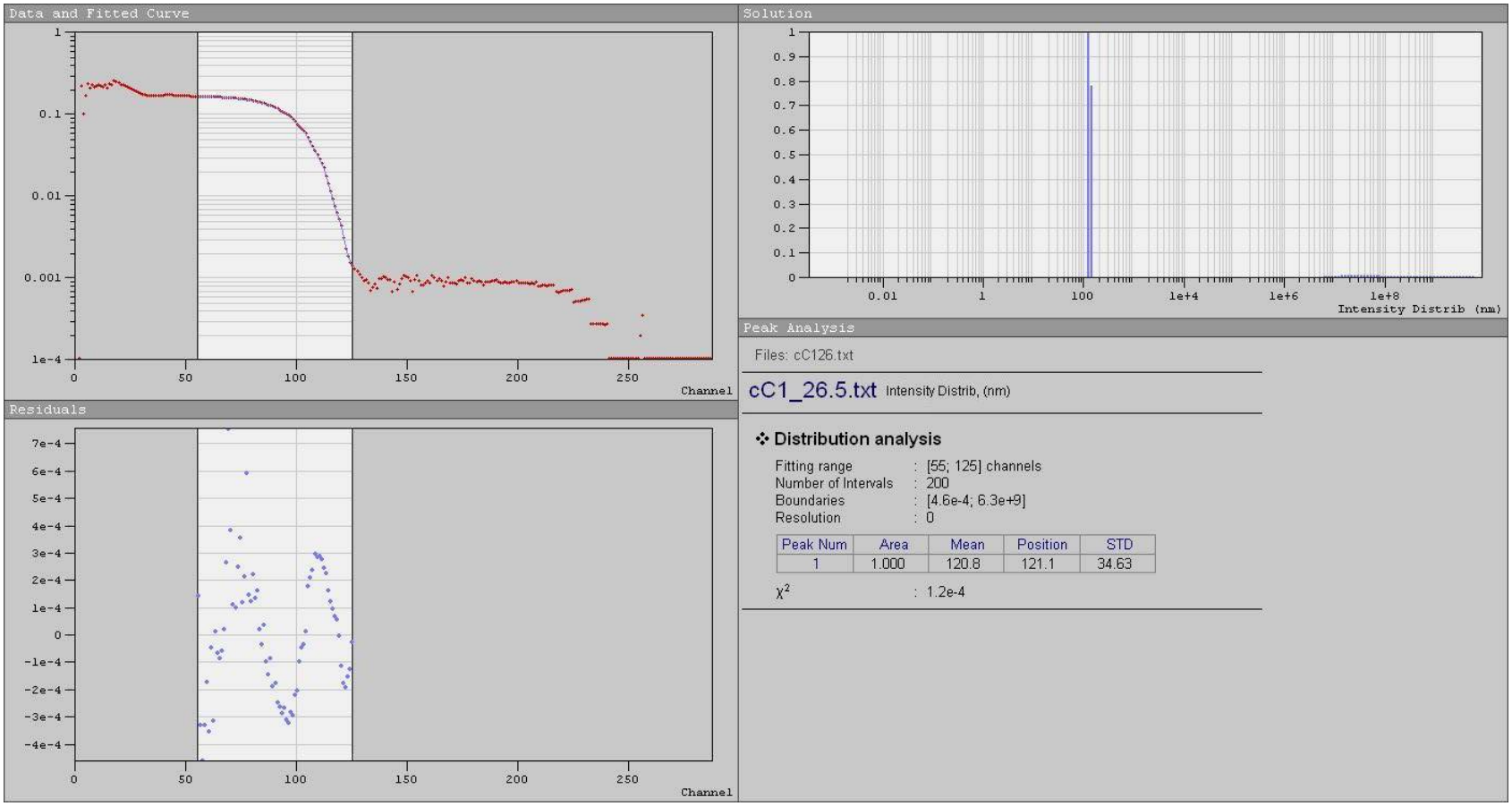
Data and Fitted Curve
Channel
Residuals
Channel
Solution
Intensity Distrib (nm)
Peak Analysis
Files: cC126.txt
cC1_26.5.txt Intensity Distrib, (nm)
Distribution analysis
Fitting range : [55; 125] channels
Number of Intervals : 200
Boundaries : [4.6e-4; 6.3e+9]
Resolution : 0
Peak Num | Area | Mean | Position | STD
1 | 1.000 | 120.8 | 121.1 | 34.63
χ² : 1.2e-4

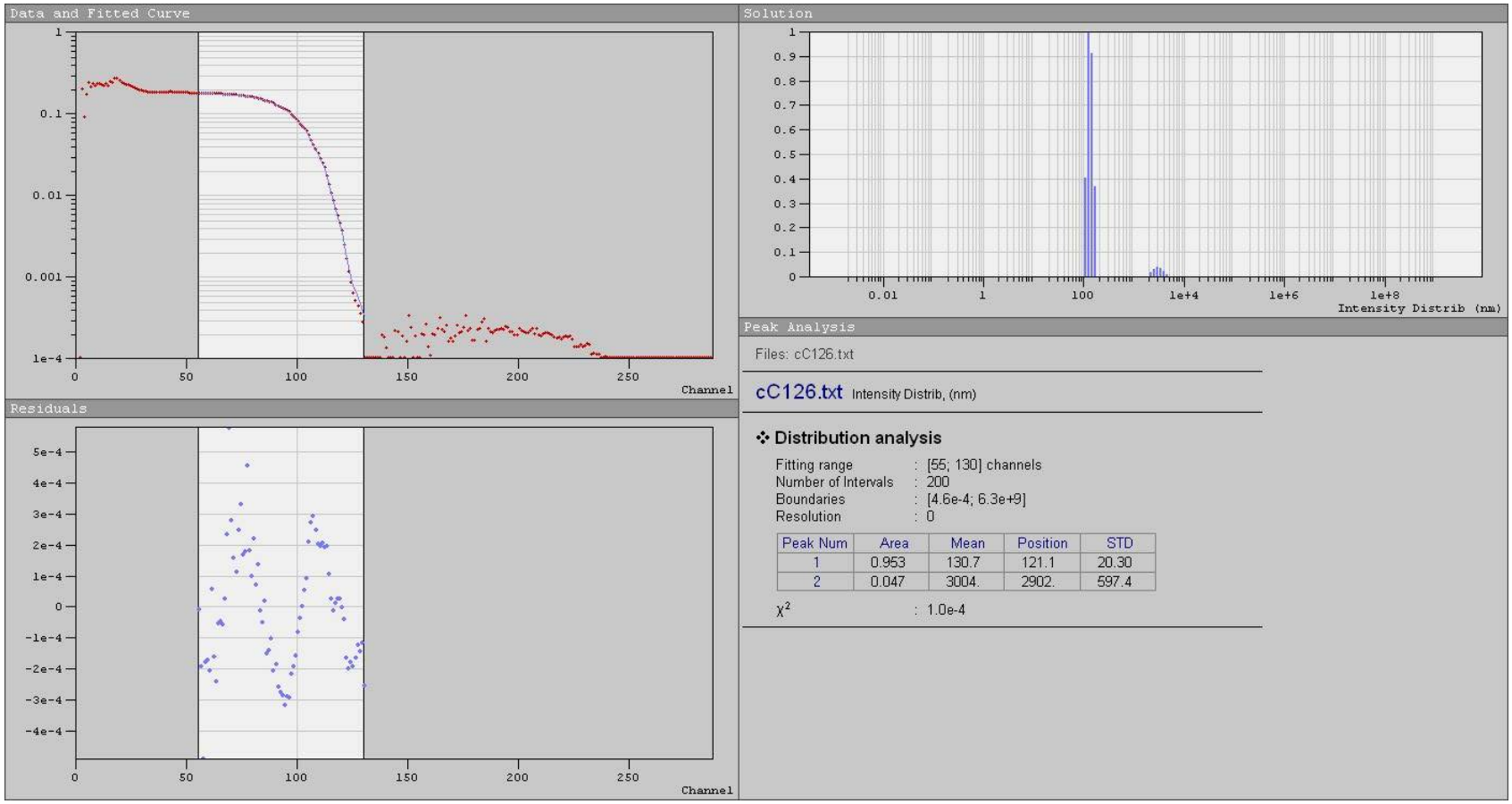
Data and Fitted Curve
1
0.1
0.01
0.001
1e-4
0
50
100
150
200
250
Channel
Residuals
5e-4
4e-4
3e-4
2e-4
1e-4
0
-1e-4
-2e-4
-3e-4
-4e-4
0
50
100
150
200
250
Channel
Solution
1
0.9
0.8
0.7
0.6
0.5
0.4
0.3
0.2
0.1
0
0.01
1
100
1e+4
1e+6
1e+8
Intensity Distrib (nm)
Peak Analysis
Files: cC126.txt
cC126.txt Intensity Distrib, (nm)
Distribution analysis
Fitting range : [55; 130] channels
Number of Intervals : 200
Boundaries : [4.6e-4; 6.3e+9]
Resolution : 0
Peak Num | Area | Mean | Position | STD
1 | 0.953 | 130.7 | 121.1 | 20.30
2 | 0.047 | 3004. | 2902. | 597.4
χ² : 1.0e-4

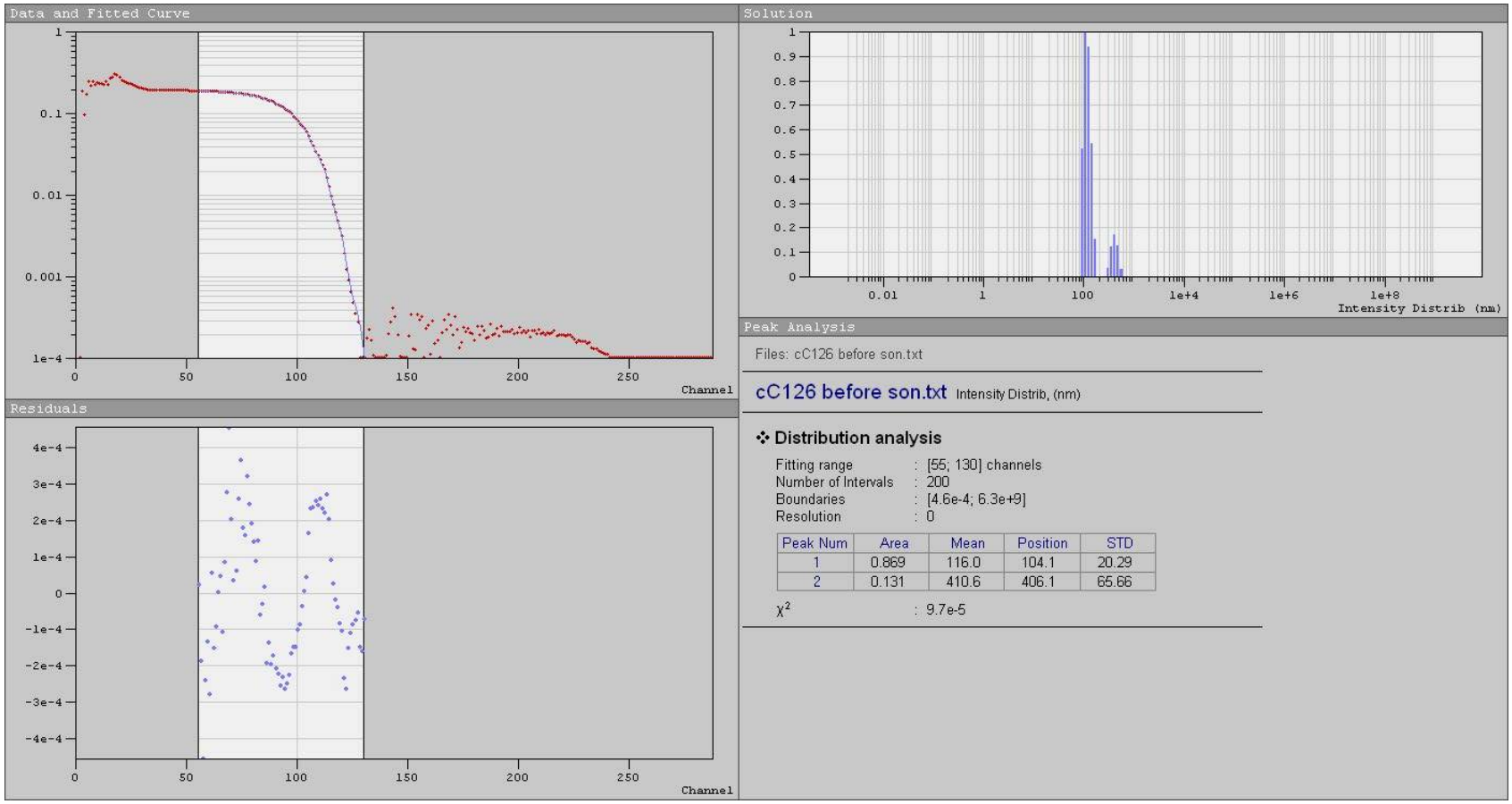
Data and Fitted Curve
Channel
Residuals
Channel
Solution
Intensity Distrib (nm)
Peak Analysis
Files: cC126 before son.txt
cC126 before son.txt Intensity Distrib, (nm)
Distribution analysis
Fitting range : [55; 130] channels
Number of Intervals : 200
Boundaries : [4.6e-4; 6.3e+9]
Resolution : 0
Peak Num | Area | Mean | Position | STD
1 | 0.869 | 116.0 | 104.1 | 20.29
2 | 0.131 | 410.6 | 406.1 | 65.66
χ² : 9.7e-5

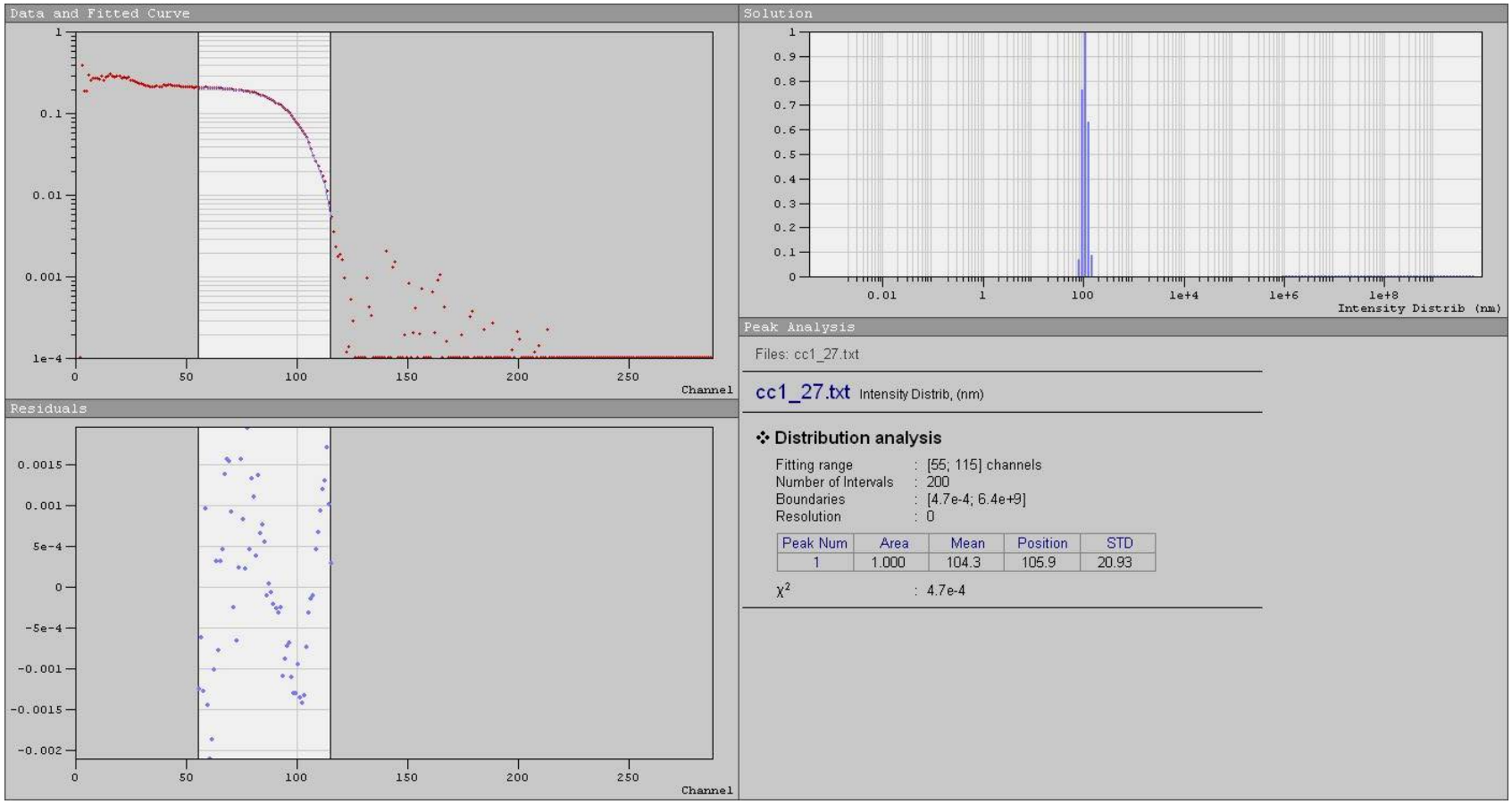
Data and Fitted Curve
1
0.1
0.01
0.001
1e-4
0
50
100
150
200
250
Channel
Residuals
0.0015
0.001
5e-4
0
-5e-4
-0.001
-0.0015
-0.002
0
50
100
150
200
250
Channel
Solution
1
0.9
0.8
0.7
0.6
0.5
0.4
0.3
0.2
0.1
0
0.01
1
100
1e+4
1e+6
1e+8
Intensity Distrib (nm)
Peak Analysis
Files: cc1_27.txt
cc1_27.txt Intensity Distrib, (nm)
Distribution analysis
Fitting range : [55; 115] channels
Number of Intervals : 200
Boundaries : [4.7e-4; 6.4e+9]
Resolution : 0
Peak Num
Area
Mean
Position
STD
1
1.000
104.3
105.9
20.93
χ2 : 4.7e-4

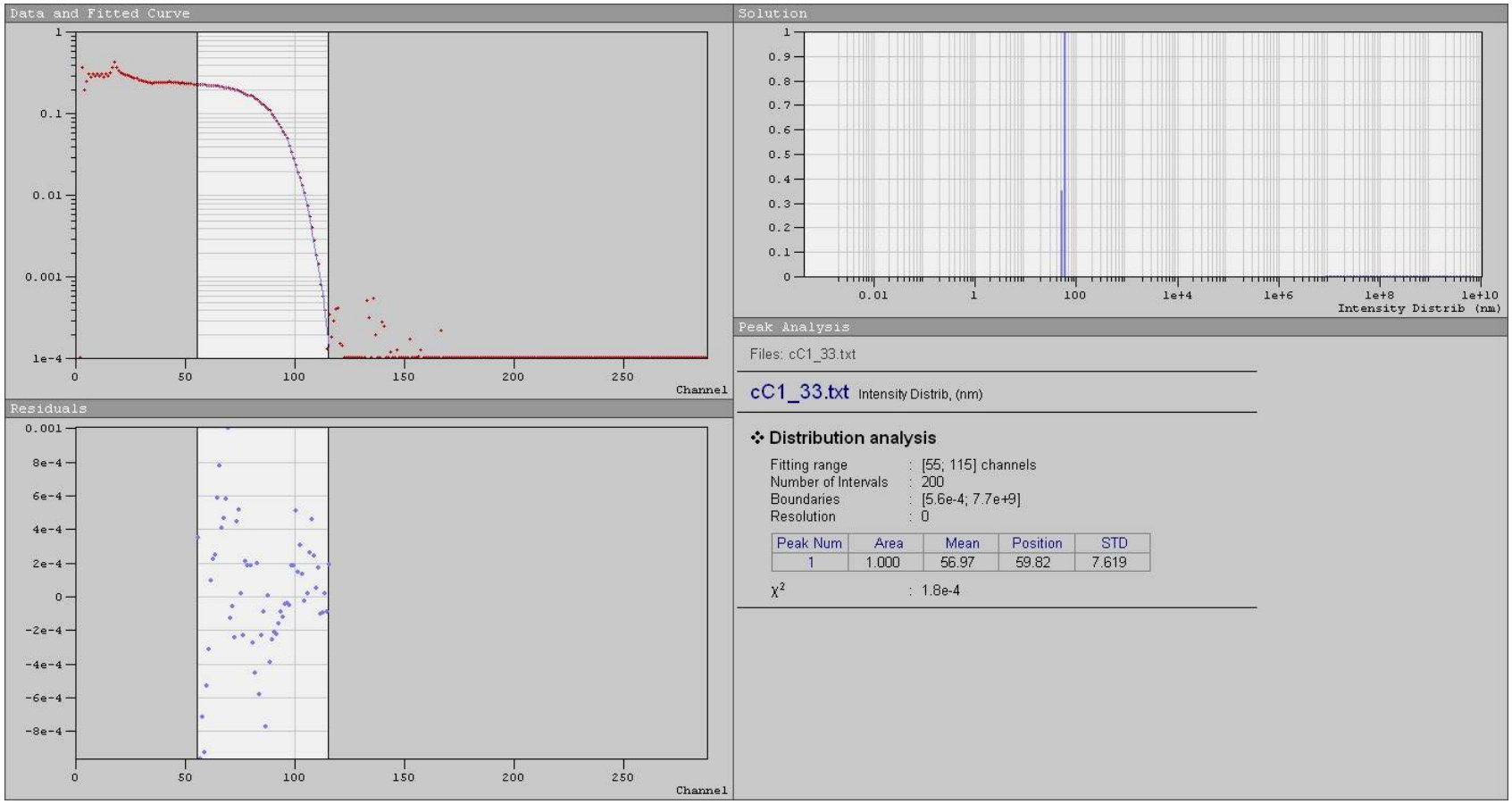
Data and Fitted Curve
Channel
Residuals
Channel
Solution
Intensity Distrib (nm)
Peak Analysis
Files: cC1_33.txt
cC1_33.txt Intensity Distrib, (nm)
Distribution analysis
Fitting range : [55, 115] channels
Number of Intervals : 200
Boundaries : [5.6e-4; 7.7e+9]
Resolution : 0
Peak Num | Area | Mean | Position | STD
1 | 1.000 | 56.97 | 59.82 | 7.619
χ² : 1.8e-4

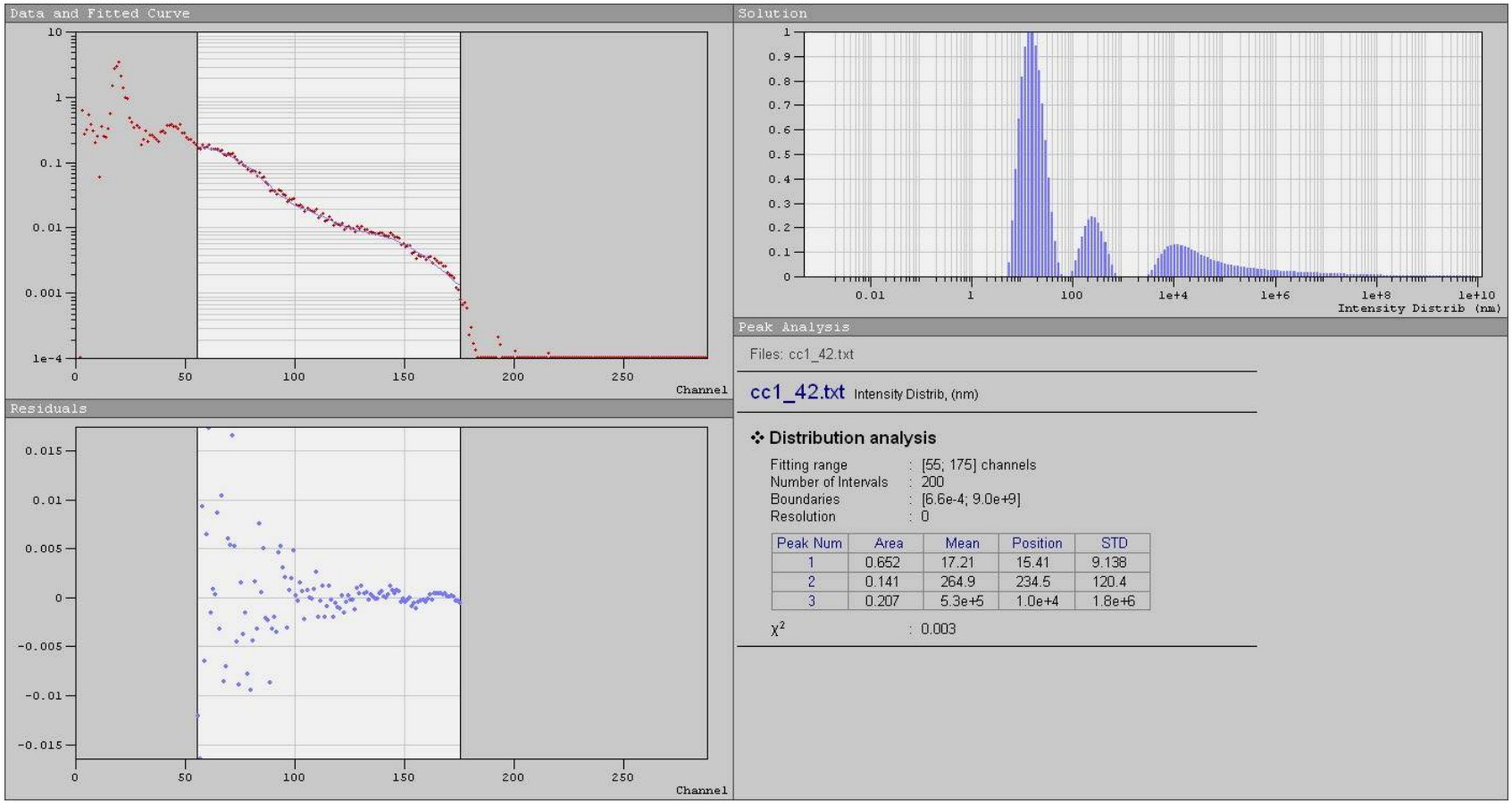
Data and Fitted Curve
Channel
Residuals
Channel
Solution
Intensity Distrib (nm)
Peak Analysis
Files: cc1_42.txt
cc1_42.txt Intensity Distrib, (nm)
Distribution analysis
Fitting range : [55, 175] channels
Number of Intervals : 200
Boundaries : [6.6e-4; 9.0e+9]
Resolution : 0
Peak Num | Area | Mean | Position | STD
1 | 0.652 | 17.21 | 15.41 | 9.138
2 | 0.141 | 264.9 | 234.5 | 120.4
3 | 0.207 | 5.3e+5 | 1.0e+4 | 1.8e+6
χ² : 0.003

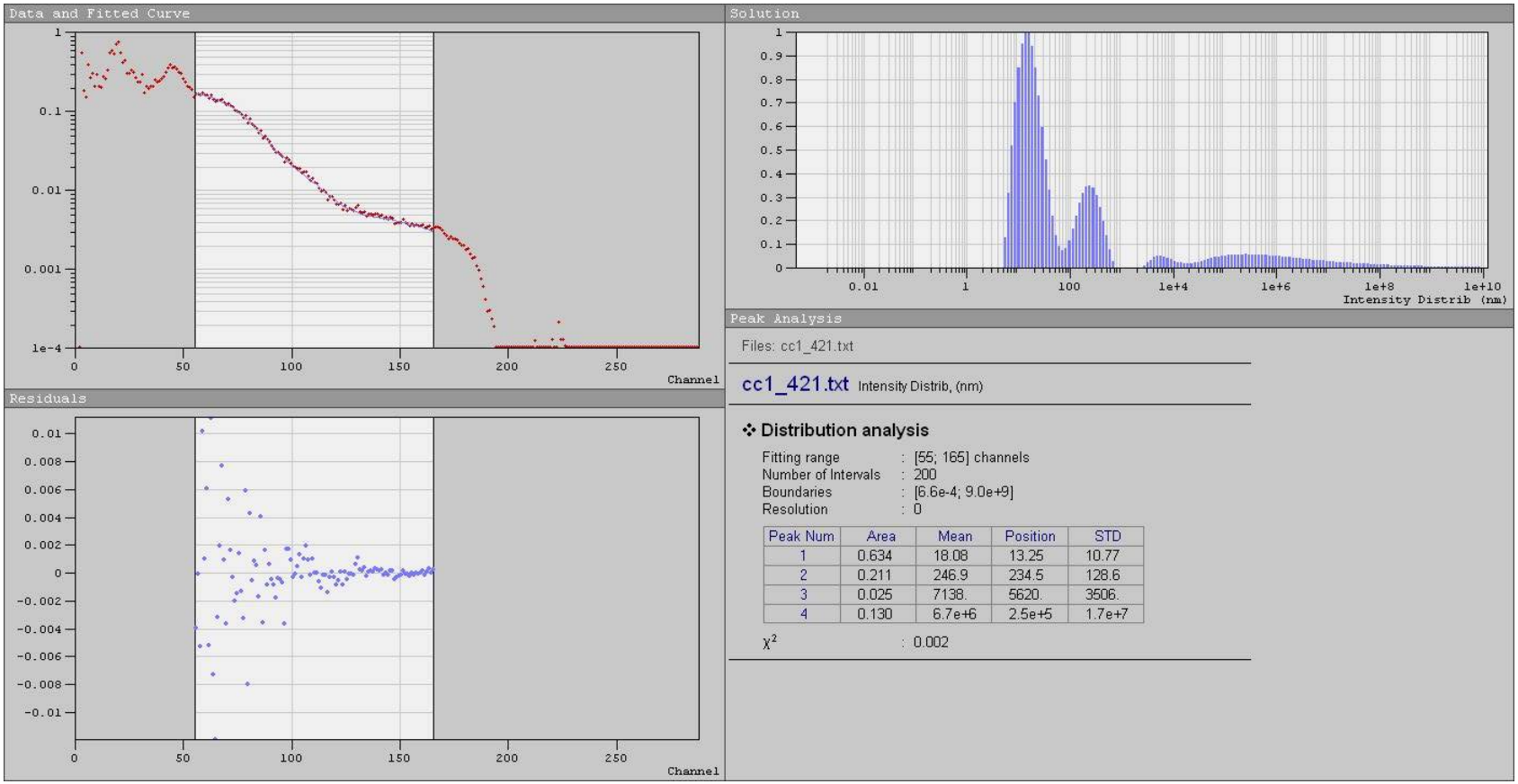
Data and Fitted Curve
Channel
Residuals
Channel
Solution
Intensity Distrib (nm)
Peak Analysis
Files: cc1_421.txt
cc1_421.txt Intensity Distrib, (nm)
❖ Distribution analysis
Fitting range : [55; 165] channels
Number of Intervals : 200
Boundaries : [6.6e-4; 9.0e+9]
Resolution : 0
Peak Num | Area | Mean | Position | STD
1 | 0.634 | 18.08 | 13.25 | 10.77
2 | 0.211 | 246.9 | 234.5 | 128.6
3 | 0.025 | 7138. | 5620. | 3506.
4 | 0.130 | 6.7e+6 | 2.5e+5 | 1.7e+7
χ² : 0.002

Data and Fitted Curve

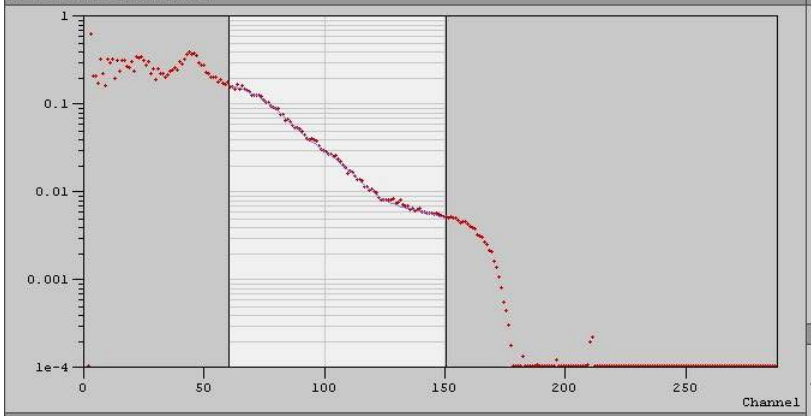

Residuals

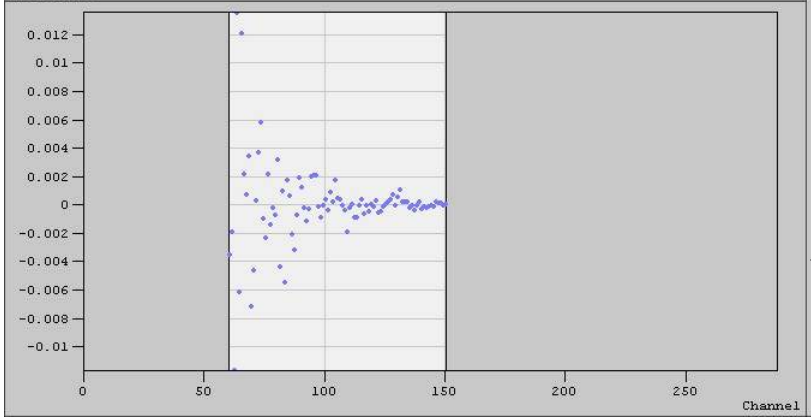

Solution

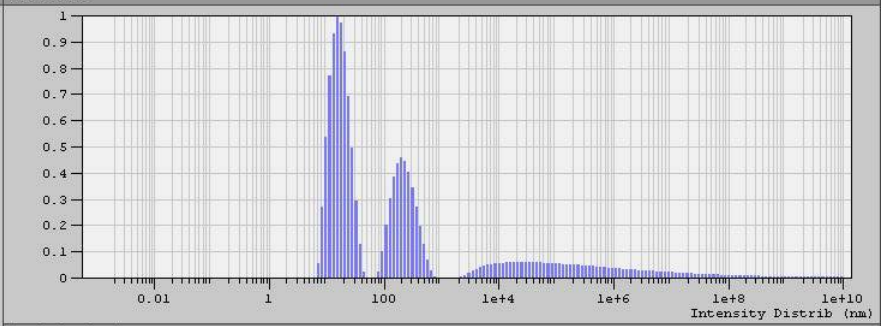

Peak Analysis

Files: cc1_491.txt

cc1_491.txt Intensity Distrib, (nm)

❖ **Distribution analysis**

Fitting range : [60; 150] channels
Number of Intervals : 200
Boundaries : [7.4e-4; 1.0e+10]
Resolution : 0

Peak Num	Area	Mean	Position	STD
1	0.531	17.24	14.99	7.049
2	0.286	235.4	196.1	115.4
3	0.183	2.4e+6	2.5e+4	7.3e+6

χ^2 : 0.002

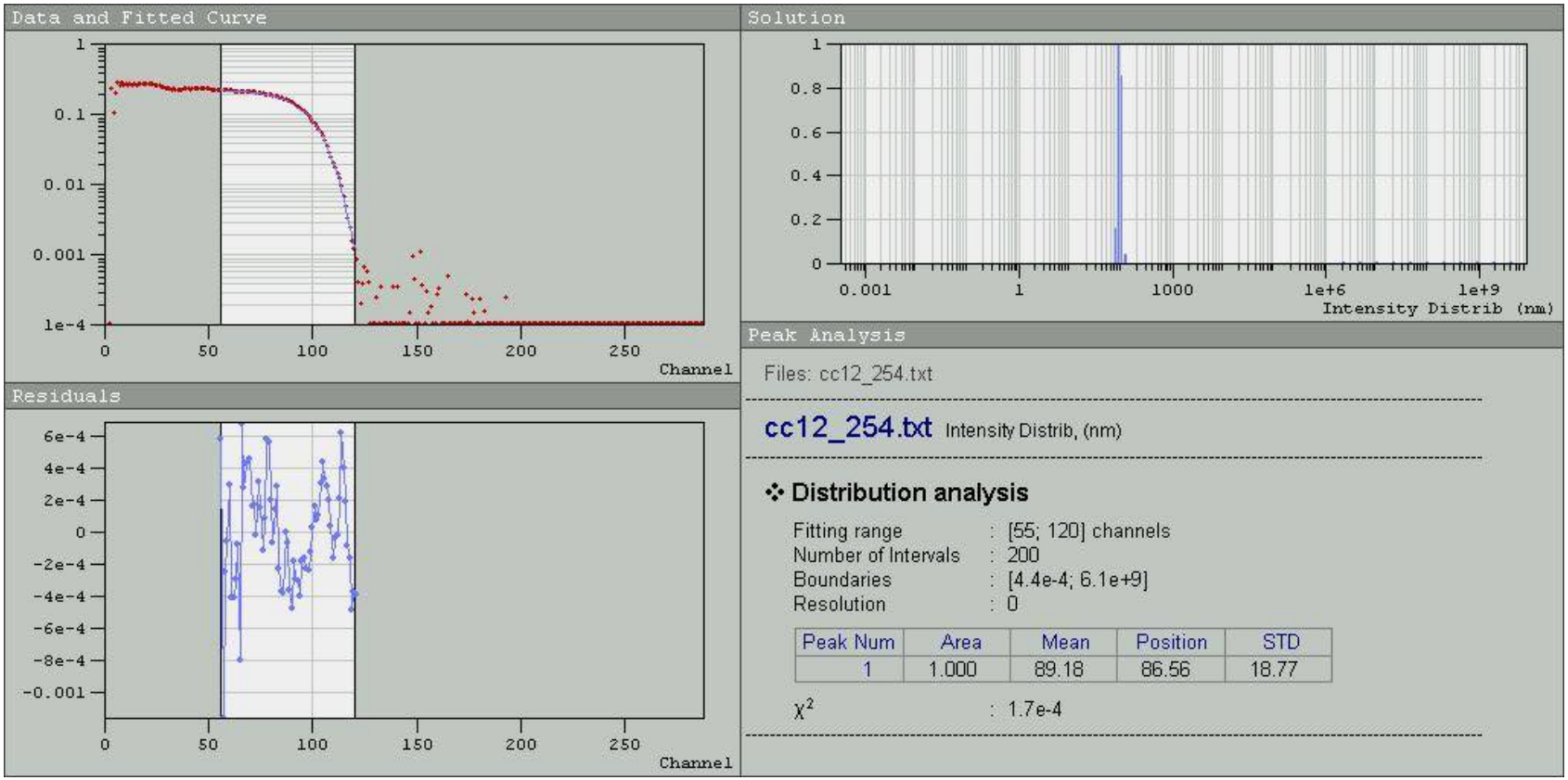
Data and Fitted Curve
1
0.1
0.01
0.001
1e-4
0
50
100
150
200
250
Channel
Residuals
6e-4
4e-4
2e-4
0
-2e-4
-4e-4
-6e-4
-8e-4
-0.001
0
50
100
150
200
250
Channel
Solution
1
0.8
0.6
0.4
0.2
0
0.001
1
1000
1e+6
1e+9
Intensity Distrib (nm)
Peak Analysis
Files: cc12_254.txt
cc12_254.txt Intensity Distrib, (nm)
Distribution analysis
Fitting range : [55; 120] channels
Number of Intervals : 200
Boundaries : [4.4e-4; 6.1e+9]
Resolution : 0
Peak Num | Area | Mean | Position | STD
1 | 1.000 | 89.18 | 86.56 | 18.77
χ² : 1.7e-4

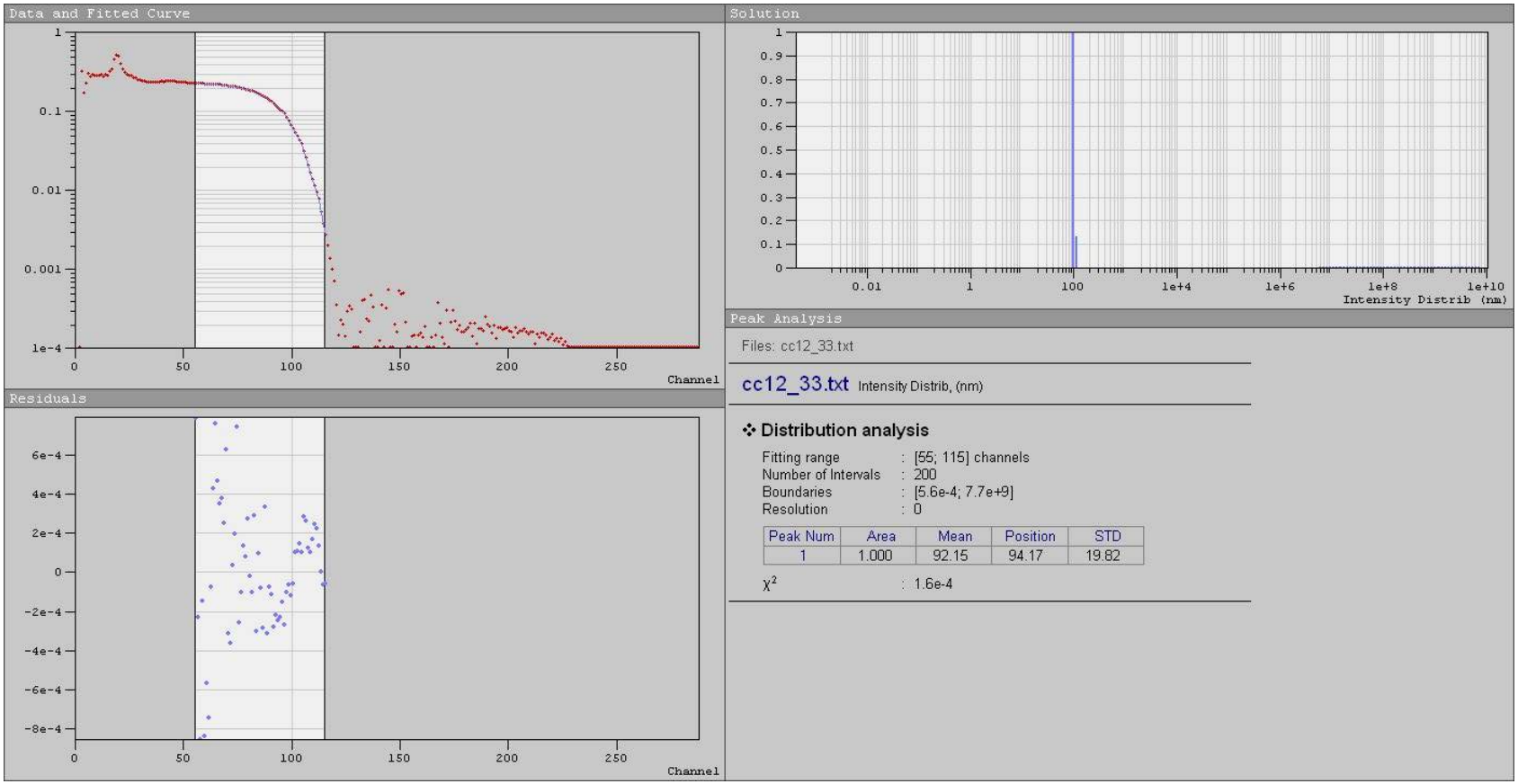
Data and Fitted Curve
1
0.1
0.01
0.001
1e-4
0
50
100
150
200
250
Channel
Residuals
6e-4
4e-4
2e-4
0
-2e-4
-4e-4
-6e-4
-8e-4
0
50
100
150
200
250
Channel
Solution
1
0.9
0.8
0.7
0.6
0.5
0.4
0.3
0.2
0.1
0
0.01
1
100
1e+4
1e+6
1e+8
1e+10
Intensity Distrib (nm)
Peak Analysis
Files: cc12_33.txt
cc12_33.txt Intensity Distrib, (nm)
❖ Distribution analysis
Fitting range : [55; 115] channels
Number of Intervals : 200
Boundaries : [5.6e-4; 7.7e+9]
Resolution : 0
Peak Num | Area | Mean | Position | STD
1 | 1.000 | 92.15 | 94.17 | 19.82
χ² : 1.6e-4

Data and Fitted Curve

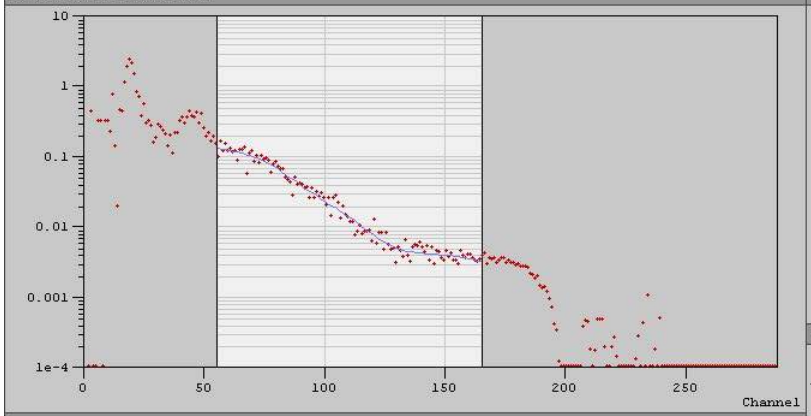

Residuals

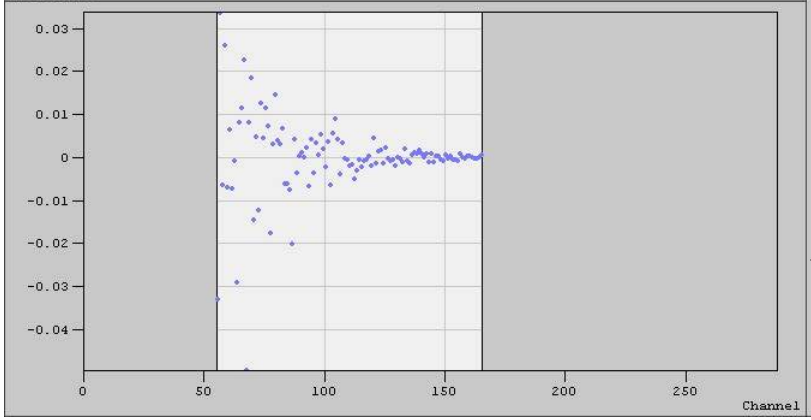

Solution

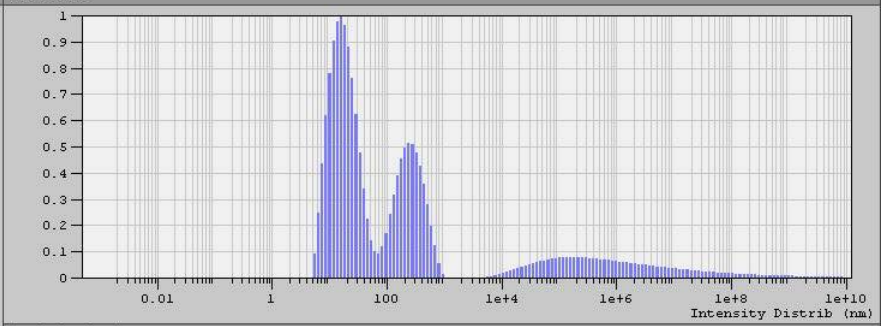

Peak Analysis

Files: cc12_423.txt

cc12_423.txt Intensity Distrib, (nm)

❖ **Distribution analysis**

Fitting range : [55; 165] channels
Number of Intervals : 200
Boundaries : [6.6e-4; 9.0e+9]
Resolution : 0.250

Peak Num	Area	Mean	Position	STD
1	0.539	18.71	15.41	10.87
2	0.294	275.2	234.5	156.9
3	0.167	8.5e+6	1.6e+5	2.7e+7

χ^2 : 0.006

Data and Fitted Curve

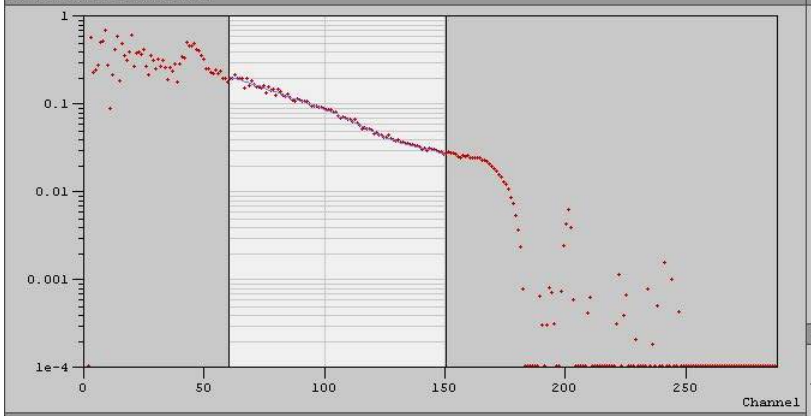

Residuals

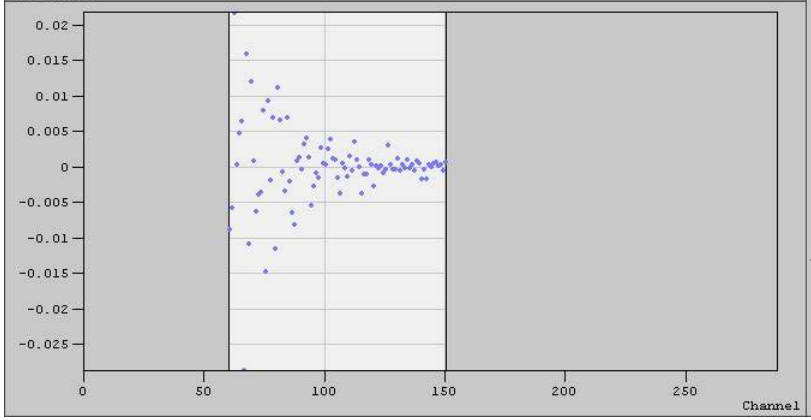

Solution

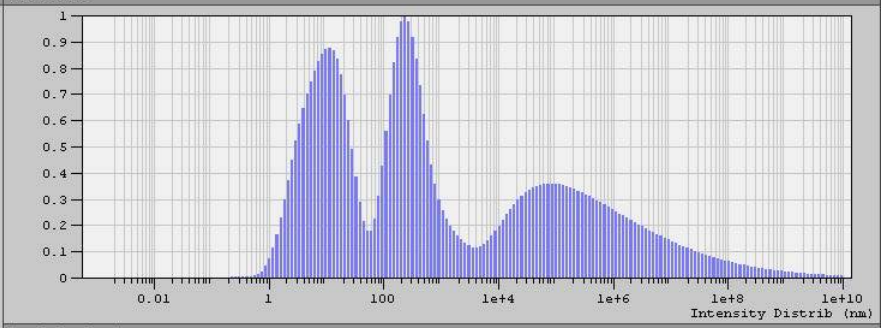

Peak Analysis

Files: cc12_49.txt

cc12_49.txt Intensity Distrib, (nm)

❖ **Distribution analysis**

Fitting range : [60; 150] channels
Number of Intervals : 200
Boundaries : [7.5e-4; 1.0e+10]
Resolution : 0

Peak Num	Area	Mean	Position	STD
1	0.330	11.40	11.12	9.474
2	0.311	468.7	229.1	585.2
3	0.359	3.5e+7	8.4e+4	2.2e+8

χ^2 : 0.003

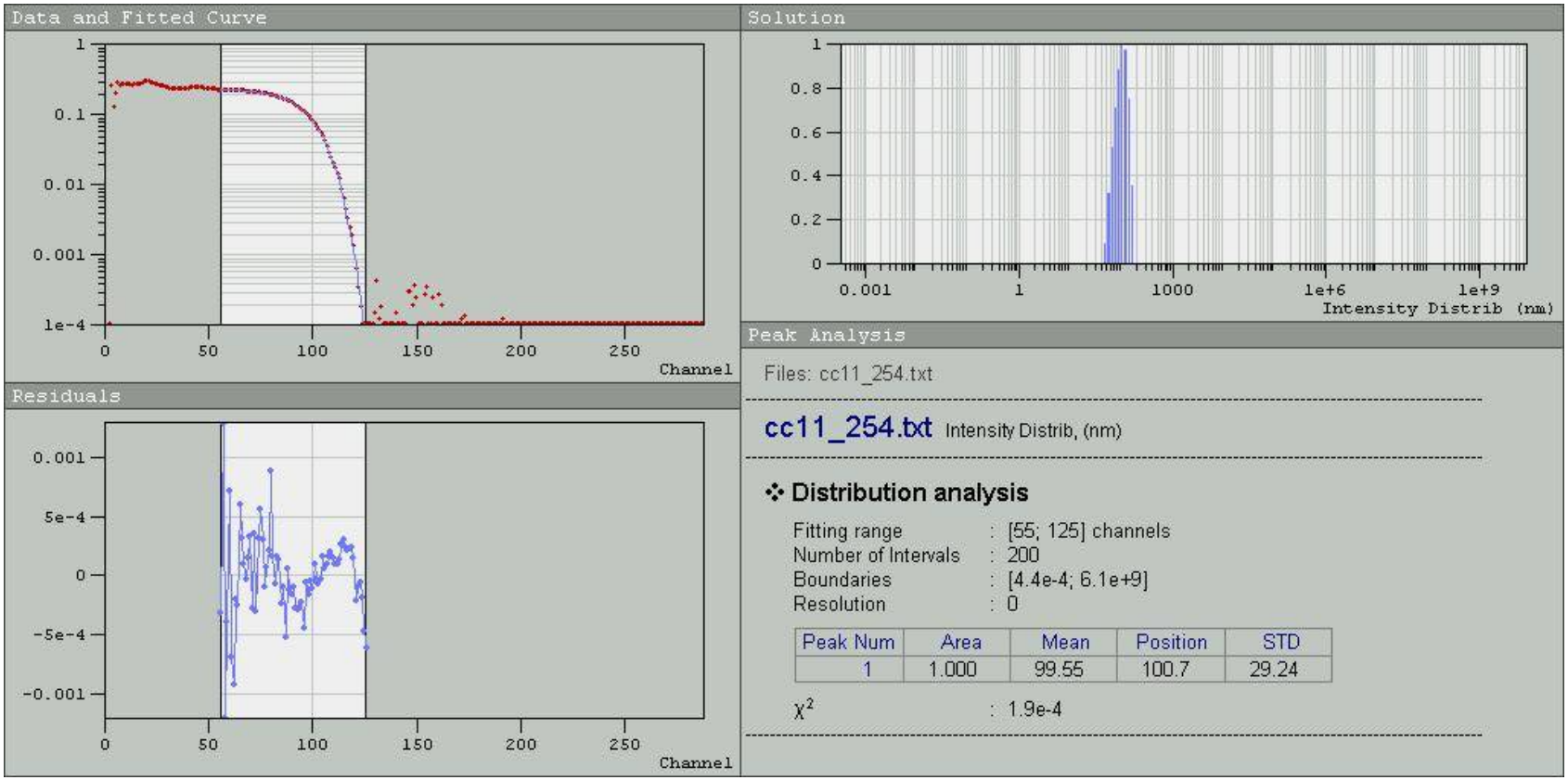
Data and Fitted Curve
1
0.1
0.01
0.001
1e-4
0
50
100
150
200
250
Channel
Residuals
0.001
5e-4
0
-5e-4
-0.001
0
50
100
150
200
250
Channel
Solution
1
0.8
0.6
0.4
0.2
0
0.001
1
1000
1e+6
1e+9
Intensity Distrib (nm)
Peak Analysis
Files: cc11_254.txt
cc11_254.txt Intensity Distrib, (nm)
Distribution analysis
Fitting range : [55; 125] channels
Number of Intervals : 200
Boundaries : [4.4e-4; 6.1e+9]
Resolution : 0
Peak Num | Area | Mean | Position | STD
1 | 1.000 | 99.55 | 100.7 | 29.24
χ² : 1.9e-4

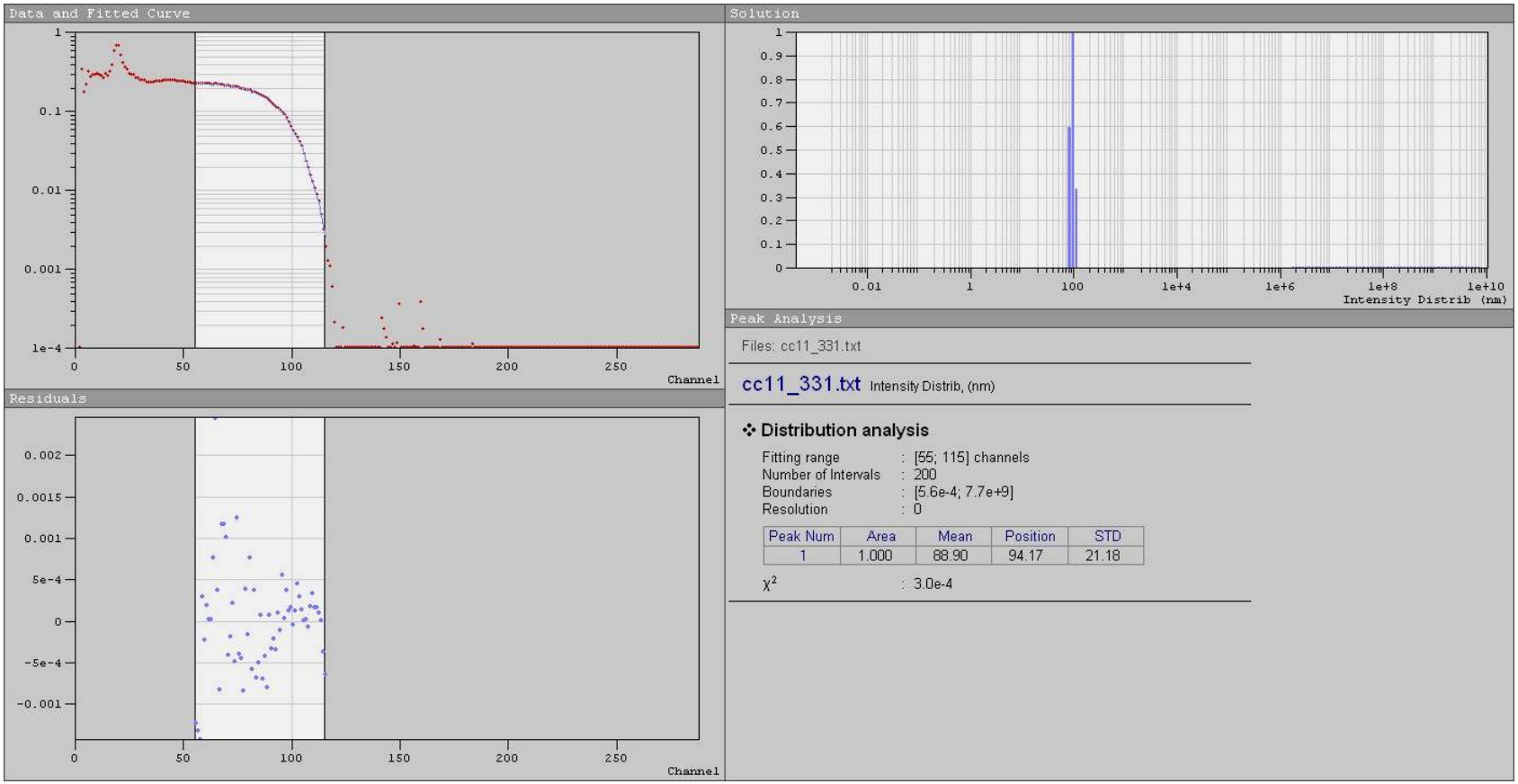
Data and Fitted Curve
1
0.1
0.01
0.001
1e-4
0
50
100
150
200
250
Channel
Residuals
0.002
0.0015
0.001
5e-4
0
-5e-4
-0.001
0
50
100
150
200
250
Channel
Solution
1
0.9
0.8
0.7
0.6
0.5
0.4
0.3
0.2
0.1
0
0.01
1
100
1e+4
1e+6
1e+8
1e+10
Intensity Distrib (nm)
Peak Analysis
Files: cc11_331.txt
cc11_331.txt Intensity Distrib, (nm)
Distribution analysis
Fitting range : [55; 115] channels
Number of Intervals : 200
Boundaries : [5.6e-4; 7.7e+9]
Resolution : 0
Peak Num | Area | Mean | Position | STD
1 | 1.000 | 88.90 | 94.17 | 21.18
χ² : 3.0e-4

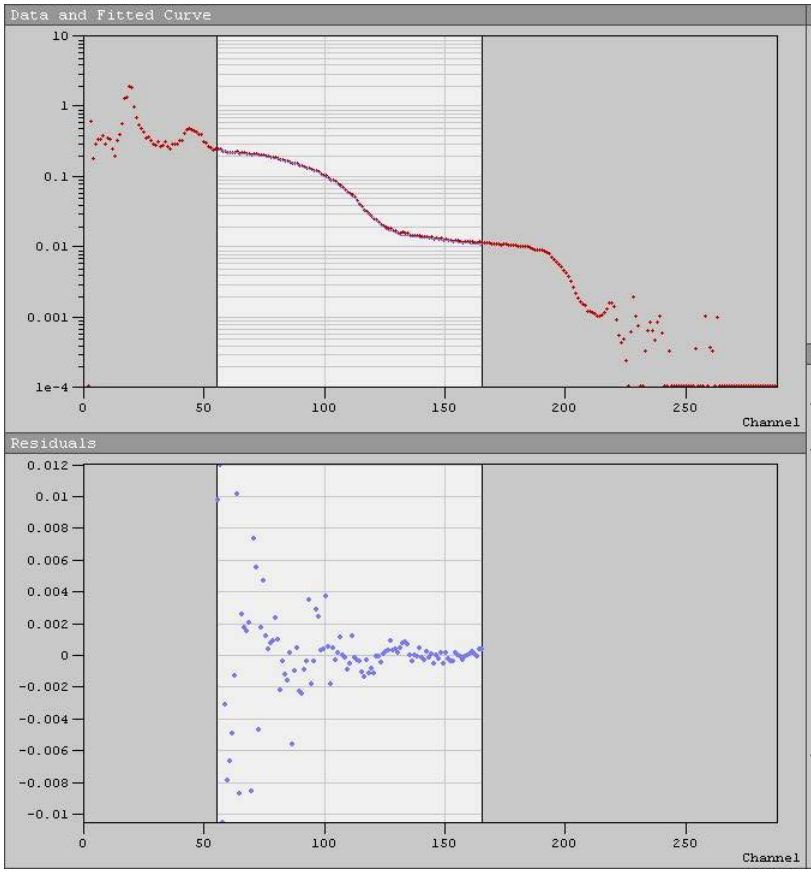
Data and Fitted Curve
10
1
0.1
0.01
0.001
1e-4
0
50
100
150
200
250
Channel
Residuals
0.012
0.01
0.008
0.006
0.004
0.002
0
-0.002
-0.004
-0.006
-0.008
-0.01
0
50
100
150
200
250
Channel

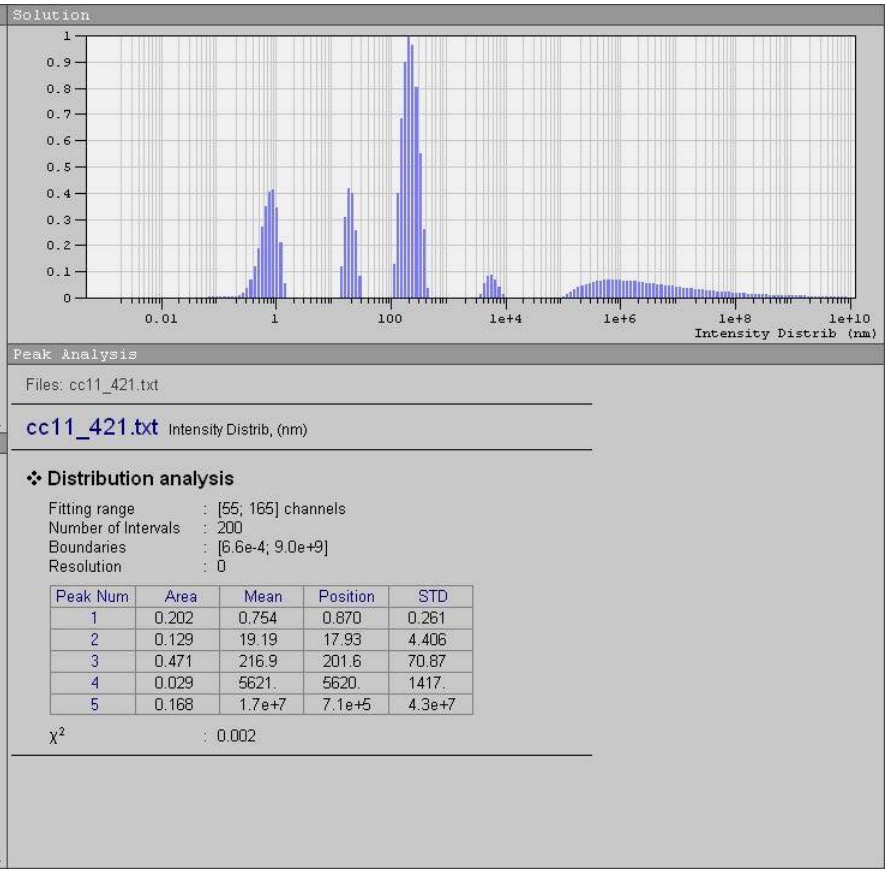
Solution
1
0.9
0.8
0.7
0.6
0.5
0.4
0.3
0.2
0.1
0
0.01
1
100
1e+4
1e+6
1e+8
1e+10
Intensity Distrib (nm)
Peak Analysis
Files: cc11_421.txt
cc11_421.txt Intensity Distrib, (nm)
❖ Distribution analysis
Fitting range : [55; 165] channels
Number of Intervals : 200
Boundaries : [6.6e-4; 9.0e+9]
Resolution : 0
Peak Num | Area | Mean | Position | STD
1 | 0.202 | 0.754 | 0.870 | 0.261
2 | 0.129 | 19.19 | 17.93 | 4.406
3 | 0.471 | 216.9 | 201.6 | 70.87
4 | 0.029 | 5621. | 5620. | 1417.
5 | 0.168 | 1.7e+7 | 7.1e+5 | 4.3e+7
χ² : 0.002

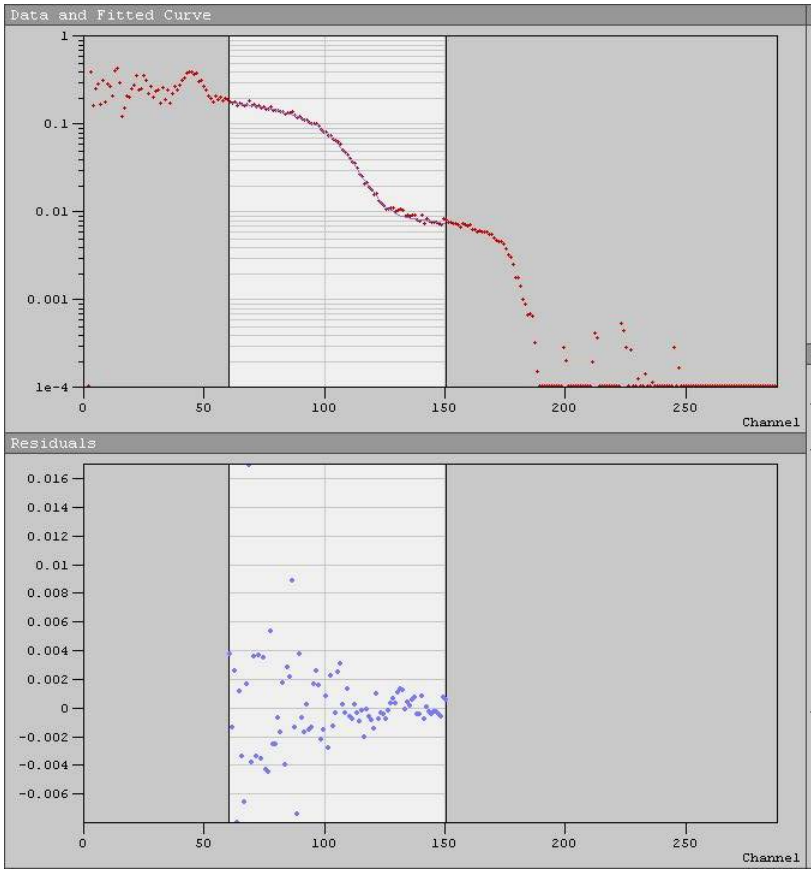
Data and Fitted Curve
1
0.1
0.01
0.001
1e-4
0
50
100
150
200
250
Channel
Residuals
0.016
0.014
0.012
0.01
0.008
0.006
0.004
0.002
0
-0.002
-0.004
-0.006
0
50
100
150
200
250
Channel

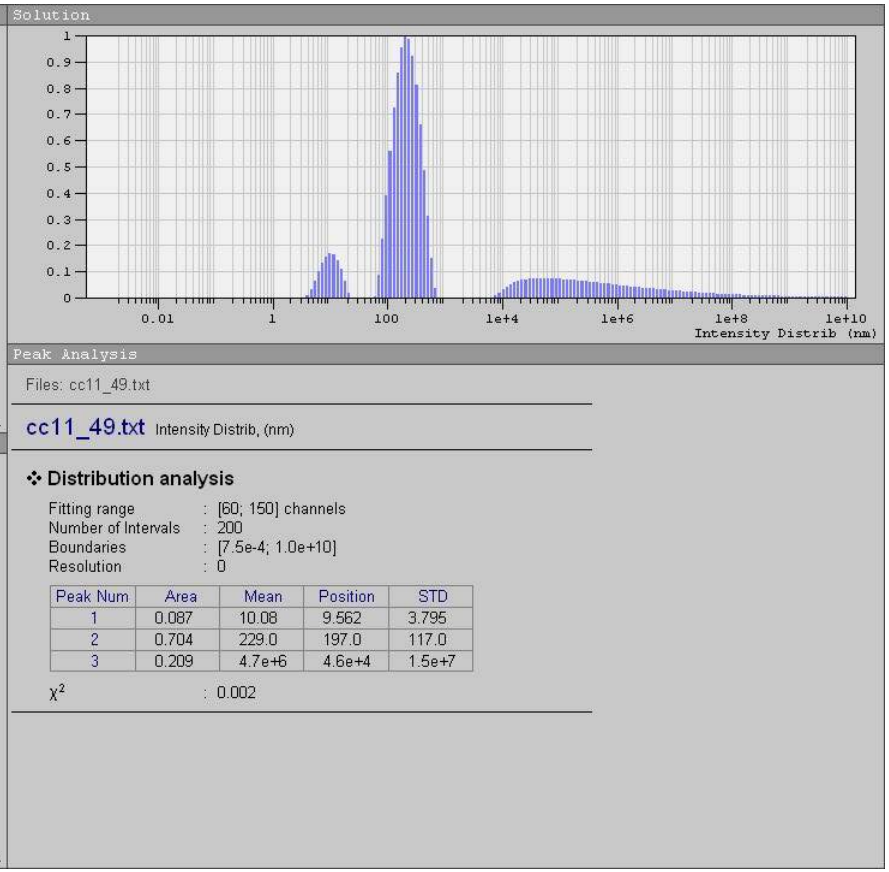
Solution
1
0.9
0.8
0.7
0.6
0.5
0.4
0.3
0.2
0.1
0
0.01
1
100
1e+4
1e+6
1e+8
1e+10
Intensity Distrib (nm)
Peak Analysis
Files: cc11_49.txt
cc11_49.txt Intensity Distrib, (nm)
❖ Distribution analysis
Fitting range : [60; 150] channels
Number of Intervals : 200
Boundaries : [7.5e-4; 1.0e+10]
Resolution : 0
Peak Num | Area | Mean | Position | STD
1 | 0.087 | 10.08 | 9.562 | 3.795
2 | 0.704 | 229.0 | 197.0 | 117.0
3 | 0.209 | 4.7e+6 | 4.6e+4 | 1.5e+7
χ² : 0.002

											Unimer		Micelle	
Sample	Run Name	Copolymer Concentration	Solvent Composition	Phase	T	n	η	Intensity	Min Channel	Max Channel	peak	mean	peak	mean
-	-	wt%	mol% methanol	-	C	-	cP	cps	-	-	nm	nm	nm	nm
MC3	MC326L	0.19	33.4	lower	26.5	1.3565	0.612	103,948	55	100	0.546	0.463	11.26	10.45
MC3	MC3L27	0.19	33.4	lower	27	1.357	0.6	105,974	55	100	0.413	0.391	11.51	10.79
MC3	mc3l422	0.19	33.4	lower	42	1.364	0.51	189,279	55	95	0.811	0.703	16.71	18.53
MC4	MC4L27	0.19	51.7	lower	27	1.357	0.6	34,099	55	100	0.88	0.769	11.51	11.31
MC4	mc4l403	0.19	51.7	lower	39.5	1.3615	0.525	15,232	55	90	0.906	0.875	10.19	10.28
MC4	mc4l428	0.19	51.7	lower	42	1.364	0.51	9,594	55	85	-	-	5.796	5.716
MC4	mcl423	0.19	51.7	lower	42	1.364	0.51	10,267	55	85	-	-	5.018	4.283
MC4	MC4L43.5 (3)	0.19	51.7	lower	43.5	1.3665	0.5025	19,177	55	75	-	-	5.099	5.222
MC4	MC4L45 (3)	0.19	51.7	lower	45	1.37067	0.55	33,095	55	80	-	-	6.373	6.388
MC4	MC4S49.5 15 min	0.19	51.7	single	49.5	1.3775	0.55	27,379	55	85	-	-	5.612	5.388
MC4	MC4S49.5 30 min	0.19	51.7	single	49.5	1.3775	0.55	27,349	55	85	-	-	5.612	5.477
MC4	mc4u_426	0.19	51.7	upper	42	1.397	0.62	2,771	55	70	-	-	1.735	2.42
MC4	MC4U43.5	0.19	51.7	upper	43.5	1.394	0.605	6,672	55	80	-	-	3.789	4.801
MC4	MC4U45.5 (1)	0.19	51.7	upper	45.5	1.386	0.6	34,237	55	80	-	-	6.96	7.428
MC5	MC5L26_2	0.20	67.3	lower	26	1.3562	0.615	28,236	55	100	0.7	?	11.18	11.91
MC5	mc5l422	0.20	67.3	lower	42	1.364	0.51	8,876	55	85	-	-	5.796	7.99

Table C.3: DLS results for the binary solvent system.

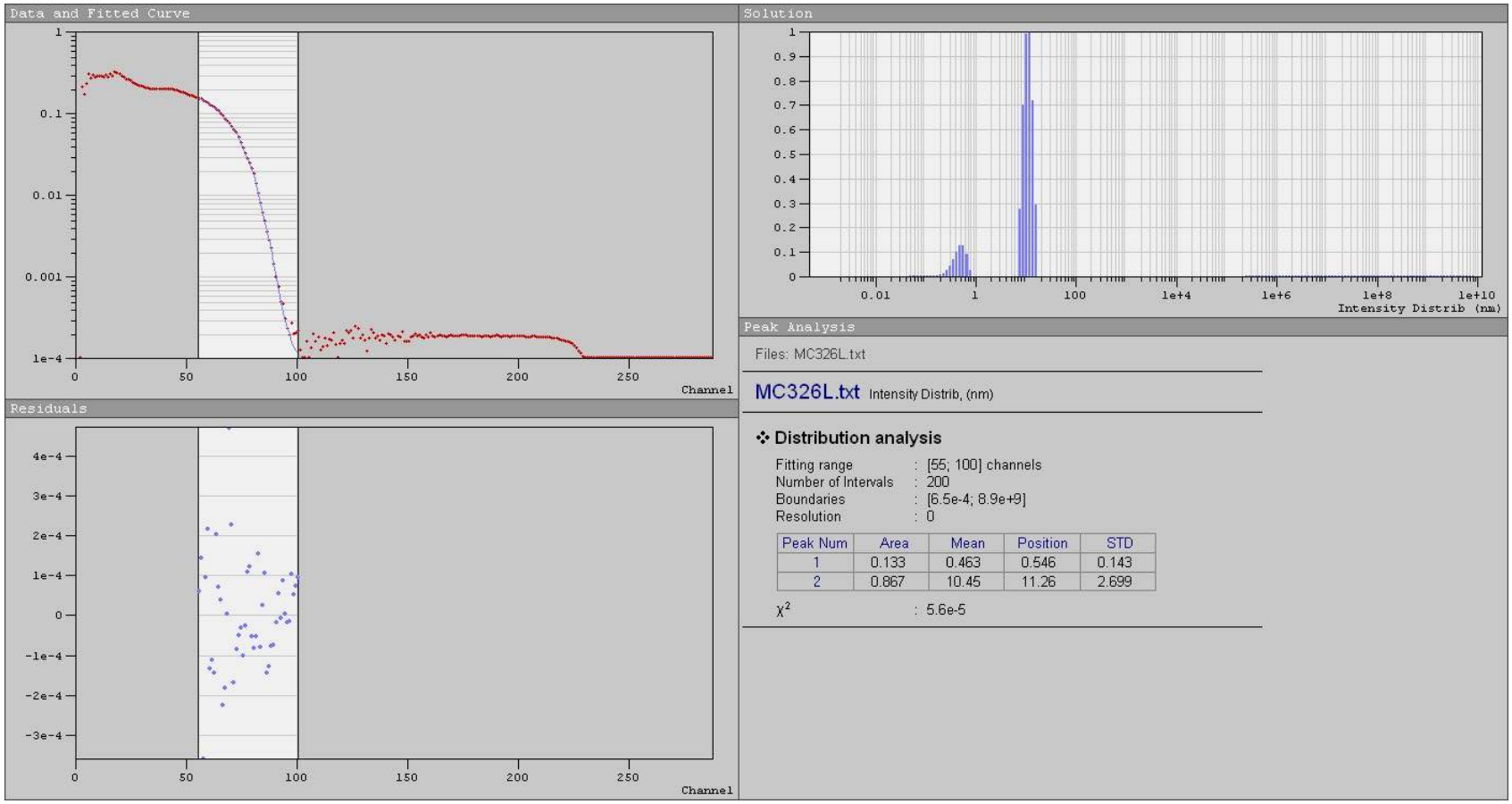
Data and Fitted Curve
1
0.1
0.01
0.001
1e-4
0
50
100
150
200
250
Channel
Residuals
4e-4
3e-4
2e-4
1e-4
0
-1e-4
-2e-4
-3e-4
0
50
100
150
200
250
Channel
Solution
1
0.9
0.8
0.7
0.6
0.5
0.4
0.3
0.2
0.1
0
0.01
1
100
1e+4
1e+6
1e+8
1e+10
Intensity Distrib (nm)
Peak Analysis
Files: MC326L.txt
MC326L.txt Intensity Distrib, (nm)
Distribution analysis
Fitting range : [55; 100] channels
Number of Intervals : 200
Boundaries : [6.5e-4; 8.9e+9]
Resolution : 0
Peak Num | Area | Mean | Position | STD
1 | 0.133 | 0.463 | 0.546 | 0.143
2 | 0.867 | 10.45 | 11.26 | 2.699
χ² : 5.6e-5

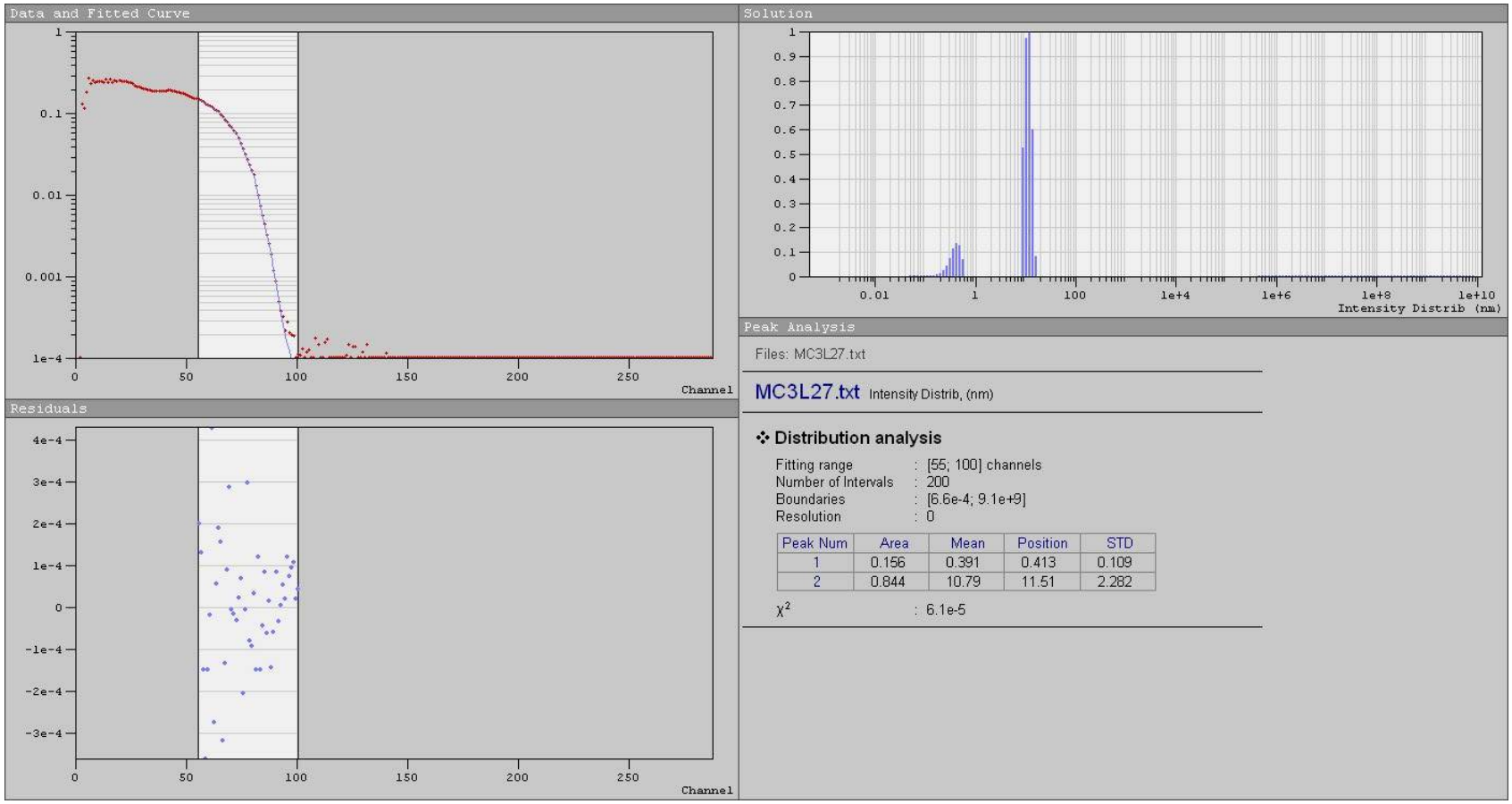
Data and Fitted Curve
1
0.1
0.01
0.001
1e-4
0
50
100
150
200
250
Channel
Residuals
4e-4
3e-4
2e-4
1e-4
0
-1e-4
-2e-4
-3e-4
0
50
100
150
200
250
Channel
Solution
1
0.9
0.8
0.7
0.6
0.5
0.4
0.3
0.2
0.1
0
0.01
1
100
1e+4
1e+6
1e+8
1e+10
Intensity Distrib (nm)
Peak Analysis
Files: MC3L27.txt
MC3L27.txt Intensity Distrib, (nm)
Distribution analysis
Fitting range : [55; 100] channels
Number of Intervals : 200
Boundaries : [6.6e-4; 9.1e+9]
Resolution : 0
Peak Num | Area | Mean | Position | STD
1 | 0.156 | 0.391 | 0.413 | 0.109
2 | 0.844 | 10.79 | 11.51 | 2.282
χ² : 6.1e-5

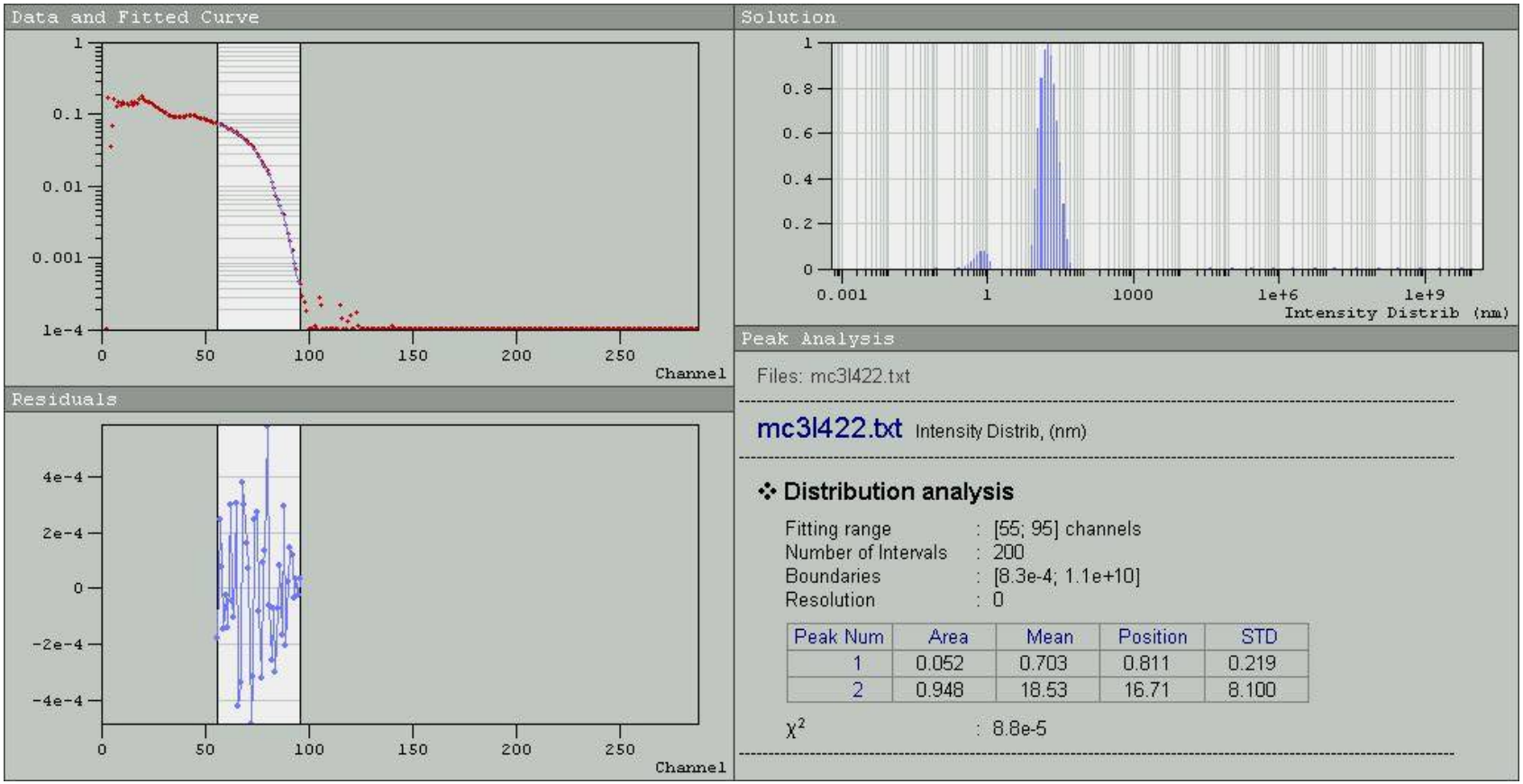
Data and Fitted Curve
1
0.1
0.01
0.001
1e-4
0
50
100
150
200
250
Channel
Residuals
4e-4
2e-4
0
-2e-4
-4e-4
0
50
100
150
200
250
Channel
Solution
1
0.8
0.6
0.4
0.2
0
0.001
1
1000
1e+6
1e+9
Intensity Distrib (nm)
Peak Analysis
Files: mc3l422.txt
mc3l422.txt Intensity Distrib, (nm)
Distribution analysis
Fitting range : [55; 95] channels
Number of Intervals : 200
Boundaries : [8.3e-4; 1.1e+10]
Resolution : 0
Peak Num | Area | Mean | Position | STD
1 | 0.052 | 0.703 | 0.811 | 0.219
2 | 0.948 | 18.53 | 16.71 | 8.100
χ² : 8.8e-5

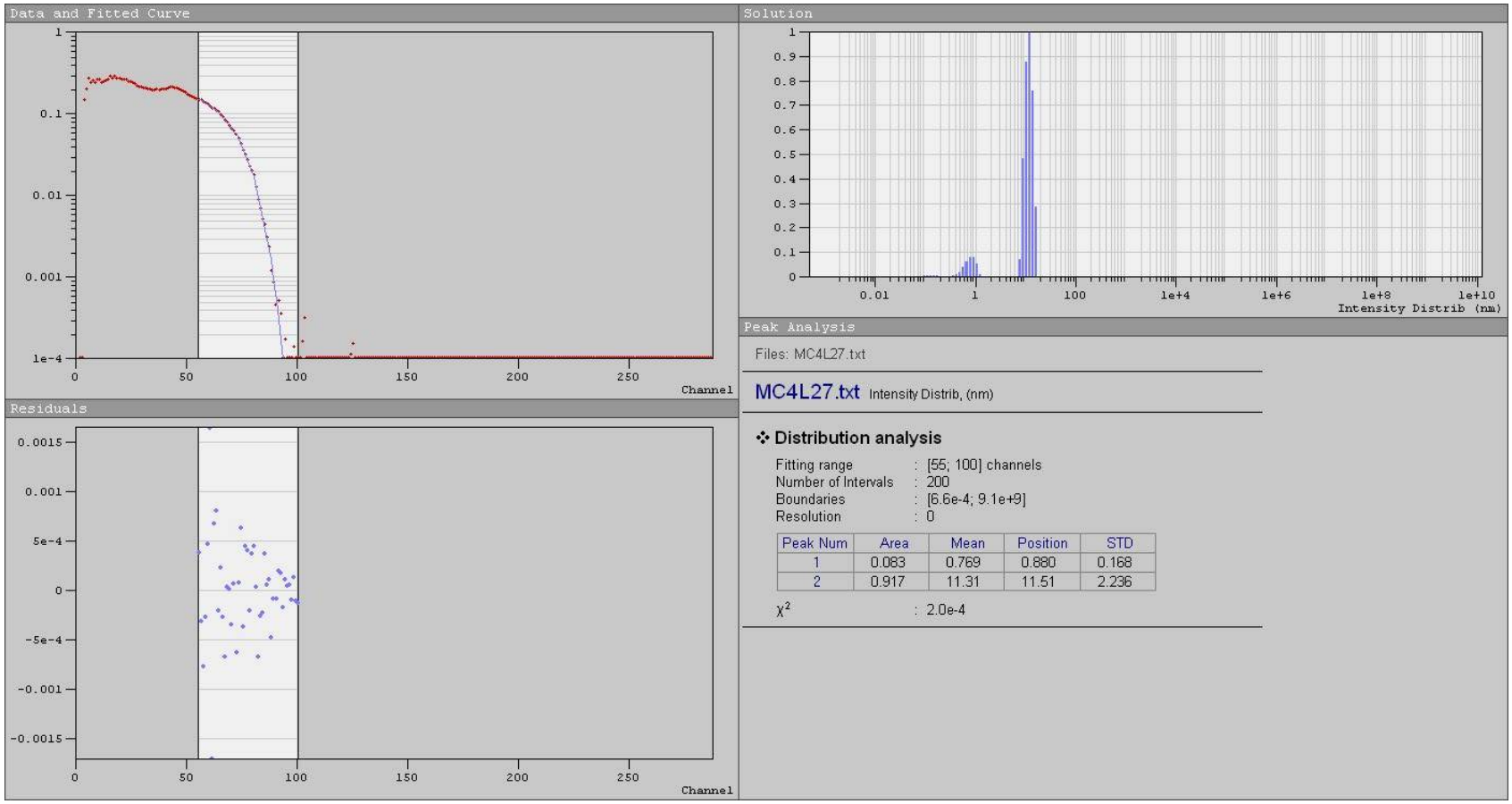
Data and Fitted Curve
Channel
Residuals
Channel
Solution
Intensity Distrib (nm)
Peak Analysis
Files: MC4L27.txt
MC4L27.txt Intensity Distrib, (nm)
Distribution analysis
Fitting range : [55; 100] channels
Number of Intervals : 200
Boundaries : [6.6e-4; 9.1e+9]
Resolution : 0
Peak Num | Area | Mean | Position | STD
1 | 0.083 | 0.769 | 0.880 | 0.168
2 | 0.917 | 11.31 | 11.51 | 2.236
χ² : 2.0e-4

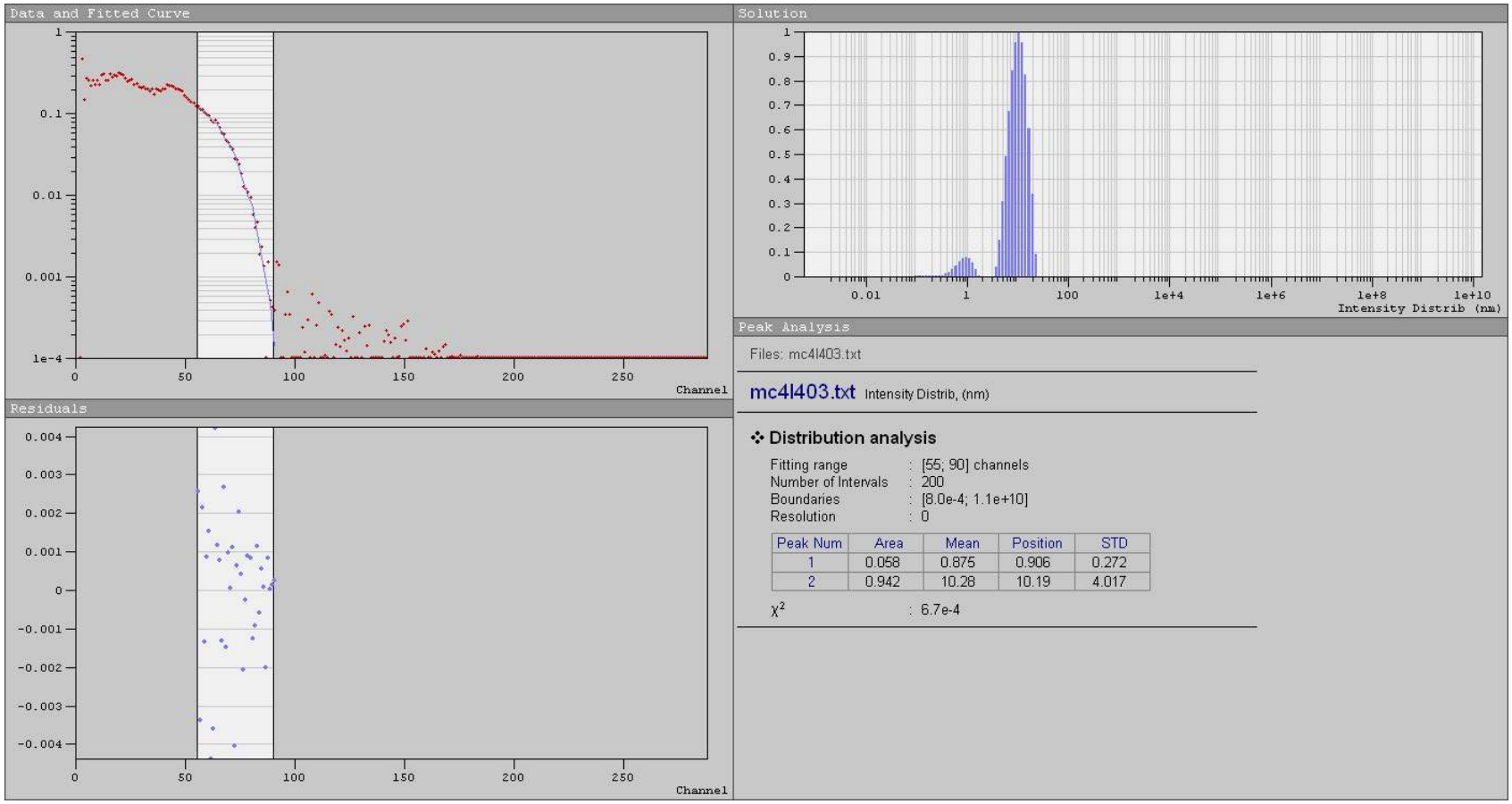
Data and Fitted Curve
Channel
Residuals
Channel
Solution
Intensity Distrib (nm)
Peak Analysis
Files: mc4l403.txt
mc4l403.txt Intensity Distrib, (nm)
Distribution analysis
Fitting range : [55, 90] channels
Number of Intervals : 200
Boundaries : [8.0e-4; 1.1e+10]
Resolution : 0
Peak Num | Area | Mean | Position | STD
1 | 0.058 | 0.875 | 0.906 | 0.272
2 | 0.942 | 10.28 | 10.19 | 4.017
χ² : 6.7e-4

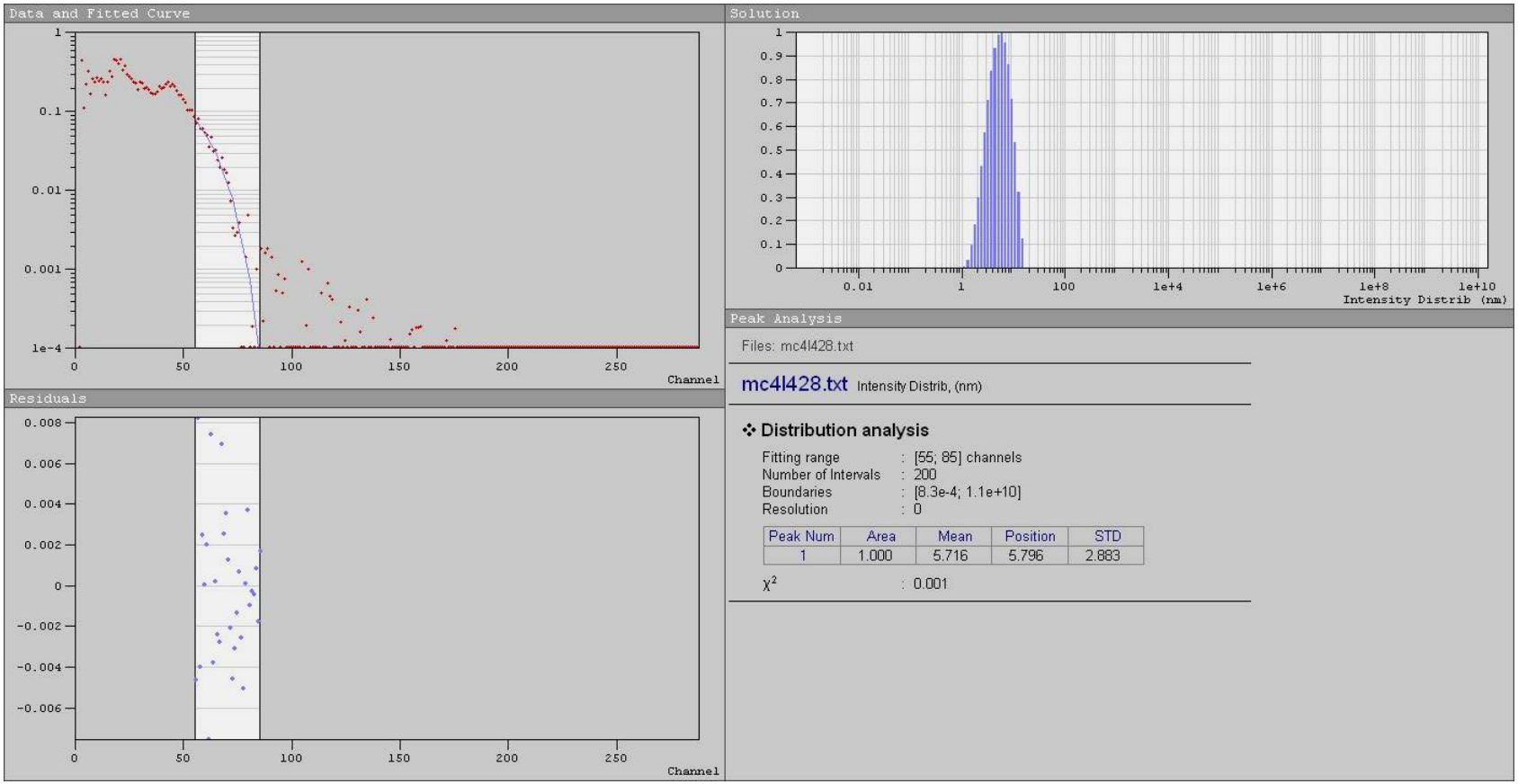
Data and Fitted Curve
1
0.1
0.01
0.001
1e-4
0
50
100
150
200
250
Channel
Residuals
0.008
0.006
0.004
0.002
0
-0.002
-0.004
-0.006
0
50
100
150
200
250
Channel
Solution
1
0.9
0.8
0.7
0.6
0.5
0.4
0.3
0.2
0.1
0
0.01
1
100
1e+4
1e+6
1e+8
1e+10
Intensity Distrib (nm)
Peak Analysis
Files: mc4l428.txt
mc4l428.txt Intensity Distrib, (nm)
❖ Distribution analysis
Fitting range : [55; 85] channels
Number of Intervals : 200
Boundaries : [8.3e-4; 1.1e+10]
Resolution : 0
Peak Num | Area | Mean | Position | STD
1 | 1.000 | 5.716 | 5.796 | 2.883
χ² : 0.001

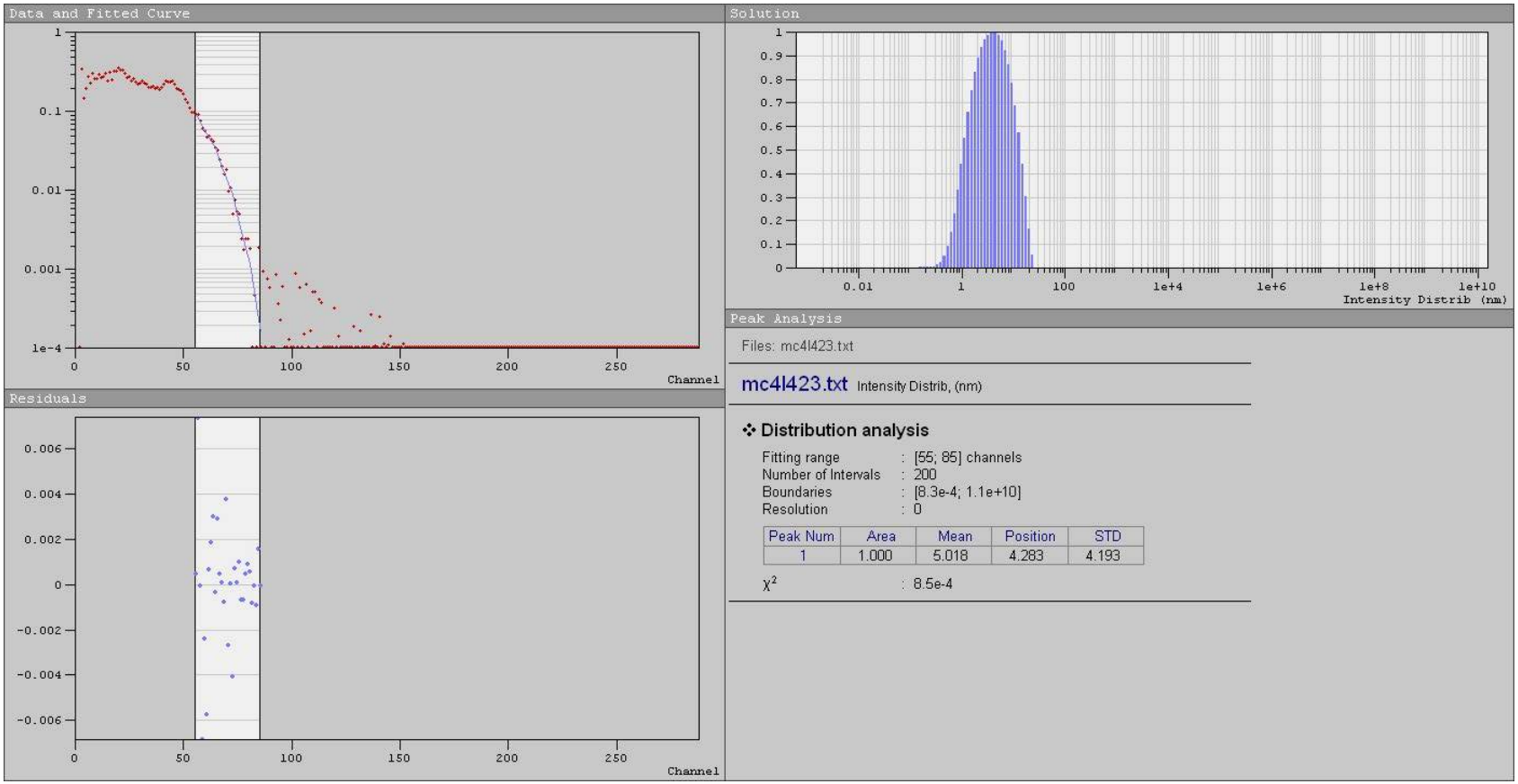
Data and Fitted Curve
1
0.1
0.01
0.001
1e-4
0
50
100
150
200
250
Channel
Residuals
0.006
0.004
0.002
0
-0.002
-0.004
-0.006
0
50
100
150
200
250
Channel
Solution
1
0.9
0.8
0.7
0.6
0.5
0.4
0.3
0.2
0.1
0
0.01
1
100
1e+4
1e+6
1e+8
1e+10
Intensity Distrib (nm)
Peak Analysis
Files: mc4l423.txt
mc4l423.txt Intensity Distrib, (nm)
❖ Distribution analysis
Fitting range : [55; 85] channels
Number of Intervals : 200
Boundaries : [8.3e-4; 1.1e+10]
Resolution : 0
Peak Num | Area | Mean | Position | STD
1 | 1.000 | 5.018 | 4.283 | 4.193
χ² : 8.5e-4

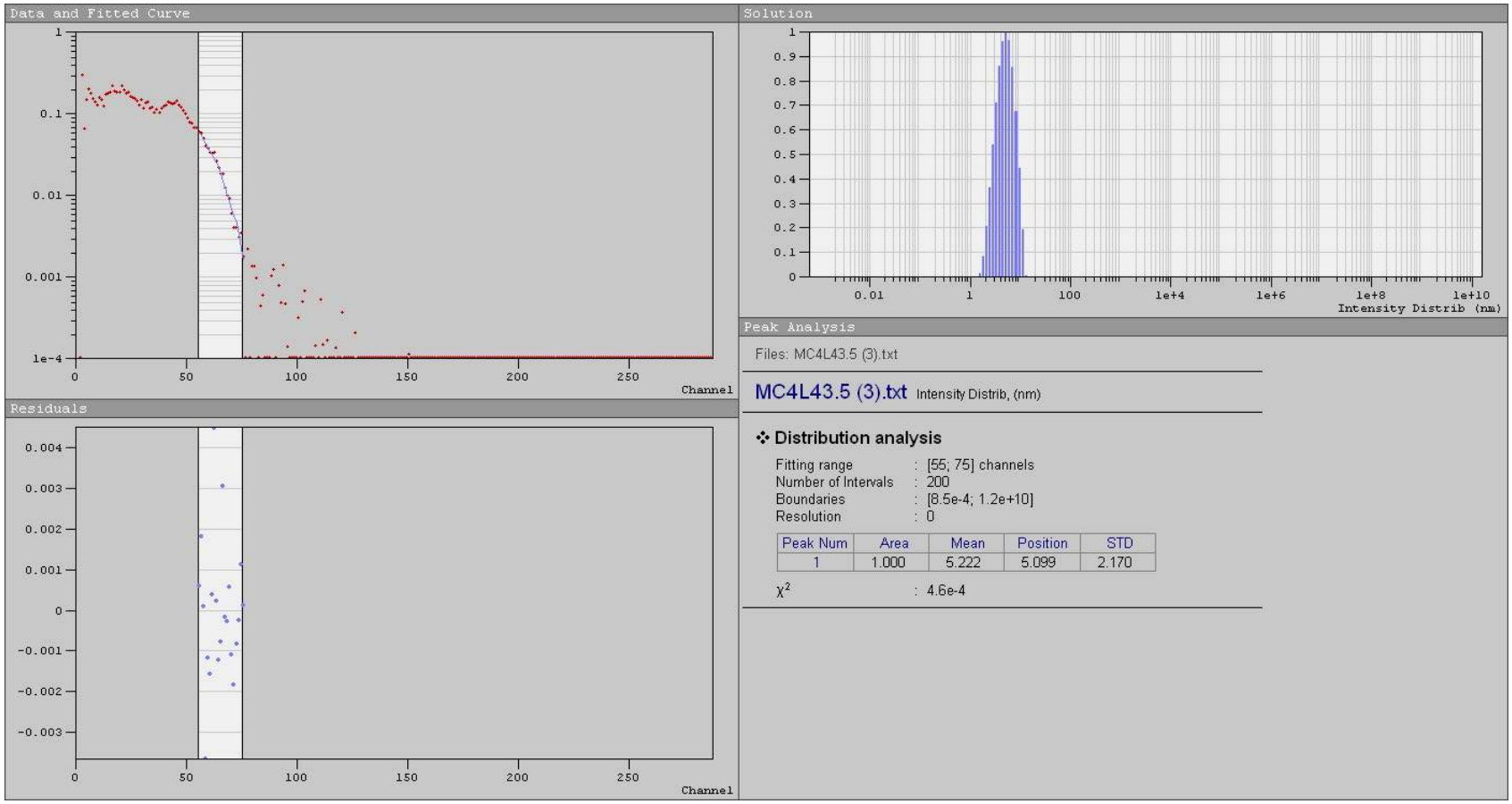
Data and Fitted Curve
1
0.1
0.01
0.001
1e-4
0
50
100
150
200
250
Channel
Residuals
0.004
0.003
0.002
0.001
0
-0.001
-0.002
-0.003
0
50
100
150
200
250
Channel
Solution
1
0.9
0.8
0.7
0.6
0.5
0.4
0.3
0.2
0.1
0
0.01
1
100
1e+4
1e+6
1e+8
1e+10
Intensity Distrib (nm)
Peak Analysis
Files: MC4L43.5 (3).txt
MC4L43.5 (3).txt Intensity Distrib, (nm)
Distribution analysis
Fitting range : [55; 75] channels
Number of Intervals : 200
Boundaries : [8.5e-4; 1.2e+10]
Resolution : 0
Peak Num | Area | Mean | Position | STD
1 | 1.000 | 5.222 | 5.099 | 2.170
χ² : 4.6e-4

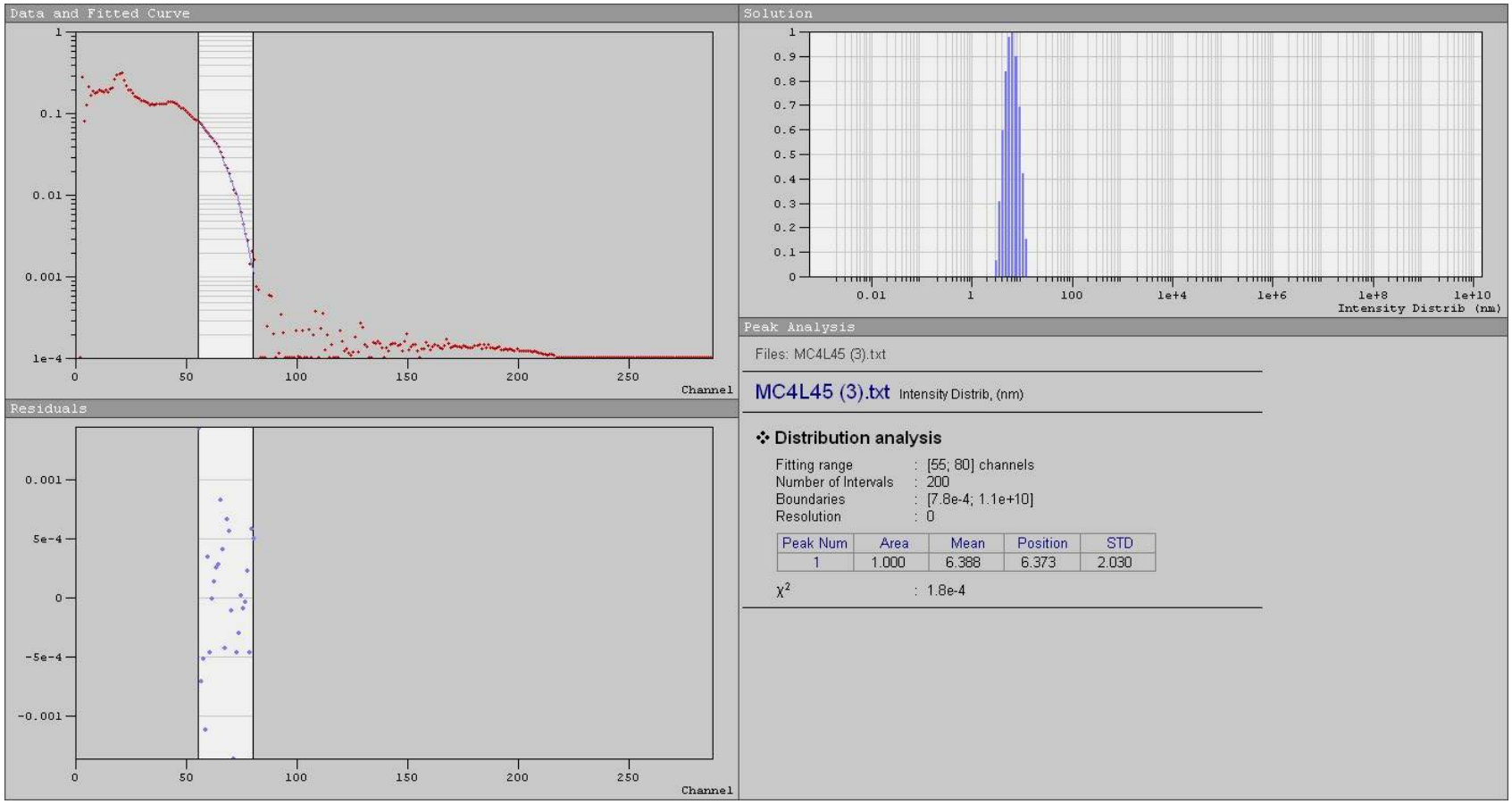
Data and Fitted Curve
1
0.1
0.01
0.001
1e-4
0
50
100
150
200
250
Channel
Residuals
0.001
5e-4
0
-5e-4
-0.001
0
50
100
150
200
250
Channel
Solution
1
0.9
0.8
0.7
0.6
0.5
0.4
0.3
0.2
0.1
0
0.01
1
100
1e+4
1e+6
1e+8
1e+10
Intensity Distrib (nm)
Peak Analysis
Files: MC4L45 (3).txt
MC4L45 (3).txt Intensity Distrib, (nm)
Distribution analysis
Fitting range : [55; 80] channels
Number of Intervals : 200
Boundaries : [7.8e-4; 1.1e+10]
Resolution : 0
Peak Num | Area | Mean | Position | STD
1 | 1.000 | 6.388 | 6.373 | 2.030
χ² : 1.8e-4

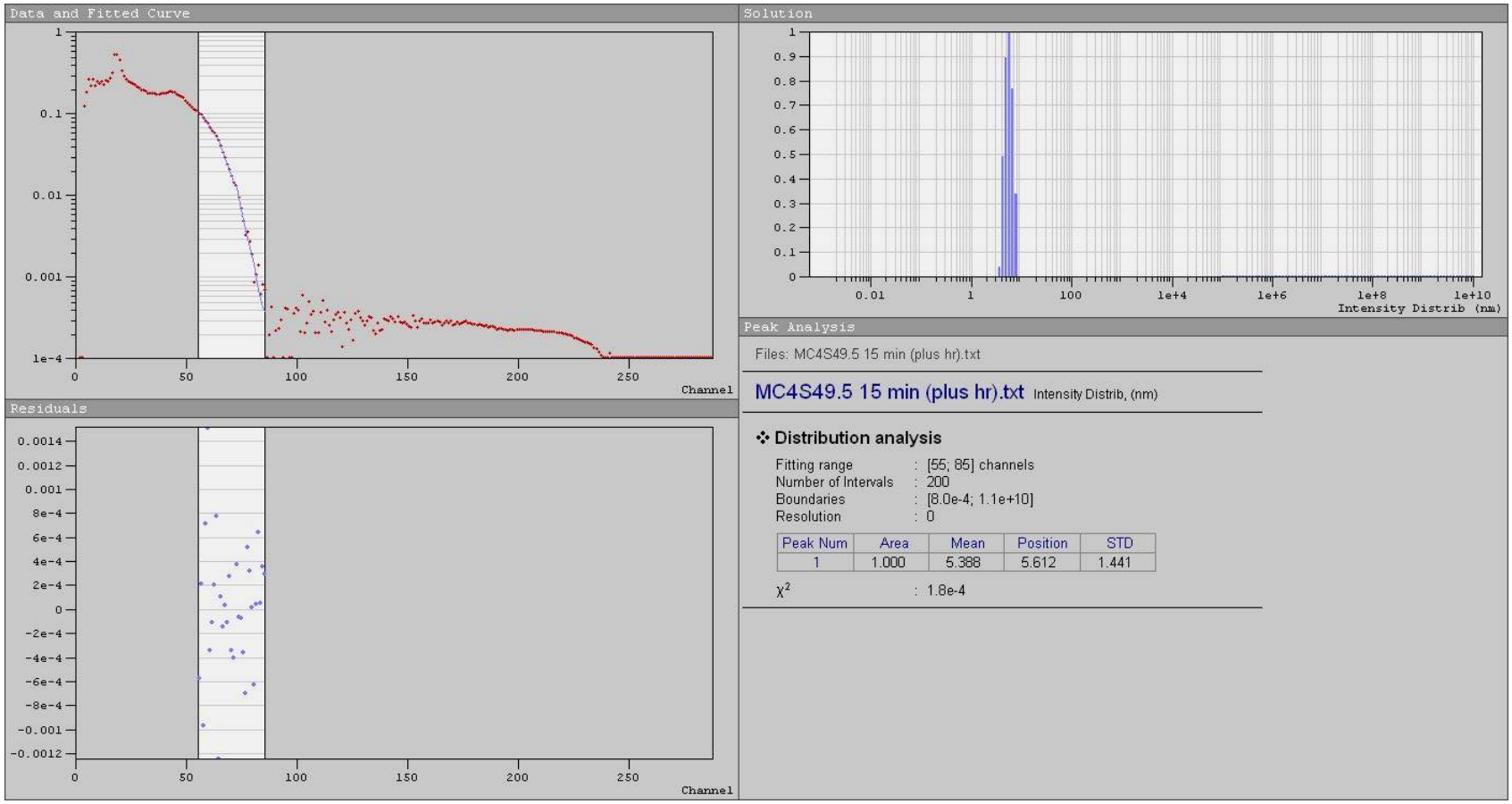
Data and Fitted Curve
1
0.1
0.01
0.001
1e-4
0
50
100
150
200
250
Channel
Residuals
0.0014
0.0012
0.001
8e-4
6e-4
4e-4
2e-4
0
-2e-4
-4e-4
-6e-4
-8e-4
-0.001
-0.0012
0
50
100
150
200
250
Channel
Solution
1
0.9
0.8
0.7
0.6
0.5
0.4
0.3
0.2
0.1
0
0.01
1
100
1e+4
1e+6
1e+8
1e+10
Intensity Distrib (nm)
Peak Analysis
Files: MC4S49.5 15 min (plus hr).txt
MC4S49.5 15 min (plus hr).txt Intensity Distrib, (nm)
Distribution analysis
Fitting range : [55; 85] channels
Number of Intervals : 200
Boundaries : [8.0e-4; 1.1e+10]
Resolution : 0
Peak Num | Area | Mean | Position | STD
1 | 1.000 | 5.388 | 5.612 | 1.441
χ2 : 1.8e-4

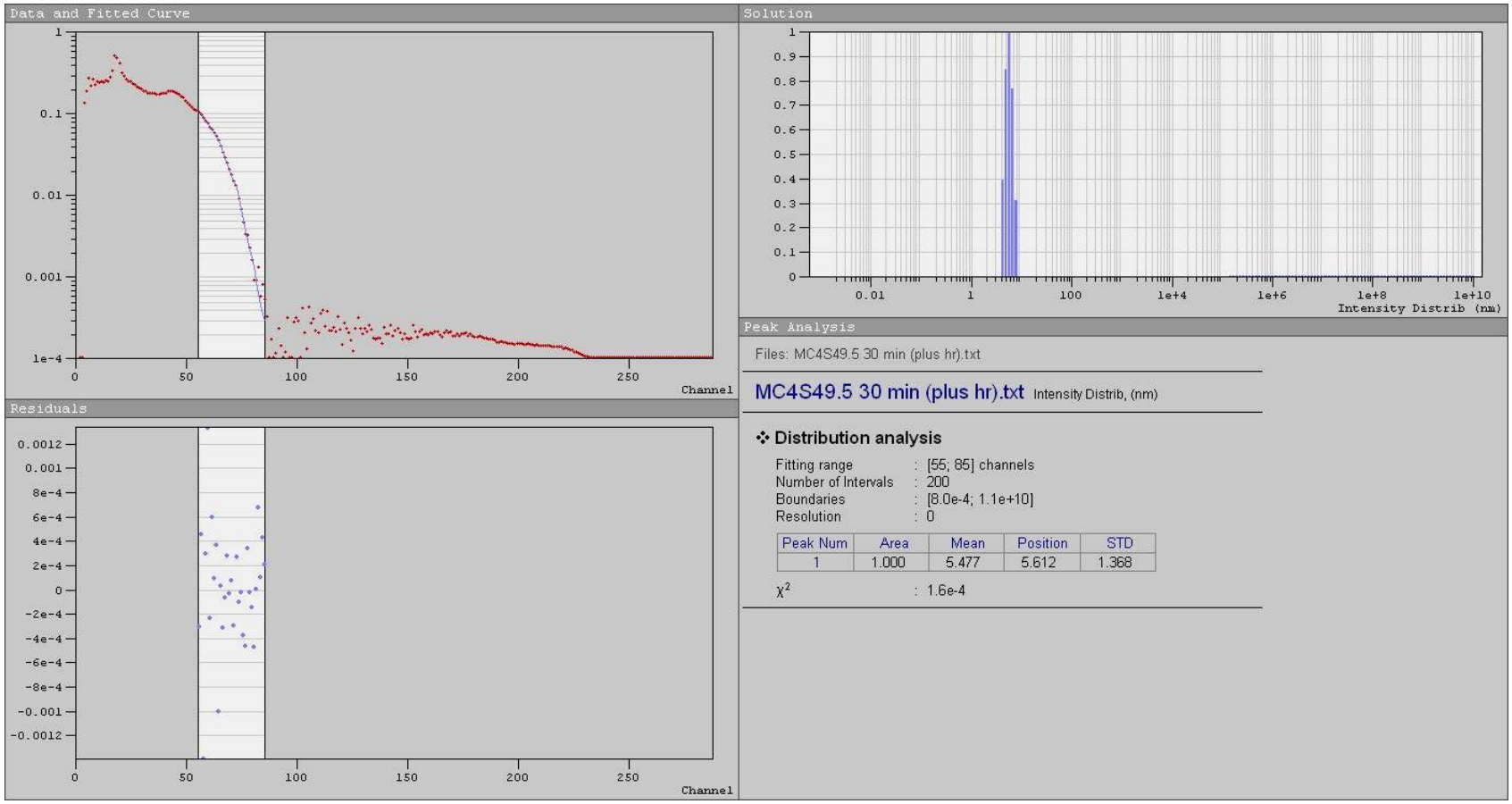
Data and Fitted Curve
1
0.1
0.01
0.001
1e-4
0
50
100
150
200
250
Channel
Residuals
0.0012
0.001
8e-4
6e-4
4e-4
2e-4
0
-2e-4
-4e-4
-6e-4
-8e-4
-0.001
-0.0012
0
50
100
150
200
250
Channel
Solution
1
0.9
0.8
0.7
0.6
0.5
0.4
0.3
0.2
0.1
0
0.01
1
100
1e+4
1e+6
1e+8
1e+10
Intensity Distrib (nm)
Peak Analysis
Files: MC4S49.5 30 min (plus hr).txt
MC4S49.5 30 min (plus hr).txt Intensity Distrib, (nm)
Distribution analysis
Fitting range : [55; 85] channels
Number of Intervals : 200
Boundaries : [8.0e-4; 1.1e+10]
Resolution : 0
Peak Num | Area | Mean | Position | STD
1 | 1.000 | 5.477 | 5.612 | 1.368
χ² : 1.6e-4

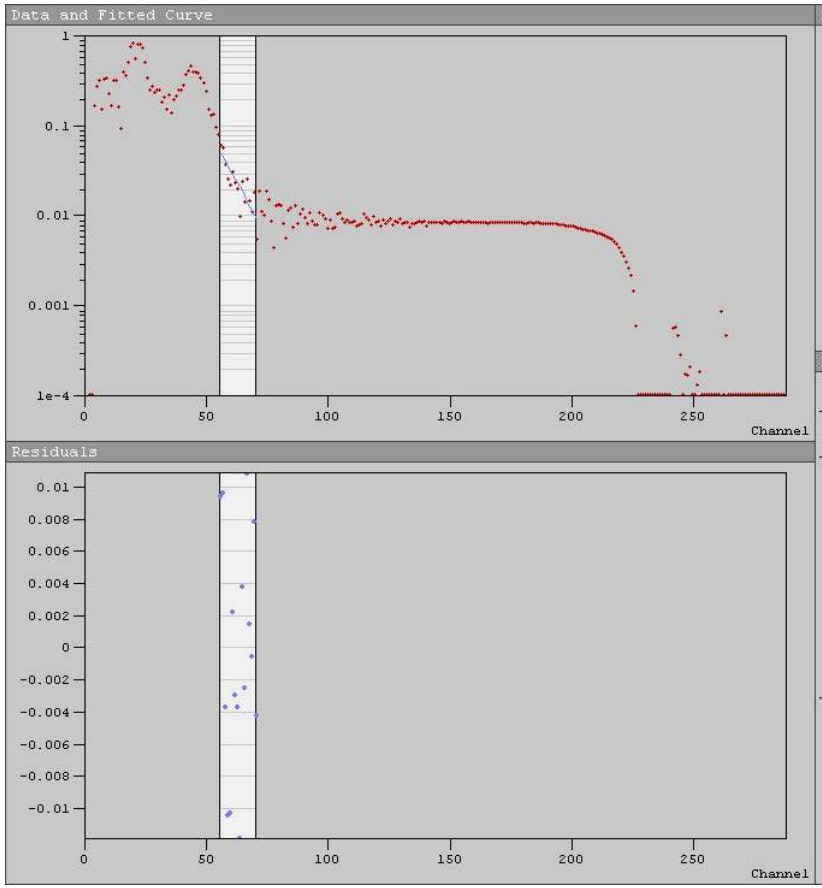

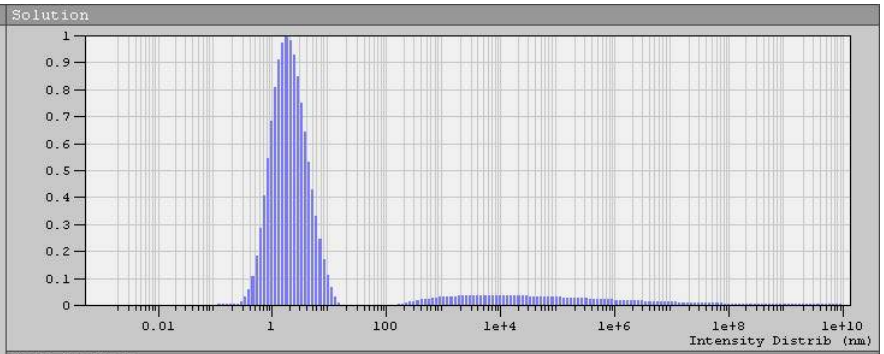

Peak Analysis

Files: mc4u_426.txt

mc4u_426.txt Intensity Distrib, (nm)

Distribution analysis

Fitting range : [55; 70] channels
Number of Intervals : 200
Boundaries : [7.2e-4; 9.8e+9]
Resolution : 0

Peak Num	Area	Mean	Position	STD
1	0.876	2.420	1.735	1.887
2	0.124	4.8e+5	6117.	1.3e+6

χ^2 : 0.002

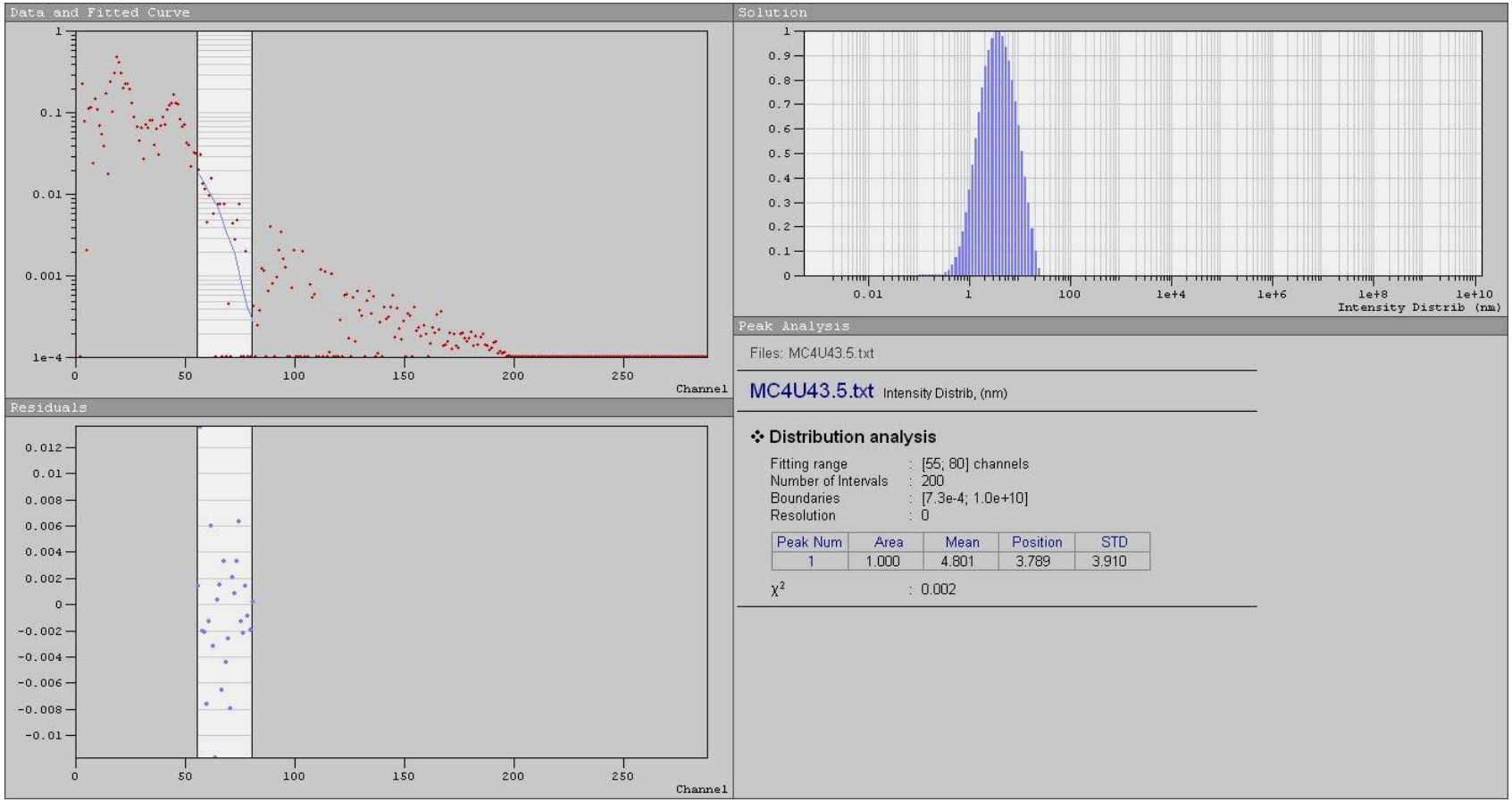
Data and Fitted Curve
1
0.1
0.01
0.001
1e-4
0
50
100
150
200
250
Channel
Residuals
0.012
0.01
0.008
0.006
0.004
0.002
0
-0.002
-0.004
-0.006
-0.008
-0.01
0
50
100
150
200
250
Channel
Solution
1
0.9
0.8
0.7
0.6
0.5
0.4
0.3
0.2
0.1
0
0.01
1
100
1e+4
1e+6
1e+8
1e+10
Intensity Distrib (nm)
Peak Analysis
Files: MC4U43.5.txt
MC4U43.5.txt Intensity Distrib, (nm)
Distribution analysis
Fitting range : [55, 80] channels
Number of Intervals : 200
Boundaries : [7.3e-4; 1.0e+10]
Resolution : 0
Peak Num
Area
Mean
Position
STD
1
1.000
4.801
3.789
3.910
χ2 : 0.002

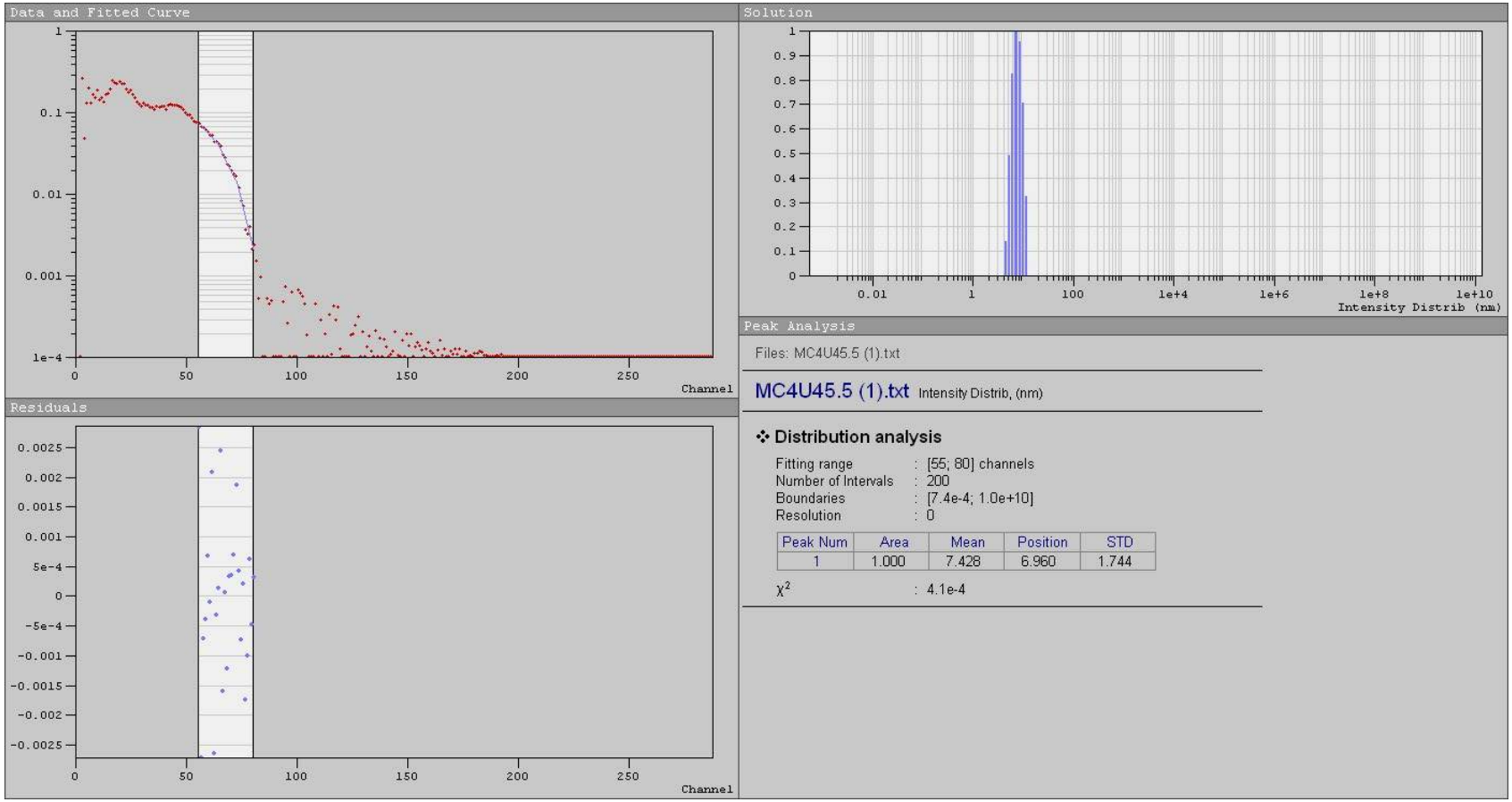
Data and Fitted Curve
1
0.1
0.01
0.001
1e-4
0
50
100
150
200
250
Channel
Residuals
0.0025
0.002
0.0015
0.001
5e-4
0
-5e-4
-0.001
-0.0015
-0.002
-0.0025
0
50
100
150
200
250
Channel
Solution
1
0.9
0.8
0.7
0.6
0.5
0.4
0.3
0.2
0.1
0
0.01
1
100
1e+4
1e+6
1e+8
1e+10
Intensity Distrib (nm)
Peak Analysis
Files: MC4U45.5 (1).txt
MC4U45.5 (1).txt Intensity Distrib, (nm)
Distribution analysis
Fitting range : [55; 80] channels
Number of Intervals : 200
Boundaries : [7.4e-4; 1.0e+10]
Resolution : 0
Peak Num | Area | Mean | Position | STD
1 | 1.000 | 7.428 | 6.960 | 1.744
χ² : 4.1e-4

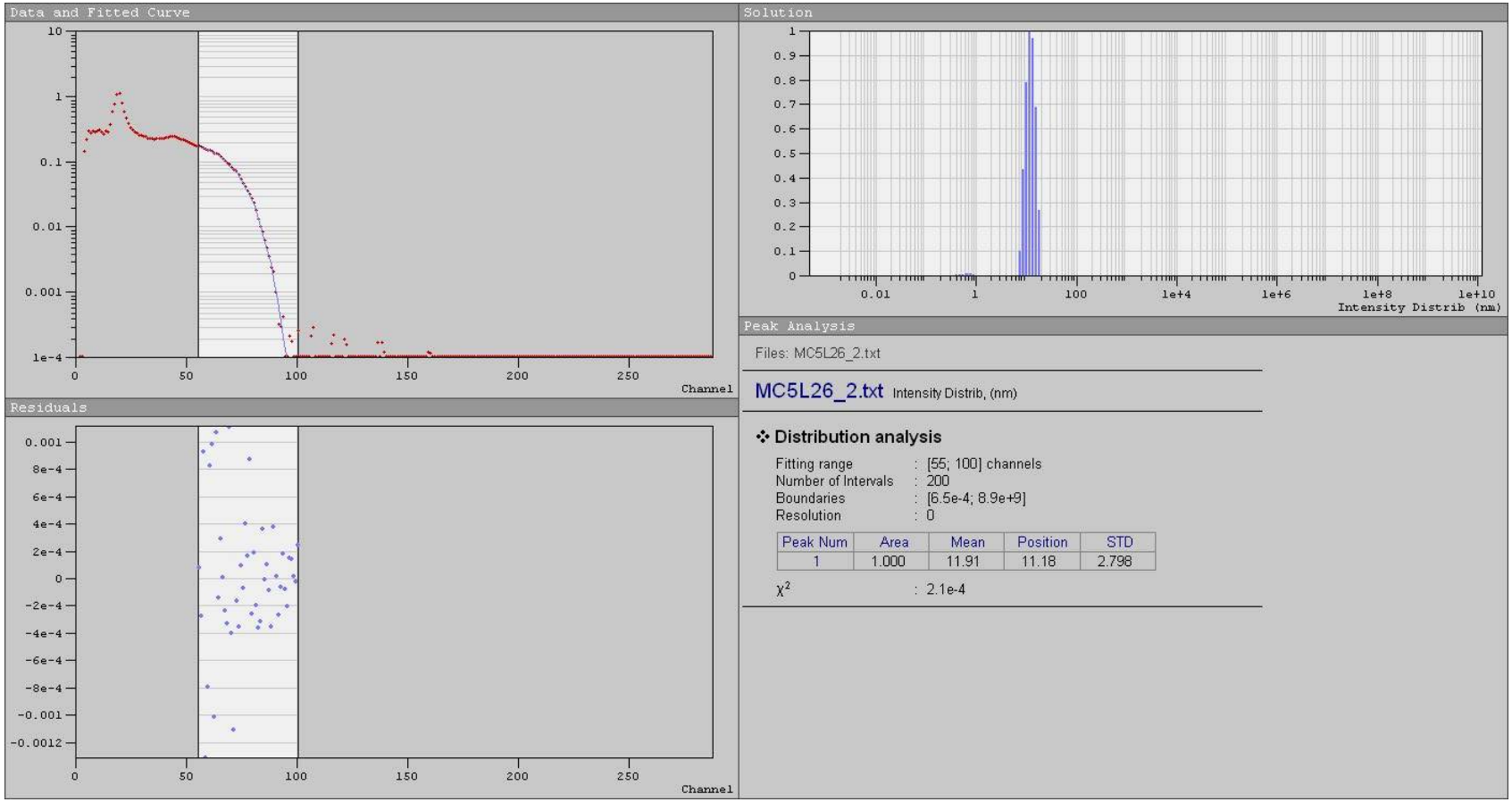
Data and Fitted Curve
Channel
Residuals
Channel
Solution
Intensity Distrib (nm)
Peak Analysis
Files: MC5L26_2.txt
MC5L26_2.txt Intensity Distrib, (nm)
Distribution analysis
Fitting range : [55; 100] channels
Number of Intervals : 200
Boundaries : [6.5e-4; 8.9e+9]
Resolution : 0
Peak Num | Area | Mean | Position | STD
1 | 1.000 | 11.91 | 11.18 | 2.798
χ² : 2.1e-4

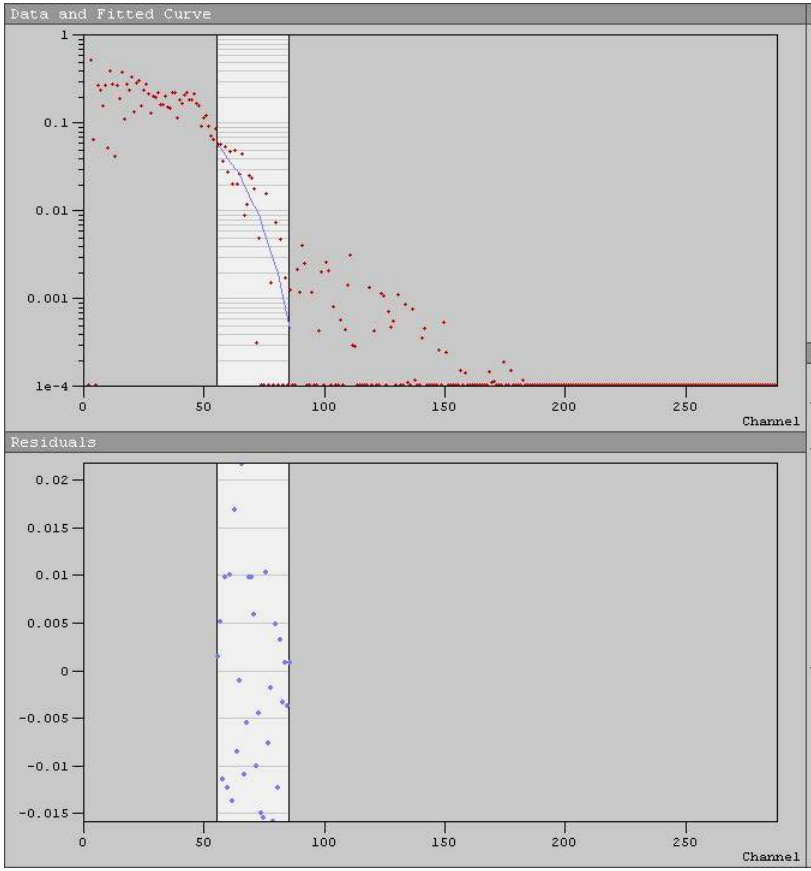
Data and Fitted Curve
1
0.1
0.01
0.001
1e-4
0
50
100
150
200
250
Channel
Residuals
0.02
0.015
0.01
0.005
0
-0.005
-0.01
-0.015
0
50
100
150
200
250
Channel

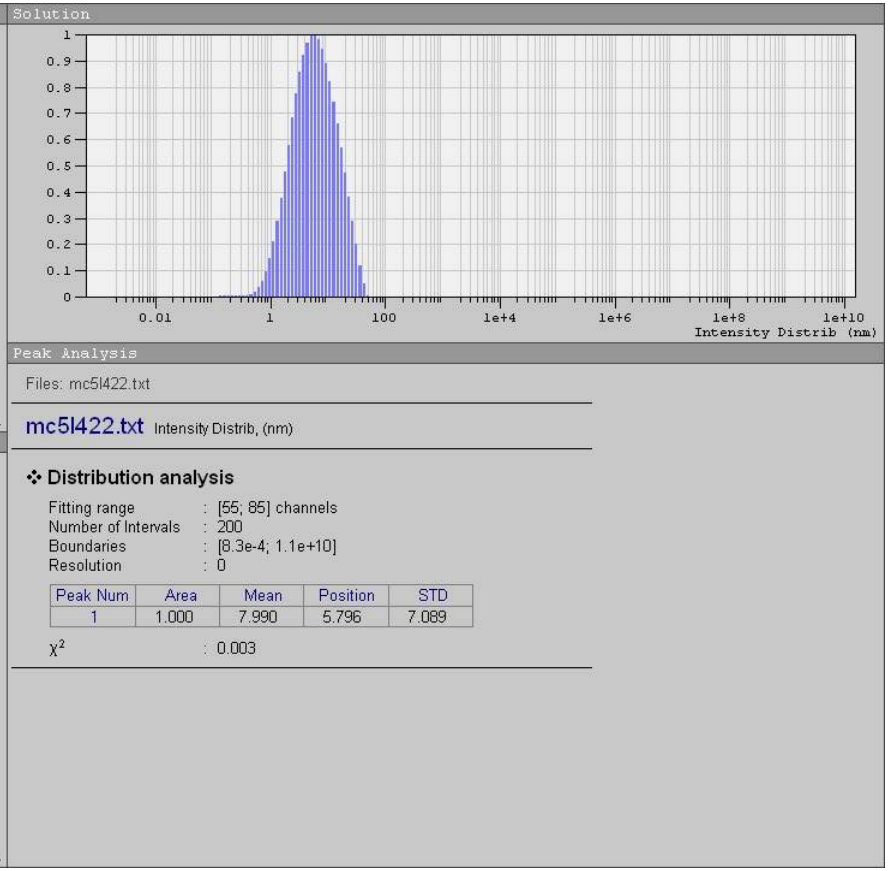
Solution
1
0.9
0.8
0.7
0.6
0.5
0.4
0.3
0.2
0.1
0
0.01
1
100
1e+4
1e+6
1e+8
1e+10
Intensity Distrib (nm)
Peak Analysis
Files: mc5l422.txt
mc5l422.txt Intensity Distrib, (nm)
❖ Distribution analysis
Fitting range : [55; 85] channels
Number of Intervals : 200
Boundaries : [8.3e-4; 1.1e+10]
Resolution : 0
Peak Num | Area | Mean | Position | STD
1 | 1.000 | 7.990 | 5.796 | 7.089
χ² : 0.003

Glossary

^{o}C	degrees Celsius
CMC	critical micelle concentration
CMT	critical micelle temperature
cP	centipoise
cps	counts per second (measure of scattered intensity)
cryo-TEM	cryogenic transmission electron microscopy
CTV	capillary tube viscometry
D	translational diffusion coefficient
DLS	dynamic light scattering
ΔG	Gibbs' free energy change
$G(\tau)$	scattered light intensity autocorrelation function
$g_1(\tau)$	normalized scattered light field autocorrelation function
$g_2(\tau)$	normalized scattered light intensity autocorrelation function
ΔH	enthalpy change
^{1}H NMR	proton nuclear magnetic resonance (spectroscopy)
$I(t)$	time-dependent scattered light intensity
K	Kelvin
k_B	Boltzmann's constant
LCST	lower critical solution temperature
mL	milliliter
mol%	mole percent
n	refractive index

nm	nanometer
p	mean square scattered light intensity
PB	polybutadiene
PB-*b*-PEO	polybutadiene-*b*-poly(ethylene oxide)
PEO	poly(ethylene oxide)
pF	picofarad
q	modulus of the scattering vector
R_h	hydrodynamic radius
ΔS	entropy change
SEC	size exclusion chromatography
T	temperature
u_i	uncertainty in variable i (99% confidence interval)
UCST	upper critical solution temperature
wt%	weight percent
Γ	half-width of the scattered light spectrum, equivalent to decay rate
η	dynamic viscosity
λ	wavelength of incident light
π	ratio of a circle's circumference to diameter
θ	scattering angle (angle between light source and photo-multiplier)
τ	correlation time
τ_c	characteristic decay time (inverse of Γ)

Bibliography

1. Deng, Y.; Young, R. N.; Ryan, A. J.; Fairclough, J. P. A.; Norman, A. I.; Tack, R. D. *Polymer* **2002,** 43, (25), 7155-7160.

2. Discher, B. M.; Bermudez, H.; Hammer, D. A.; Discher, D. E.; Won, Y. Y.; Bates, F. S. *Journal of Physical Chemistry B* **2002,** 106, (11), 2848-2854.

3. Forster, S.; Berton, B.; Hentze, H. P.; Kramer, E.; Antonietti, M.; Lindner, P. *Macromolecules* **2001,** 34, (13), 4610-4623.

4. Hentze, H. P.; Kramer, E.; Berton, B.; Forster, S.; Antonietti, M.; Dreja, M. *Macromolecules* **1999,** 32, (18), 5803-5809.

5. Hong, S.; Yang, L. Z.; MacKnight, W. J.; Gido, S. P. *Macromolecules* **2001,** 34, (20), 7009-7016.

6. Jain, S.; Bates, F. S. *Science* **2003,** 300, (5618), 460-464.

7. Jain, S.; Bates, F. S. *Macromolecules* **2004,** 37, (4), 1511-1523.

8. Jain, S. M.; Gong, X. B.; Scriven, L. E.; Bates, F. S. *Physical Review Letters* **2006,** 96, (13).

9. Jofre, A.; Hutchison, J. B.; Kishore, R.; Locascio, L. E.; Helmerson, K. *Journal of Physical Chemistry B* **2007,** 111, (19), 5162-5166.

10. Lang, P.; Willner, L.; Pyckhout-Hintzen, W.; Krastev, R. *Langmuir* **2003,** 19, (18), 7597-7603.

11. Nordskog, A.; Futterer, T.; von Berlepsch, H.; Bottcher, C.; Heinemann, A.; Schlaad, H.; Hellweg, T. *Physical Chemistry Chemical Physics* **2004,** 6, (12), 3123-3129.

12. Pispas, S.; Hadjichristidis, N. *Langmuir* **2003,** 19, (1), 48-54.

13. Won, Y. Y.; Brannan, A. K.; Davis, H. T.; Bates, F. S. *Journal of Physical Chemistry B* **2002,** 106, (13), 3354-3364.

14. Won, Y. Y.; Davis, H. T.; Bates, F. S. *Science* **1999,** 283, (5404), 960-963.

15. Won, Y. Y.; Davis, H. T.; Bates, F. S. *Macromolecules* **2003,** 36, (3), 953-955.

16. Won, Y. Y.; Davis, H. T.; Bates, F. S.; Agamalian, M.; Wignall, G. D. *Journal of Physical Chemistry B* **2000,** 104, (30), 7134-7143.

17. Won, Y. Y.; Paso, K.; Davis, H. T.; Bates, F. S. *Journal of Physical Chemistry B* **2001,** 105, (35), 8302-8311.

18. Kotzabasakis, V.; Georgopoulou, E.; Pitsikalis, M.; Hadjichristidis, N.; Papadogianakis, G. *Journal of Molecular Catalysis A-Chemical* **2005,** 231, (1-2), 93-101.

19. Alexandridis, P.; Olsson, U.; Linse, P.; Lindman, B., Structural Polymorphism of Amphiphilic Block Copolymers in Mixtures with Water and Oil: Comparison with Solvent-Free Block Copolymers and Surfactant Systems. In *Amphiphilic Block Copolymers*; Alexandridis, P.; Lindman, B., Eds.; Elsevier Science, B.V.: Amsterdam, 2000; p 169-190.

20. Alexandridis, P.; Olsson, U.; Lindman, B. *Macromolecules* **1995,** 28, (23), 7700-7710.

21. Holmqvist, P.; Alexandridis, P.; Lindman, B. *Journal of Physical Chemistry B* **1998,** 102, (7), 1149-1158.

22. Jacobs, D. T.; Anthony, D. J.; Mockler, R. C.; O'Sullivan, W. J. *Chemical Physics* **1977,** 20, (2), 219-226.

23. Matsuda, H.; Ochi, K.; Kojima, K. *Journal of Chemical and Engineering Data* **2003,** 48, (1), 184-189.

24. Trejo, A.; Yañez, P.; Eustaquio-Rincón. *Journal of Chemical Engineering Data* **2006,** 51, 1070-1075.

25. Alexandridis, P.; Lindman, B., *Amphiphilic Block Copolymers*; Elsevier Science B.V.: Amsterdam, 2000.

26. Linse, P., Modelling of the Self-Assembly of Block Copolymers in Selective Solvents. In *Amphiphilic Block Copolymers*; Alexandridis, P.; Lindman, B., Eds.; Elsevier Science B.V.: Amsterdam, 2000; p 13-40.

27. Lui, T.; Lui, L.-Z.; Chu, B., Formation of Amphiphilic Block Copolymers in Nonaqueous Solution. In *Amphiphilic Block Copolymers*; Alexandridis, P.; Lindman, B., Eds.; Elsevier Science B.V.: Amsterdam, 2000; p 115-149.

28. Nagarajan, R.; Ganesh, K. *Journal of Chemical Physics* **1989,** 90, (10), 5843-5856.

29. Smith, J. M.; Van Ness, H. C.; Abbott, M. M., *Introduction to Chemical Engineering Thermodynamics*. 7th ed.; McGraw-Hill: New York, 2005.

30. Nagarajan, R.; Ganesh, K. *Macromolecules* **1989,** 22, (11), 4312-4325.

31. Nozawa, K.; Gailhanou, H.; Raison, L.; Panniza, P.; Ushiki, H.; Sellier, E.; Delville, J. P.; Delville, M. H. *Langmuir* **2005,** 21, 1516-1523.

32. Pérez-Rodríguez, M.; Prieto, G.; Rega, C.; Varela, L. M.; Sarmiento, F.; Mosquera, V. *Langmuir* **1998,** 14, 4422-4426.

33. Cohn, R. H.; Greer, S. C. *Journal of Physical Chemistry* **1986,** 90, (17), 4163-4166.

34. Caroline, D., Photon Correlation Spectroscopy of Polymer Solutions. In *Developments in Polymer Characterization*; Dawkins, J. V., Ed.; Elsevier: New York, 1986.

35. Rubinstein, M.; Colby, R. H., *Polymer Physics*; Oxford University Press: Oxford, 2003.

36. Thomas, J. C., Photon Correlation Spectroscopy: Technique and Instrumentation. In *Photon Correlation Spectroscopy: Multicomponent Systems*; Schmitz, K. S., Ed.; SPIE - The International Society for Optical Engineering: Bellingham, WA, 1991.

37. Yudin, I. K.; Nikolaenko, G. L.; Kosov, V. L.; Agayan, V. A.; Anisimov, M. A.; Sengers, J. V. *International Journal of Thermophysics* **1997,** 18, (5), 1237-1248.

38. Goldin, A. A. Software for Particle Size Distribution Analysis in Photon Correlation Spectroscopy. http://www.photocor.com/download/manuals/dynals_manual.htm (accessed 17 February 2008).

39. Provencher, S. W. *Makromolekulare Chemie* **1979,** 180, 201.

40. Einstein, A. *Annalen der Physik* **1906,** 19, (4), 289-306.

41. Sandoval, C.; Rezende, M. C.; Gonzales-Nilo, F. *Journal of Solution Chemistry* **2003,** 32, (9), 781-790.

42. Timmermans, J., *Physico-chemical Constants of Pure Organic Compounds*; Elsevier: New York, 1950.

43. Yaws, C. L., *Yaws' Handbook of Thermodynamic and Physical Properties of Chemical Compounds* (electronic edition); Knovel: 2003.

44. Xiang, H. W.; Laesecke, A.; Huber, M. L. *Journal of Physical Chemistry Reference Data* **2006,** 35, (4), 1597-1620.

45. Basu, S.; Vutukuri, D. R.; Thayumanavan, S. *Journal of the American Chemical Society* **2005,** 127, 16794 - 16795.

46. Tamura, K.; Li, H. *Journal of Chemical Engineering Data* **2005,** 50, 2013-2018.

47. Rodriguez, F.; Cohen, C.; Ober, C. K.; Archer, L. A., *Principles of Polymer Systems*. 5th ed.; Taylor & Francis: New York, 2003.

48. Israelachvili, J. N.; Mitchell, D. J.; Ninham, B. W. *Journal of The Chemical Society-Faraday Transactions II* **1976,** 72, 1525-1568.

49. Dreiss, C. A. *Soft Matter* **2007,** 3, (8), 956-970.

50. Elliott, J. R.; Lira, C. T., *Introductory Chemical Engineering Thermodynamics*; Prentice Hall PTR: Upper Saddle River, NJ, 1999.

51. Matsuda, H.; Ochi, K. *Fluid Phase Equilibria* **2004,** 224, 31-37.

52. Khurma, J. R.; Fenby, D. V. *Australian Journal of Chemistry* **1982,** 35, 1281-1284.

53. Bird, R. B.; Stewart, W. E.; Lightfoot, E. N., *Transport Phenomena*. 2nd ed.; John Wiley & Sons, Inc.: New York, 2002; 'Vol.' p.

54. Anisimov, M. A.; Kiyachenko, Y. F.; Nikolaenko, G. L.; Yudin, I. K. *Inzhenerno-Fizicheskii Zhurnal* **1980,** 38, (4), 651-655.

55. Will, S.; Leipertz, A. *International Journal of Thermophysics* **1997,** 18, (6), 1339-1354.

56. Park, J.-H.; DeShong, P., Personal Communication. 2008.

57. Abramowitz, M.; Stegun, I. A., *Handbook of Mathematical Functions with Formulas, Graphs, and Mathematical Tables*; Dover: New York, 1972.

58. Schoffstall, A. M.; Gaddis, B. A.; Druelinger, M. L., *Microscale and Miniscale Organic Chemistry Laboratory Experiments*. 2nd ed.; McGraw-Hill: Boston, 2004.